PHOTONICS

CMDITR Review of Undergraduate Research

Contributions from undergraduate research experiences within the
NSF Center on Materials and Devices for Information Technology Research

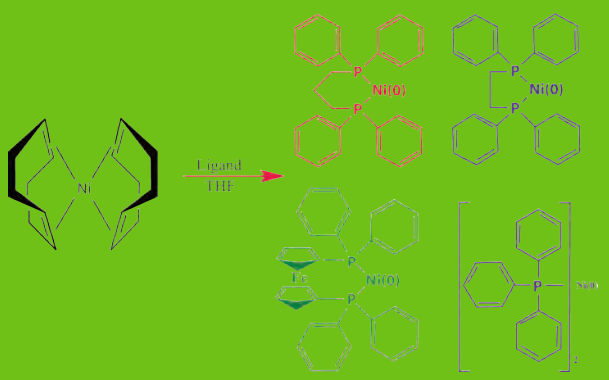

Volume 5, Number 1

This material is based upon work supported by the STC Program of the
National Science Foundation No. DMR 0120967.

Printed in the United States at the University of Washington, Seattle, WA

Inquires should be addressed to:

Center on Materials and Devices for Information Technology Research
University of Washington
Department of Chemistry
Box 351700
Seattle, WA 98195-1700

reu@stc-mditr.org

http://stc-mditr.org

Volume 5, Number 1

Table of Contents

1 Parameter Study of an Acid Catalyzed Sol-Gel Reaction, Using Spectroscopic Methods
Eduardo Acevedo, California State Polytechnic University

5 Methods for Two Photon Absorption Polymerization in SU-8 and Subsequent Development of a Miniature SU-8 Waveguide Hydrophone
Justin Aschenbener, University of Chicago

7 Characterization of Silver Nanoparticle Plasmon Effects on Systems of Free and Affixed Chromophore Dyes
William Boyd, Georgia Institute of Technology

11 Effects of Amorphous Polycarbonate Buffer Layers on Photorefractive Polymers
Victor Densmore, Pima Community College

14 Characterization of Third Harmonic-Generation in Amorphous Polymer Films Doped with Push-Pull Chromophores
Michael Gaj, University of Arizona

19 Synthesis of Benzo[1,2-b:4,5-b']dithiophene Derivatives for OFET Applications
Taylor Giddens, Georgia Institute of Technology

23 The Effect of Processing Parameters on the Properties of Transparent SWNT Electrodes
Joshua Gomberg, Cornell University

27 Ambipolar Solution-Processed Organic Field-Effect Transistor with Al metal as Source/Drain Electrodes
Adrian Grant, Tuskegee University

31 Piezo-Electric Laser Control for Ultra-Cold Atom Manipulationl
Kevin Gudenkauf, University of Arizona

33 Novel Mixed-Crystal System for Studying Single Molecule Photophysics
Elizabeth Jimenez, California State University, Stanislaus

36 Studies of the Optical Properties of Self-Assembled Photonic Crystals Infiltrated with Conjugated Polymers
Meng Kang, Duke University

43 Two-Photon Polymerization of Hydrogels for Biological Applications
Andrew Koltonow, University of Michigan

47 Layer-by-Layer Assembly of CdTe and CdSe Semiconducting Nanocrystals: Toward Solution Processable Inorganic Type-II Heterojunction Solar Cells
Avery Lindeman, Harvard College

51 Dickson Charge Pump Measurements for Comparison of Voltage Gain Efficiencies with Organic Solar Cells
Daniel J. Lum, Louisiana State University

55 Fabrication and Characterization of Bulk Heterojunctions Based on Low Band Gap Polymers
Ariel S. Marshall, University of Central Arkansas

59 Attenuating Conductivity in Electro-Optic Devices via Sol Gel Deposition of TiO_2
John R. Milton

61 A Spectroscopic Analysis of a Candle Flame Light Source
Angela N. Parker, Norfolk State University

64 Effect of Salts on the Drop Size Dependence of the Water Contact Angle
Kim Reishus, Taylor University

68 Single Molecule Spectroscopy: Intermittent Luminescence Studies
Colleen Ross, University of Washington

71 Novel Host Materials for Highly Efficient Blue Emitting OLEDs
Richard Schaugaard, Edmonds Community College

74 Control Systems and Laser Beam Stabilization
Krystal R. Stevenson, Norfolk State University

77 The Effects of Binding Ligands on Nickel Catalysts in the Polymerization of Poly(3-Hexylthiophene)
Michelina Stoddard, Seattle Central Community College

81 Easily-Processed Metal Oxide Thin Films for Use as Interlayers and Encapsulants in Organic Solar Cells
Delvin Tadytin, University of Arizona

85 The Synthesis of Organic Dyes as Charge Carriers for Organic Field Effect Transistor (OFET) and Organic Photovoltaic (OPV) Devices
Donovan Thompson, Georgia Southern University

89 Electro-Optic Coefficient Measurement Using Mach-Zehnder Interferometry
Rika M. Yatchak, University of California San Diego

Welcome to the Fifth Edition of CMDITR's Review of Undergraduate Research

This volume features extended abstracts written by student participants in the National Science Foundation (NSF) Center on Materials and Devices for Information Technology Research (CMDITR) Summer 2008 Research Experiences for Undergraduates (REU) program.

The REU experience is intended to serve as a catalyst for entry by undergraduates into careers involving science, technology, engineering, and mathematics. The REU experience provides a rich learning opportunity not only for the undergraduate participants who experience research first-hand prior to committing to graduate study, but also for the student's mentor, be they faculty members, research scientists, post-doctoral fellows, or graduate students. While working with REU students, mentors develop teaching and mentoring skills, and benefit from reflecting on the excitement of cutting-edge research upon which their careers have been built.

The CMDITR REU Program placed undergraduate students from across the United States in CMDITR research laboratories at the University of Washington, the University of Arizona, and Georgia Institute of Technology. All of the participants worked on authentic interdisciplinary research projects that contributed to advancements in information technology-encompassing activities in chemistry, physics, optics, materials science and engineering. The program emphasized the teamwork nature of scientific research, and was supplemented by a collection of activities including ethics training and workshops in scientific communication.

This publication offers a forum for participants to share their research with their REU peers, future REU students, CMDITR graduate students and faculty, and others interested in the research activities of CMDITR. To learn more about this REU program please visit *www.stc-mditr.org/reu*.

A special thanks to all of the REU participants for their hard work, to their mentors for their time and patience, and to the REU program coordinators Olanda Bryant, Marya Dominik, and Kimberly Sierra-Cajas, for their organizational efforts. A final, but important thanks goes to Ly Pham and Suzy Hunter for their work in the production of this volume.

The extended abstracts included here are presented in alphabetical order by the participant's last name.

Philip Reid, Editor.

Parameter Study of an Acid Catalyzed Sol-Gel Reaction, Using Spectroscopic Methods

EDUARDO ACEVEDO, California State Polytechnic University
Roland Himmelhuber, Robert A. Norwood, College of Optical Sciences, University of Arizona

Introduction

Silicate based inorganic-organic hybrid polymers have been investigated intensively for the past decade due to their physical and chemical properties.[1, 2, 3, 4] These hybrid polymers have been a great focus during this era because of their quick production and their low cost. These materials are synthesized, using the sol-gel process and can be engineered with great flexibility by variation of the catalyst, silane, and temperature.[2, 3] With such maneuverability, one can control the synthesis carefully for the specific application of the sol-gel.[3, 4] Applications consist of photo-lithography, optical wave-guiding, lens creation, beam splitters, telecommunication modulation, optical filters, and anti-scratch coatings.[1] For this project, the sol-gel is to be used as an optical wave-guide.

The main objective of this study is to gain a better understanding of the chemical structures of newly developed sol-gels used in micro-optical devices. The goal is to see how processing conditions and synthesis influence the presence of specific functional groups in the liquid material, like the OH group at 3200 cm^{-1} and the CC double bonds at 1640 cm^{-1}. [1, 2, 3, 5, 6]

Research Methods

The chemicals that were used in the synthesis of the material are Methacryloxypropyltrimethoxysilane [MAPTMS], Diphenyldimethoxysilane [DPDMS], and hydrochloric acid. MAPTMS was used because of its cross-linking properties between organic-inorganic compounds and its photo-patternable properties. DPDMS was used to reduce the optical loss by reducing the aliphatic groups in MAPTMS [4]. Hydrochloric acid was used as a catalyst and as a reactant for the hydrolization process.

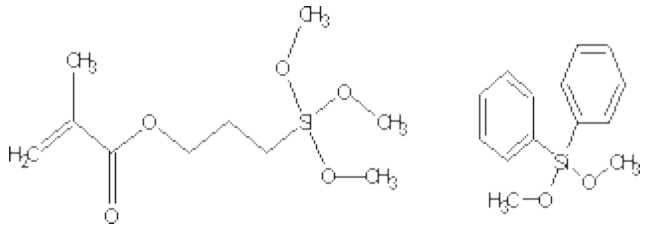

Figure. 1 Structures of MAPTMS and DPDMS (left to right)

In order to gain a better understanding of the sol-gels during the processing conditions and synthesis, the project was divided into three tests. The first test consisted of the variation of the hydrolization ratio (h_R), which is the ratio of water to hydrolizable groups.[2] The hydrolizable groups in this sol-gel are methoxy groups (R-O-CH_3). In the second test, the catalyst concentration was varied. The different concentrations (moles of HCl/1L of water) that were used were 0.1M, 0.2M, 0.5M, and 1M. For the third test, the variable was the stirring time. It would be ideal to know the minimum amount of stirring time needed to make an efficient sol-gel.

In this project, two main apparatus were used. The first one is a Fourier Transform Infrared Spectrometer (FT-IR). The FT-IR was used because it is one of the simplest techniques for polymer identification and its detection abilities of chemical functionalities. Another primary reason was that it can easily detect the OH peak at around 3200 cm^{-1}. The manner, in which the FT-IR was used, was that a drop of the sol-gel was placed in between two NaCl pallets. NaCl was used because it shows no absorption in the infrared spectrum. Then, the NaCl pallets are placed in a sample holder inside the FT-IR, which then allows the transmission to be recorded. The second apparatus used was an UV-Vis-NIR spectrometer. It was used because it is a direct measurement of the optical loss in the telecommunication region of 1550 nm.[1, 4] The spectrometer was operated in the way that the sol-gel was poured into a cuvette which was then placed inside the apparatus. Once the cuvette is positioned, the spectrum of the sample is measured.

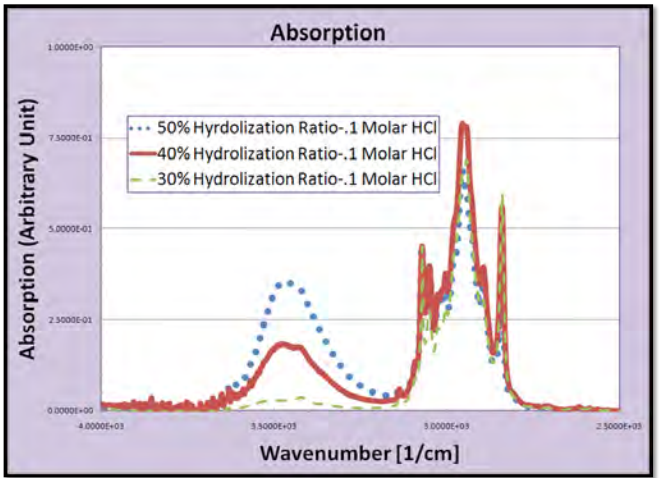

Figure 2. FT-IR spectra of hR 50%, 40%, and 30%

In Figure 2, an FT-IR spectra of three materials with different hR can be seen.[5, 6, 7] The broad peak at 3500 cm^{-1} is the peak of the OH groups. When recording the data from the FT-IR, every sample needed to be normalized due to different thicknesses of the samples. The peak that the graphs were normalized to is the peak of the phenyl groups at 3070 cm^{-1}. In the hydrolization test and in the stirring test, the data was compared semi-quantitatively by measuring the area under the OH curve of each sample. For the test of various catalyst concentrations, the same approach was quite difficult to accomplish since there were noise complications. Instead, the height of each peak was used. In broad, the concern is to minimize the OH peak because in sol-gels the lower the OH groups, the lower the optical loss at 1550 nm.

Results and Discussion

In the first test, the variation was the hyrdolization ratio, h_R. The hydrolization ratio is the ratio of water to methoxy groups. In a broad sense, the higher the h_R, the more viscous the sol-gel becomes because more of the sol-gel is being hydrolyzed, thus causing larger Si-O-Si networks. The different hydrolization ratios used were 20%, 25%, 30%, 35%, 40%, and 50%. In the three tests, there were three main parameters that were kept constant, which were 3 grams of MAPTMS, 2.95 grams of DPDMS, and the sample was heated to 100 °C. The samples were heated to that temperature because during the stirring process, methanol is produced from the methoxy groups. To remove the methanol in a very effective manner, the sample is heated to 100 °C because methanol evaporates at 65 °C.

The results for the FT-IR spectra indicate that 30% h_R is the ratio with the lowest area under the OH peak. Table 1 illustrates that 30% h_R has a considerably lower h_R than the other samples, and can be a potential h_R for the sol-gels.

Although 30% indicated the lowest absorption reading, in actuality it can be inferred that its variation is within the error margin.

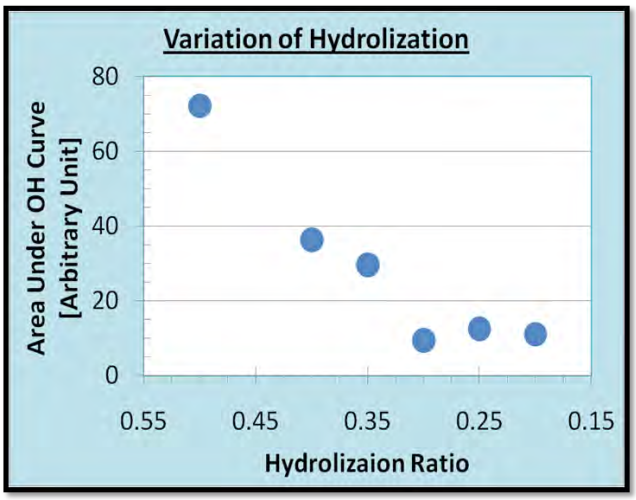

Figure 3. Area under OH curve for each h_R

Hydrolization Ratio	Area under OH Peak
50%	72.2
40%	36.4
35%	29.7
30%	9.5
25%	12.6
20%	11.1

Table 1. Area under OH peak in respect with the h_R

The NIR spectra (Figure 4), indicates that 30%, 25%, and 20% are practically identical in respect to the optical loss. This demonstrates that h_R greater than 30% can be discarded as potential hydrolization ratios because the optical loss is greater in respect to the other samples.

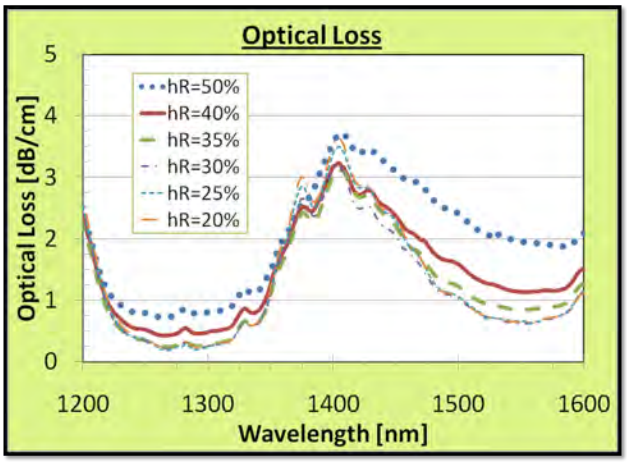

Figure 4. Optical loss for various h_R

The second test consisted of the variation of the catalyst concentration. The purpose is to see the influence of the catalyst concentration on the OH peak and the optical loss. The catalyst concentrations used were 0.1M, 0.2M, 0.5M, and 1M. The same three parameters were used with an addition of a 30% h_R for all samples.

The results of the FT-IR indicated that 0.5M had the lowest OH peak, meaning that it absorbed the least amount of light. One thing to note from Figure 5 is that 0.1M and 1M are not too different than 0.5M in respect with the OH peak. Also, 0.2M is definitely not a potent catalyst due to its high OH peak.

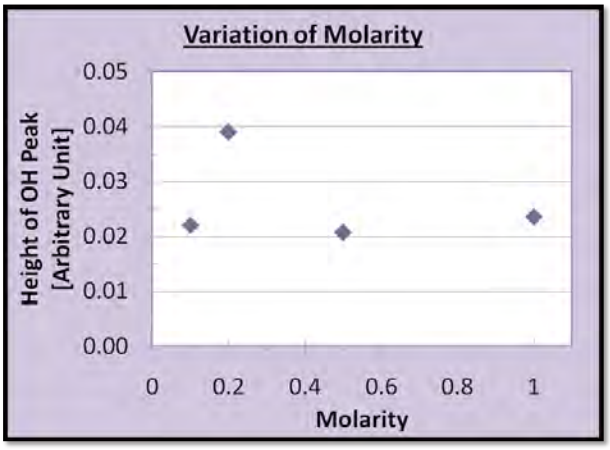

Figure 5. Height of OH peak in respect with the catalyst concentration

The optical loss for the samples, however, demonstrates that 1M catalyst concentration has the lowest optical loss, as illustrated in Figure 6. On these results, one thing to note is that 0.1M is very similar to 1M in terms of optical loss. Again, 0.2M can be withdrawn as a catalyst because the optical loss and absorption are both considerably high.

The third and final test consisted of the variation of stirring times. The task was to find out what would be the minimum amount of stirring time for the sol-gel synthesis to be efficient. The three main constant parameters were still used with an addition of 0.1M catalyst and 30% h_R.

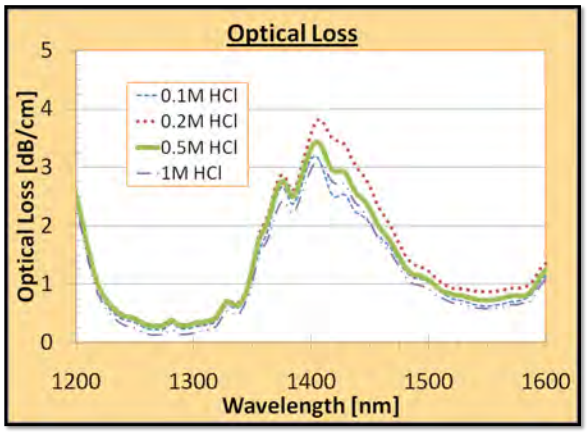

Figure 6. Optical loss in respect with catalyst concentration

The results of the FT-IR spectra indicated that the area under the OH curve was the lowest at 101 hours of stirring. The graph was formatted into a log scale for the time axis, as seen in Figure 7. After finalizing the data however, it was clear that after approximately 40 hours of stirring, the change was marginal.

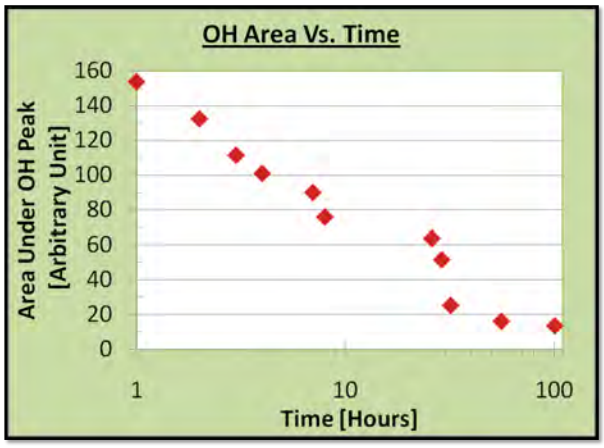

Figure 7. Area under OH peak in respect with the stirring time

Conclusion

From the results of these three tests, it is concluded that a hydrolization ratio of less than 30% is a potential candidate. From the six total ratios, 35%, 40%, and 50% are discarded, since their OH concentrations are higher than the 20%, 25%, and 30% h_R. For the test regarding the various catalyst concentrations, it is concluded that 0.1M, 0.5M, and 1M are potent catalysts. The 0.2M HCl would be discarded as potential catalyst because its results from the FT-IR spectra and the NIR spectra were clearly too high in comparison to the other concentrations. For the third test, it is concluded that the OH concentration is the lowest after 101 hours of stirring time, but the effort is not worth it. The difference of approximately 45 hours and 101 hours is marginal, so an approximate stirring time of 45 hours is recommended.

Future work with these particular sol-gels would be to vary the h_R with different catalyst concentrations. For example, use 35% h_R with a catalyst concentration of 1M. Another available expansion on this research that was started but never finished would be to explain why minimal changes appear in the FT-IR spectra and NIR spectra when the sol-gel is heated to temperatures above 100 °C. This phenomenon would be interesting to understand because as the sol-gel was heated to temperatures like 120 °C, 130 °C and 140 °C, the sol-gel became very viscous without noticeable change in the spectra. Further expansion of this work would be to study why 0.2M has such high concentrations of OH groups when 0.1M, 0.5M, and 1M have lower concentrations.

Acknowledgments

Funds for this research were provided by the Center on Materials and Devices for Information Technology Research (CMDITR), and the NSF Science and Technology Center No. DMR 0120967. I would also like to give thanks to Dr. Robert Norwood for his guidance in this incredible project and for his noble advice in this field. Special thanks to Roland Himmelhuber for all the amazing information that he has shared with me not only in the field of optics, but also in life.

References

1. O. Soppera; P.J. Moreira; P.V.S. Marques; A.P. Leite. Science Direct 2006, 430-435.
2. W. Kim; R. Houbertz; T. Lee; B. Bae. Journal of Polymer Science 2004, 1979-1986.
3. R. Houbertz; G. Domann; J. Schulz; B. Olsowski; L. Fröhlich; W. Kim. Applied Physics Letters 2003, 1105-1107.
4. M. Oubaha; P. Etienne; S. Calas; R. Sempere; J.M. Nedelec; Y. Moreau. Science Direct 2005, 2122-2128.
5. I. Fleming. Spectroscopic Methods In Organic Chemistry. Berkshire, England: McGraw-Hill Publishing Company Limited, 1966.
6. K. Nakanishi. Infrared Absorption Spectroscopy. Tokyo, Japan: Nankodo Company Limited, 1962.
7. R. A. Nyquist. Interpreting Infrared, Raman, And Nuclear Magnetic Resonance Spectra. 1. San Diego: Academic Press, 2001.

EDUARDO ACEVEDO is pursuing a bachelor's degree at the California State Polytechnic University in Pomona. Upon completion, his goal is to attend graduate school and receive his PhD in the field of Optical Science.

Methods for Two Photon Absorption Polymerization in SU-8 and Subsequent Development of a Miniature SU-8 Waveguide Hydrophone

JUSTIN ASCHENBENER, University of Chicago
Antao Chen, Applied Physics Laboratory, University of Washington

History and Background

In 1931 Maria Göppert-Mayer published her doctoral thesis, outlining the theoretical plausibility of multiple photon absorption, in which a molecule is driven to a new energy state by absorbing more than one photon simultaneously.[1] However, it was not until 1961 that the creation of the laser provided scientists with enough photons in one place to initiate this process.[2] Today, multiple photon absorption is at the heart of numerous research problems with the potential to benefit fields not limited to medicine, telecommunications, and computer engineering.[3]

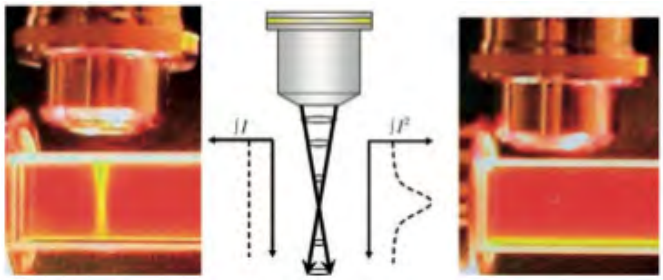

Figure 1. As opposed to single photon processes (left), TPA (right) allows for localization of the reaction to a small focal volume. Image from LaFratta and Fourkas, Angew. Chem. Int. Ed. 2007, 46, 6238-6258

One such avenue of this research is microfabrication by using two-photon absorption (a subset of multiple photon absorption) to drive photocrosslinking or photopolymerization.[4] Because the process of two photon absorption (TPA) requires a unique coincidence of high counts of molecules in photons in the same place at once, such a method of microfabrication can be used to create very small structures with very high resolution. Microfabrication by TPA polymerization also offers gains in utility over other more conventional methods of microfabrication. Where conventional methods of microfabrication usually work in layers so constraints on each layer are in part dictated by underlying layers, TPA polymerization is layer independent. The light source essentially draws the desired structure freehand in whatever photoresist is used. Such aspects of microfabrication by TPA polymerization offer obvious potential for an endless list of applications.

Equipment and Photoresist

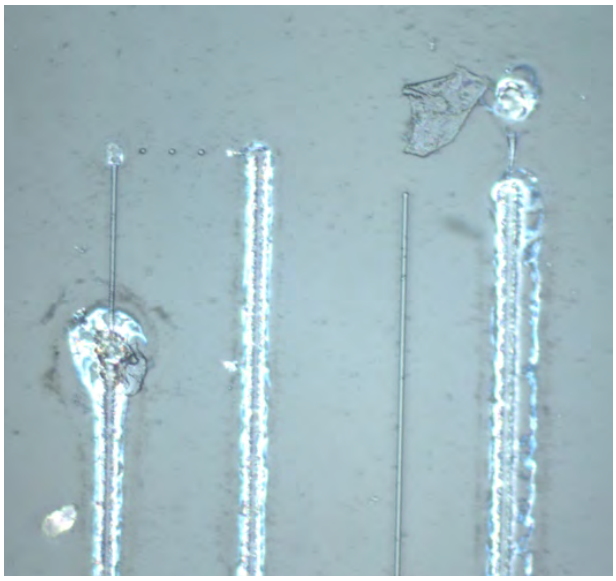

Figure 2. Instead of the usual clean polymer (clean lines above) too intense of light results in burns.

The Chen group at the Applied Physics Laboratory at the University of Washington realizes the potential of the process and has therefore chosen to study and become familiar with microfabrication by TPA polymerization. SU-8, a commercially available photoresist produced by MicroChem usually used for UV microfabrication, has been chosen for use in these early experiments by merit of its success in producing 30 nm nanorods.[5] The research team runs a Ti:Sapphire oscillator at 800 nm through a collimator, and then through an attenuator which allows for beam intensity variability. The collimated beam can fill the entire back aperture of a microscope outfitted with a Mitutoya lens with a numerical aperture of .42. Samples are prepared on a 1" square of microscope slide following the standard procedure for SU-8 preparation[6] and translated with respect to the focal volume of the beam using a computer-controlled stage with Labview capabilities. The Chen group has a series of programs created by former graduate student Dr. Cody Young which can translate CAD diagrams and image files into trajectory files for the stage to read and write using a Raster scan method.

Fabrication

First attempts at polymerization consistently resulted in bright flashes emitted from stage during fabrication, signifying immediate

burning of any created polymer. After failed attempts at mitigation through the varying of translation speed (burning was found to be largely translation speed independent), a solution was found through the addition of the aforementioned attenuator to the setup, and a suitable writing laser intensity was found (yet to be quantified). Inconsistent polymerization through full sample-width passes was also frequently observed, and was most likely caused by different portions of the focal volume entering different regions in the SU-8 due to a tilted sample. This prompted the writing of an artificial leveling program in Labview code, which augments the original z coordinates and adjusts for sample tilt. Concerns about the rough surface of the SU-8 application on the slide causing improper polymerization necessitated dilution of the SU-8 solution with cyclopentanone. This resulted in a more consistent reaction.

Application to Waveguide Hydrophone

Straightforward experimental results in early fabrication steps allowed for prompt application of methods for fabrication to the concept of a miniature SU-8 waveguide hydrophone. The research team has recently been developing a hydrophone consisting of two opposing optical fibers, one stationary and the other cantilevered. Bombardment of this setup underwater with sound waves of varying frequency results in varying amounts of light being transmitted successfully from one fiber to the other. SU-8 waveguides work not unlike optical fibers, in that the high refractive index of solid SU-8 relative to the surrounding air results in containment of the light. Figure 3 shows the proposed design for such a hydrophone. Crucial to this setup, but not pictured, are the optical fibers to be glued to each end of the waveguide for provision and reception of laser light.

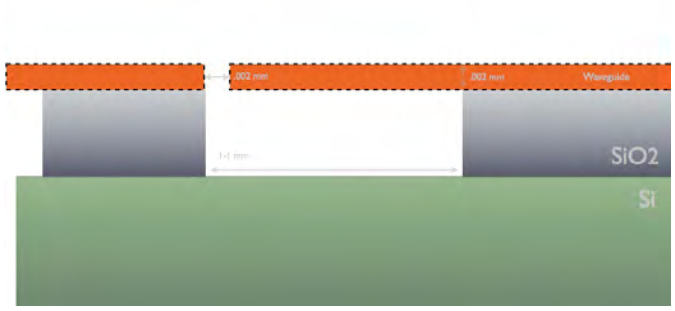

Figure 3. Proposed structure for miniature SU-8 waveguide hydrophone.

Future Work

The proposed waveguide hydrophone will undergo rigorous testing after fabrication. This testing will include but not be limited to investigations of sound intensity vs. transmitted light, waveguide materials, fabrication of waveguide using alternative TPA writing methods (raster vs. vector scan), the efficiency of differing wavelengths of light used in the waveguide, and alternative waveguide hydrophone housings.

The Chen group also plans to apply this newfound ability of TPA polymerization in SU-8 to create new, novel structures and waveguides. One primary and immediate step to achieve these ends is the addition of an option to the code for trajectory creation to employ a vector scan, as opposed to raster scan method. Where a raster scan (similar to the operation of an inkjet printer) leaves imperfect bumpy edges on created curves and structures because of its stepwise nature, a vector scan could trace out the edges of a structure first, leaving a smooth arc. This smoothness will allow for the creation of more efficient waveguides, opening in turn an even greater number of possibilities for optical devices fabricated using this method.

References

1. M. Göppert-Mayer, Ann. Phys. 1931, 9, 273.
2. W. Kaiser, C. G. B. Garrett, Phys. Rev. Lett. 1961, 7, 229.
3. J. T. Lafratta et al. Angew. Chem. Int. Ed. 2007, 46, 6238–6258.
4. H-B. Sun and S. Kawata. Journal of Lightwave Technology. 2003, 21, 3.
5. S. Juodkazis et al. Nanotechnology 2005, 16, 846-849.
6. 'SU-8 2000: Permanent Epoxy Negative Photoresist' Micro-Chem Corp., Newton, MA. http://microchem.com/products/pdf/SU-82000DataSheet2025thru2075Ver4.pdf.

JUSTIN ASCHENBENER is currently an undergraduate physicist at the University of Chicago. His post-2011 graduation plans are a toss up between going to graduate school and finding work (in bulk, of course) at the local Costco.

Characterization of Silver Nanoparticle Plasmon Effects on Systems of Free and Affixed Chromophore Dyes

WILLIAM R. D. BOYD III, Georgia Institute of Technology
Wojciech Haske , Joseph Perry, Georgia Institute of Technology

Introduction

In recent years much work has been done to characterize the optical properties of metal nanoparticles (NPs). Metal NPs are polarizable and in the presence of an incident electromagnetic field at resonance frequency their electrons oscillate (Figure 1) and produce a resultant electric field surrounding the local vicinity of the nanoparticle that is greater than solely that of the incident light. Plasmon resonance effects have brought metal NPs to the forefront of research for applications such as optical power limiting,[1] photodynamic cancer therapy,[2] and biosensor technology.[3]

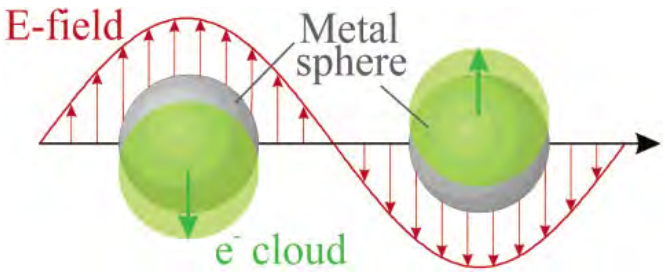

Figure 1. An electromagnetic field induces oscillations of a nanoparticle's conduction band electrons.

The objective of this research project was to characterize silver NP (AgNP) systems with chromophores such as 4,4' bis (N-phenyl, N-3-methylphenyl amino)biphenyl (TPD), and 1,4-bis(4-nitrostyryl)2-methoxy-benzene (BN) (Figure 2). The systems studied included both free chromophores in solution with AgNPs and chromophore-coated AgNPs. Physical characterization of these systems sought to determine chromophore-AgNP chromophore ligand adsorption-desorption reaction kinetics, the coverage of chromophores on the surface of AgNPs, and the solubility and thermodynamic stability of chromophore-coated AgNPs in various organic solvents. Optical characterization included theoretical modeling and experimental probing of the effects of plasmon resonance on the fluorescence lifetimes of TPD and BN.

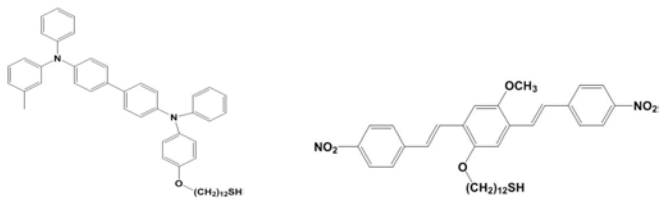

(a) (b)

Figure 2. The thiolated chromophores: (a) TPD and (b) BN.

Research Methods

Physical Characterization

The first step towards physical characterization of systems of AgNPs and chromophores was to synthesize a substantial quantity of Ag-NPs from which to produce the chromophore-AgNP systems. The AgNP synthesis procedure involved reacting silver acetate (AgAc) with oleylamine (OLA) in boiling o-xylene solvent in an oxygen-free environment (Figure 3). At specified intervals during the synthesis, small samples were extracted for transmission electron microscopy (TEM) to determine the size distribution of the AgNPs using ImageJ software. Following the synthesis reaction, the AgNPs were purified by aggregating the particles in ethanol, centrifuging the heavy aggregates at 3500 rpm to precipitate the AgNPs, and removing the supernatant. A stock solution of AgNPs dissolved in toluene was stored in a glove box under nitrogen to prevent oxidation on the surface of the AgNPs.

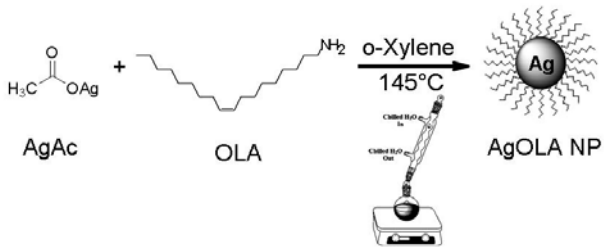

Figure 3. AgNP synthesis reaction of silver acetate (AgAc) and oleylamine (OLA) in boiling o-xylene at 145 °C produced oleylamine ligand-coated AgNPs.

Following the AgNP synthesis, samples of chromophores-modified AgNPs were prepared. This was accomplished by a ligand-exchange reaction with both TPD and BN chromophores. The weakly bound oleylamine on the surface of the particles was partially replaced by the chromophoric ligands which bound strongly through terminal thiol groups (Figure 4). Based on the thiol's footprint (21 $Å^2$) and the size distribution and calculated surface area of the AgNPs, the relative concentrations of chromophores to AgNPs could be determined. The chromophore-coated AgNPs were purified by aggregating the AgNPs in hexane, centrifuging the samples at 3500 rpm for 10 minutes, and extracting the supernatant, leaving behind the chromophore-modified AgNP precipitant. This process was repeated four times and the chromophore-coated AgNPs were finally dissolved in toluene (TPD) or dichlorobenzene (BN). The chromophore coverage on the surface of the AgNPs was estimated following the exchange reaction by analyzing the UV-vis

absorption spectrum of the extracted supernatant. Following the purification procedure, the solvent of the extracted supernatant was removed with a rotary evaporator, leaving behind a small residue of unreacted chromophores and AgNPs. The residue was dissolved in a known volume of solvent (toluene for TPD and dichlorobenzene for BN) and UV-vis spectra were taken of the resulting solutions. A MATLAB analysis program estimated the spectral contribution of isolated AgNPs and chromophores to the resultant supernatant spectrum using a least-squares minimization method. From the estimated chromophore absorbance in the supernatant and the chromophore extinction coefficients, the concentration of chromophores in the supernatant was calculated from Beer's Law.

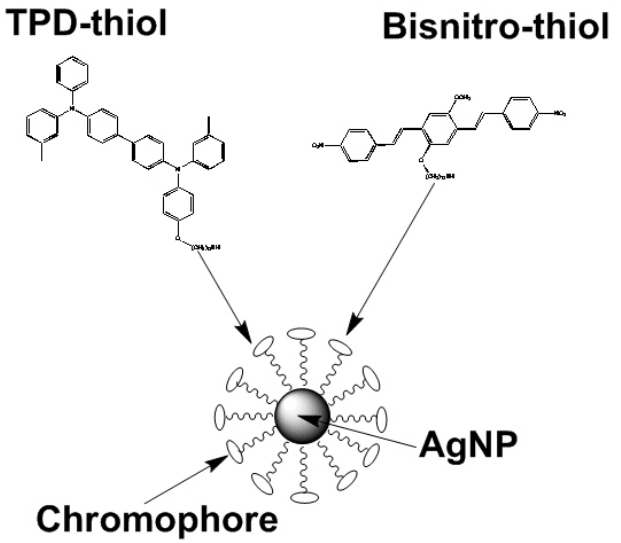

Figure 4. TPD and (b) BN each shown with an oxy-dodecylthiol ($(CH_2)_{12}SH$) for attachment to the silver NP surface.

The thermodynamic stability of the chromophore-coated AgNPs was studied with time-based fluorimetry and UV-vis spectroscopy. Due to the proximity of the chromophores to the metal surface (~1nm) and Förster Resonance Energy Transfer (FRET), the fluorescence of affixed TPD and BN was strongly quenched. By monitoring the fluorescence emission over time using time-based fluorimetry, any observed increase in fluorescence indicated the desorption of chromophores from the surface of the AgNPs. This was due to the reduced fluorescence quenching rate of the free chromophores when desorbed in solution as compared to when adsorbed on the metal surface. In addition to time-based fluorimetry, UV-vis spectroscopy was used to indicate damage to the AgNP-chromophore systems in various organic solvents based on shifts of the spectra over time.

Optical Characterization

Optical characterization of the chromophore-AgNP systems aimed to (1) model the effects of AgNP plasmon resonance on the fluorescence emission of affixed chromophores and (2) measure the fluorescence lifetimes of free TPD and BN chromophores, as well as those affixed to the surface of AgNPs. The modeling was done in MATLAB in accordance with the theoretical results derived by Gersten and Nitzan for the fluorescence of a molecule near a spheroid.[4] This theory classically treats the chromophores as oscillating molecular dipoles in their excited singlet state. The oscillating molecular dipoles induce dipole moments on the surface of the AgNPs which allows for energy transfer processes to occur between the excited state chromophores and the AgNPs. By utilizing the dielectric function of silver,[5] the radiative and non-radiative constants, k_r and k_{nr}, along with the fluorescence quantum yields Φ_F were computed for a series of AgNP diameters and fluorescence emission wavelengths.

Fluorescence lifetimes of free and affixed TPD and BN chromophores were measured by Time Correlated Single Photon Counting (TC/SPC) (Figure 5). The TC/SPC measurement produced a histogram of the decay times for individual photons emitted by TPD and BN via fluorescence. The experiment was performed on samples of free TPD and BN in solution and samples of TPD and BN affixed to AgNPs.

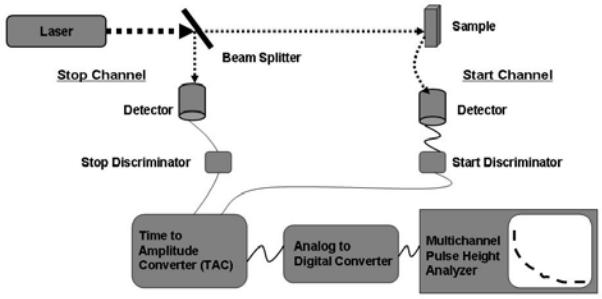

Figure 5. Time-Correlated Single Photon Counting (TC/SPC). A femtosecond pulsed laser is split into Start and Stop Channels. The Start Channel detector triggers the TAC to begin a time count following the detection of a photon from fluorescence emission until the Stop Channel triggers the TAC to end counting. The emission times are then projected as a histogram on the Multichannel Pulse Height Analyzer.

RESULTS

Physical Characterization

The AgNP synthesis reaction and purification was successfully completed in an oxygen-free environment resulting in a stock solution of AgNPs with a fairly narrow size distribution. Analysis of TEM images of the resulting AgNPs (Figure 6) revealed the average AgNP diameter to be 4.71 nm with a standard deviation of 13.6%.

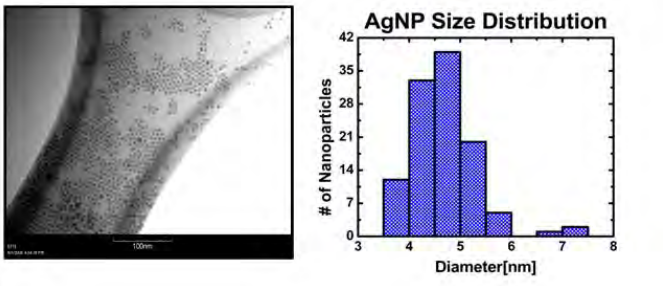

Figure 6. TEM image of AgNPs (left) and AgNP size distribution produced from ImageJ software analysis of TEM image (right).

Exchange reactions with the thiolated chromophores were successfully completed and the resulting chromophore-coated AgNPs were purified. Spectral deconvolution of the supernatant revealed the chromophore coverage of BN($(CH_2)_{12}$SH) to be 60.8% and TPD($(CH_2)_{12}$SH) to be 69.8%.

The thermodynamic stability of the chromophore-AgNP systems was measured using time-based fluorimetry and UV-vis spectroscopy (Figure 7). Such measurements were made in a variety of organic solvents in order to determine the most stable conditions for each system. An additional concern that arose was fluorescence quenching of the chromophores due to certain solvents. Time-based fluorimetry measurements determined a 5:1 mixture of toluene and DMF to be the best solvent for systems of TPD($(CH_2)_{12}$SH), and dichlorobenzene for BN($(CH_2)_{12}$SH). In the case of TPD($(CH_2)_{12}$SH), time-based fluorimetry (Figure 7a) demonstrated the desorption of chromophores from the surface of the AgNPs in all tested organic solvents, and the absorption spectrum was strongly affected by the irradiation following the fluorimetry experiment (Figure 7b). Alternatively, Figures 7c and 7d demonstrate a relatively stable BN($(CH_2)_{12}$SH)-AgNP system both before and after fluorimetry.

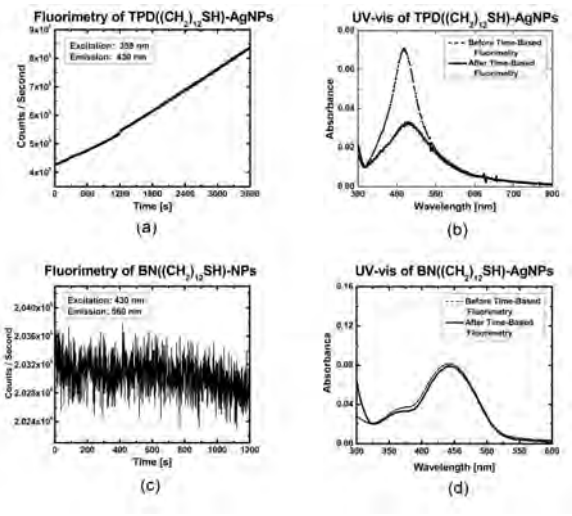

Figure 7. Graphs of time-based fluorimetry and UV-vis spectra of TPD($(CH_2)_{12}$SH)-AgNPs in toluene (a, b) and BN($(CH_2)_{12}$SH)-AgNPs (c, d) in dichlorobenzene.

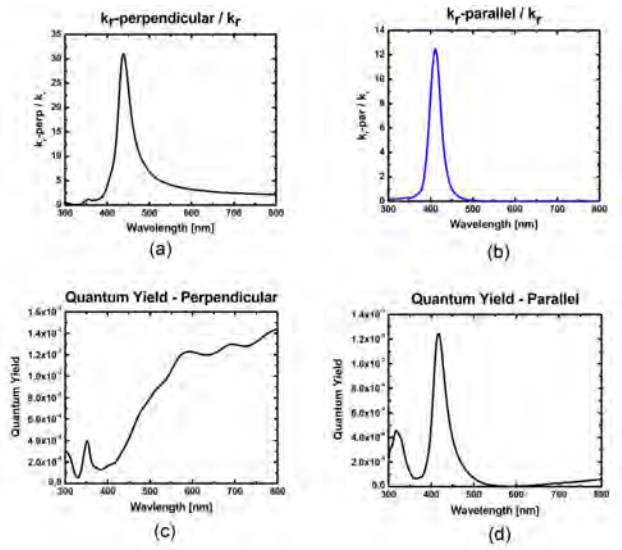

Figure 8. Graphs (a) and (b) plot the ratios of the computed radiative constants of an affixed chromophore to that of a free chromophore for perpendicular and parallel orientations vs. fluorescence emission wavelength. Graphs (c) and (d) plot the computed fluorescence quantum yields for affixed chromophores for perpendicular and parallel orientations vs. fluorescence emission wavelength.

Optical Characterization

The results from modeling an ideal chromophore (Φ_F=1) a distance of 1 nm from a silver spheroid 4.7 nm in diameter (approximate dimensions of the chromophore-AgNP systems studied) are shown in Figure 8. The models were for two special cases: one for chromophores oriented perpendicular to the AgNP surface and the other for chromophores oriented parallel to the AgNP surface. As shown in Figures 8a and 8b, the radiative constants for both orientations are larger by over an order of magnitude than for free chromophores. Since the radiative constant is inversely proportional to fluorescence lifetime τ_r ($\tau_r \propto 1/k_r$), one would expect to measure shorter fluorescence lifetimes for the systems of TPD and BN affixed to chromophores than for free TPD and BN. Indeed, shorter fluorescence lifetimes have been reported for systems involving AgNPs and other chromophores.[7, 8,9] Figures 8c and 8d illustrate the predicted fluorescence quantum yields for both perpendicular and parallel orientations. For each orientation, the quantum yields are on the order of 10^{-3}, more than an order of magnitude smaller than the fluorescence quantum yields of free TPD and BN.

System	BN($(CH_2)_{12}$SH)	TPD($(CH_2)_1$SH)	AgNPs-BN($(CH_2)_{12}$SH)	AgNPs-TPD($(CH_2)_{12}$SH)
Solvent	Dichlorobenzene	Toluene/DMF(5:1)	Dichlorobenzene	Toluene/DMF (5:1)
τ_1 [ns]	**0.017**	**1.600**	**0.020**	**0.604**
Error [ns]	6.224	0.001	3.704	0.027
τ_2 [ns]	**1.551**	-	**1.873**	**2.453**
Error [ns]	0.002	-	0.001	0.003
τ_3 [ns]	-	-	-	-
Error [ns]	-	-	-	-

Table 1. Measured fluorescence lifetimes and errors of free and affixed BN($(CH_2)_{12}$SH) and TPD($(CH_2)_{12}$SH).

The measured fluorescence lifetimes of TPD($(CH_2)_{12}$SH) and BN($(CH_2)_{12}$SH) in toluene and dichlorobenzene, respectively, and TPD($(CH_2)_{12}$SH) and BN($(CH_2)_{12}$SH) affixed to AgNPs in the same respective solvents as shown in Table 1. The fluorescence signal from the chromophore-coated AgNPs was much lower than for the free chromophores during the TC/SPC experiments. This was most likely due to a limitation of the TC/SPC setup since a measured sample must have a high transmittance in order to minimize reabsorption of fluorescence emission. At such high transmittance levels, the concentration of chromophores in the chromophore-coated AgNP samples was much lower than the concentration of chromophores in the samples of free chromophores. Additionally, as discussed in Figure 8, the expected fluorescence quantum yields of the affixed chromophores was much lower than that for the free chromophores, complicating the detection of fluorescence emission by TC/SPC.

Conclusion

This summer's research has shown that ligand-coated silver nanoparticles can be effectively synthesized and purified. In addition, it was demonstrated that ligand- coated AgNPs can be coated with TPD and BN via a thiol-terminated alkane chain linker by a ligand exchange reaction with relatively high efficiency.

Modeling of the classical interactions between excited state chromophores and AgNPs reveal order-of-magnitude enhancements of the radiative constants for chromophores affixed to AgNPs. Such results indicate shorter fluorescence lifetimes for affixed chromophores.

Fluorescence lifetimes of both free and affixed TPD($(CH_2)_{12}$SH) and BN($(CH_2)_{12}$SH) systems were measured using TC/SPC. The measured values indicate that the shorter fluorescence lifetimes measured from the affixed chromophores is too short to measure with a reasonable level of uncertainty using TC/SPC.

Future work must be done to determine whether more stable chromophore-AgNP systems can be developed in alternative organic solvents. In addition, future fluorescence lifetime measurements should be conducted with chromophores affixed to AgNPs via longer alkane chains to reduce the probability of energy transfer, thereby increasing the fluorescence quantum yield and fluorescence signal of the affixed chromophores for TC/SPC.

Acknowledgements

Thanks to the National Science Foundation and the MDITR REU program for sponsoring this research in conjunction with support from Georgia Tech. Special thanks to Dr. Joseph Perry and Wojciech Haske for guiding this research project, and to Michal Malicki, Matteo Cuzzoul, Dr. Matthew Sartin, and Dr. Joel Hales for their assistance and advice in performing this research.

References

1. Martin, Robert B.; Meziani, Mohammed J., Pathak, Pankaj; Riggs, Jason E.; Cook, Davis E.; Perera, Sujith; Sun, Ya-Ping, Optical Materials 29(7): 788-793 (2007)
2. Wang, Shizhong; Gao, Ruomei; Zhou, Feimeng; Selke, Matthias, Journal of Materials Chem 14(4): 487-493 (2004)
3. Graham, Duncan; Faulds, Karen; Smith, W. Ewen. Chemical Communications (42): 4363-4371 (2006)
4. J. Gersten, A. Nitzan, J. Chem. Phys. 75(3): 1139-1152 (1981)
5. P. B. Johnson; Christy, R. W., Phys. Rev. B 6(12): 4370-4379 (1972)
6. Tovmachenko, Oleg G.; Graf, Christina; van den Heuvel, Dave J.; van Blaaderen, Alfons; Gerritsen, Hans C., Advanced Materials 18(1): 91-95 (2006)
7. Fu, Yi; Zhang, J.; Lakowicz, J. R., J. Fluorescence 17: 811-816 (2007)
8. Viger, M. L.; Live, L. S.; Therrien, O. D.; Boudreau, D., Plasmonics 3: 33-40 (2008)

WILLIAM BOYD is currently attending the Georgia Institute of Technology as a physics and mathematics double major. He hopes to graduate in May 2010 and to subsequently pursue a PhD in high energy sub-atomic physics. Eventually, he plans for his research career to evolve towards business as he hopes to start a company involved in a high-tech industry.

Effects of Amorphous Polycarbonate Buffer Layers on Photorefractive Polymers

VICTOR DENSMORE, Pima Community College

Bob Norwood, Nasser Peyghambarian, Cory Christenson, College of Optical Science, University of Arizona

Introduction

Photorefractive (PR) polymers are a material that can experience a change in index of refraction by applying an electric field. This property is being utilized to make re-writable holographic displays. They generally consist of a charge generator, charge trap, and birefringent molecule. It has been hypothesized that adding a thin layer of amorphous polycarbonate (APC) between the PR polymer and the electrodes could reduce the amount of current through the polymer; potentially allowing higher fields to be applied to the PR polymer without the risk of breakdown. However, it is necessary to gain a deeper understanding of the underlying mechanisms to better implement these modifications for display applications.

Many of the properties pertinent to the efficiency of the polymer in its application as a holographic display, such as charge generation rates, types of traps, and trapping rates, affect the conductivity of the material. Therefore, the photoconductivity and dark conductivity will be compared between two samples, each composed of the same materials, but with a thin buffer layer on one which separates the polymer from the electrodes.

Method

Conductivity will be derived from the current across the sample, beginning with the dark current. This will be done by applying a voltage across the sample without illuminating the material and reading the resulting current over the period of time for the current to reach a steady state. In this experiment, the steady state dark current was attained after approximately 40 minutes. The dark conductivity, σ_d, will then be found by the applying the following equation:

$$\sigma_d = \frac{i_d d}{V A_{elec}} \qquad (1)$$

In this equation, i_d represents the steady state dark current, V is the voltage applied, d is the thickness of the polymer (100μm), and A_{elec} is the area of overlap of the electrodes.

When light is applied to the sample, charges are excited and will move under the influence of an applied voltage, creating a current. By varying the voltage with a constant irradiance, the photoconductivity σ_p, of the sample can be found using a similar relation to photocurrent, as in equation (1), with the exception that the dark conductivity is subtracted to find the true current induced by the incident light.

The photoconductivity values can be used to calculate the photogeneration efficiency, which is essentially the number of charge generated per number of photons absorbed in a given volume. Photogeneration efficiency, ϕ, was calculated using

$$\phi = \frac{2\hbar\omega\sigma_p}{\alpha d e I} E \qquad (2)$$

where I is the intensity, α is the absorption coefficient, ω is the optical frequency, and e is the fundamental charge.

A Glassman high voltage supply was used to apply a bias to the sample while a Keithley electrometer was used to read the current across the sample. The laser used was a solid state laser emitting 532nm. The laser was passed through a pockels cell which was used to control the light incident on the sample. Due to the temporal resolution required and sensitivity of the measurements, a Labview program was written to interface with and record data from the voltage supply, electrometer, and pockels cell. Furthermore, the sample was placed in a dark box during testing to limit the noise generated from external light sources. A protection circuit was also integrated into the setup to protect the electrometer from receiving damaging current levels if the sample were to break down and also served as a grounding device to reduce noise from stray currents and capacitance from the optical table, sample stage, and electrometer.

The transient currents in some samples can take several minutes to reach steady-state, therefore, the conductivities for each voltage should be performed separately. For a single voltage trial, the procedure was as follows. Before each trial at a given voltage, a power meter was used to measure the light incident on the sample and the pockels cell was until the light on the sample had an intensity of approximately 0.7mW/cm^2. Then the laser aperture was closed and the experimental parameters were set in the Labview program. The Labview program was run and current levels were read for about ten seconds before the voltage supply was turned on. At the end of the 40 minute trial period the data taken for the dark current was saved into a separate file. If after 40 minutes the steady state dark current level had indeed been attained, the program was run again for another 15 minutes. Then the laser aperture was opened, exposing the sample to the light, which causes the PR polymer to generate charges, and the current to increase. Once the photocurrent level had reached a static state, typically after five to ten minutes, the laser aperture was closed again and the dark current was read again for the remainder of time.

Data/Discussion

The dark and photocurrent levels in the non-buffered sample and the buffered sample at six kilovolts are shown in Figure 1.

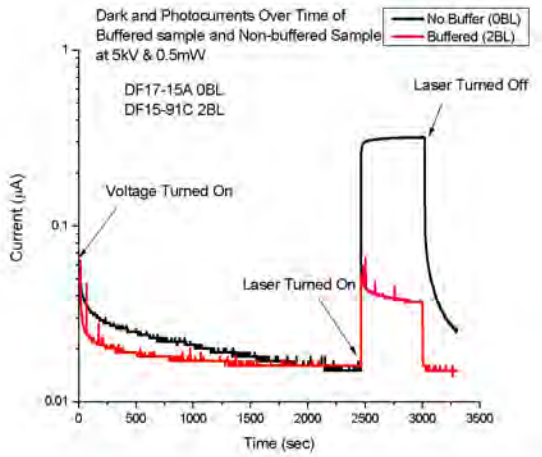

Figure 1. Graph of dark and photocurrents of two- and zero-buffered samples at six kilovolts

It is important to note that the photocurrent is much greater in the sample without APC buffer layers than the buffered sample, confirming that the buffer layer protects against breakdown. Additionally, the degradation of the photocurrent in the buffered sample suggests that it may have more deep traps than the zero-buffer sample. This is perhaps because the charges can become trapped for a long time at the interface between the polymer and buffer layers. Also, the buffered sample appears to have experienced more noise, as indicated by the various spikes. This may be due to charges building up on the APC/polymer interface and irregularly tunneling or hopping through.

The dark and photoconductivity levels at each voltage are shown in Figure 2.

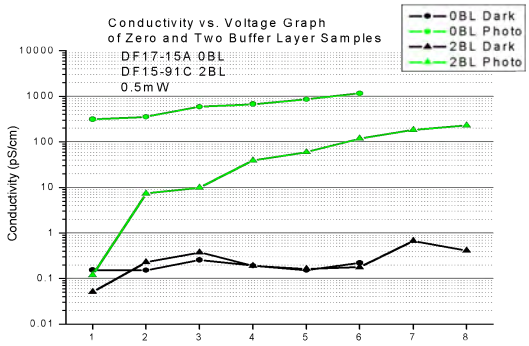

Figure 2. Graph of dark and photoconductivity of two- and zero-buffered samples

These data display a positive trend in photoconductivity with voltage. The sample without buffer layers was only tested up to six kilovolts, as previous experiments show that testing at greater voltages risk destroying the sample. The photoconductivity of the buffered sample is considerably less at all voltages than that of the non-buffered sample. This is perhaps due to increased trap density or trapping rates, owing to the increased deep traps, decreased field strength compared to the non-buffered sample, or other causes. This will affect the response time. In terms of holographic images, this suggests that a PR polymer with a buffer layer would have longer persistency and shorter writing time.

One distinction to be made is the large increase in photoconductivity from one kilovolt to two kilovolts. This may be due to the existence of an energy threshold necessary to either separate the photoexcited charges or overcome the potential barrier of the APC at the electrodes.

The photogeneration efficiency data (Figure 3), like the photoconductivity, also suggest a positive trend with voltage. This is probably due to a decreased field magnitude across the polymer in the buffered sample.

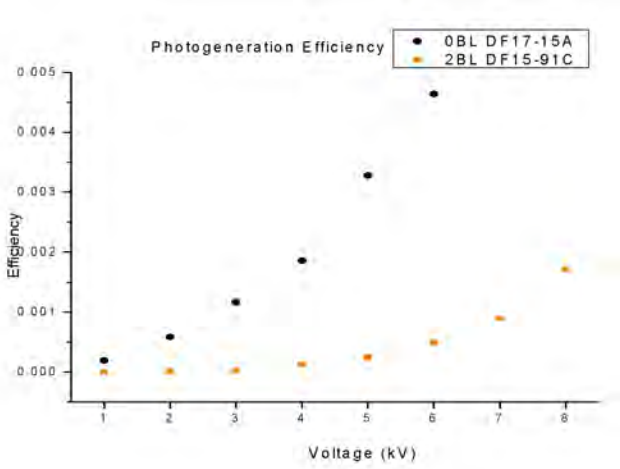

Figure 3. Plot of photogeneration efficiency of two- and zero-buffer layered samples

The lower values for the efficiency of the buffered sample would indicate that holograms would take longer to write as fewer charges are generated in a given time at a particular voltage, which is related to the trapping dynamics as shown in the photoconducitivity.

Conclusion

The photogeneration efficiency and photoconductivity data show that a PR polymer with an APC buffer layer between it and electrodes may increase the amount of time taken to write a hologram to the material, but also may allow higher voltages to be applied to the sample with a much reduced risk of breakdown, potentially increasing the lifetime of the material.

Acknowledgements

This material is based upon work supported by the STC Program of the National Science Foundation No. DMR 0120967, and CHE 0453596, as well as Nitto Denko.

Special thanks to Cory Christensen, Bob Norwood, and Nasser Peyghambarian for their guidance in addition to Pierre-Alexander Blanche, Jayan Thomas, and Ram Voorakaranam for their help.

References

1. Moerner W.A., Grunnet-Jepsen A, Thompson C.L. Annu. Rev. Mater. Sci. 27, 585-623 (1997).
2. Hendrickx Eric, Zhang Yadong, Ferrio Kyle B., et al. J. Mater. Chem. 9, 2251–2258 (1999).
3. Ostroverkhova O., Singer K. D. J. Appl. Phys. 92 (4), 1727-1743 (2002).
4. Fuentes-Hernandez C. Thesis. University of Arizona College of Optical Science.
5. Herlocker Jon. Thesis. University of Arizona College of Optical Science.

VICTOR DENSMORE will be attending the University of Arizona's College of Optical Science in the fall of 2008 where he later intends on applying to graduate school. Victor would like to thank Cory Christenson, Bob Norwood, and Nasser Peyghambarian for engaging him in the innovative field of optics and providing the opportunity to experience graduate school in the College of Optical Science.

Characterization of Third Harmonic-Generation in Amorphous Polymer Films Doped with Push-Pull Chromophores

MICHAEL P. GAJ, University of Arizona
Canek Fuentes-Hernandez, Bernard Kippelen, Georgia Institute of Technology

Nonlinear optics is the study of the interaction between light and matter in the limit where the dielectric polarization induced in the media is nonlinear with respect to the applied optical fields.[1] Unlike the case in linear optics, where the induced polarization $\vec{P}(t)$ linearly depends upon the electric field strength $\vec{E}(t)$, nonlinear optical responses are described by expressing the induced polarization as a power series of the field strength.[2]

$$\vec{P}(t) = \chi^{(1)}\vec{E}(t) + \chi^{(2)}\vec{E}^{2}(t) + \chi^{(3)}\vec{E}^{3}(t) + \cdots \equiv \vec{P}^{(1)}(t) + \vec{P}^{(2)}(t) + \vec{P}^{(3)}(t) + \cdots \quad (1)$$

The fields $\vec{P}^{(2)}(t)$ and $\vec{P}^{(3)}(t)$ are referred to as the second and third-order nonlinear polarizations, respectively, and $\chi^{(2)}$ and $\chi^{(3)}$ are known as the second and third-order nonlinear optical susceptibilities, respectively.[2] Second-order nonlinear optical interactions can occur in crystal materials with a non-centrosymmetric crystal structure, that is materials that lack inversion symmetry. However, third-order nonlinear interactions can occur in any media and do not impose any symmetry requirements.[3] These second and third-order nonlinear optical interactions bring rise to a range of optical phenomena, each distinct from one another.[2]

Interest in nonlinear optics has grown substantially since these phenomena first emerged.[1] Two of the more prominent of these nonlinear optical interactions are Second and Third Harmonic Generation, referred to as SHG and THG, respectively.[2] In SHG, two photons of frequency ω are destroyed, transferring their energy into a newly created photon at the second-harmonic frequency 2ω.[1] SHG is commonly used to convert output optical radiation from lasers into new spectral regions at half the fundamental wavelength. Similarly, in THG three photons of frequency ω are destroyed and their energy is transferred into a new photon traveling with the third-harmonic frequency, 3ω, and at a third of the fundamental wavelength. This process is illustrated in Figure 1. Photonic processes similar to these have gained much interest lately due to their ability to perform processes similar to those of electrons, but several orders of magnitude faster than their electronic equivalent.[1] These new processes present new technological applications that are capable of occurring in nonlinear optical materials. Although second-order nonlinear processes are much more efficient than those third-order nonlinear interactions, their symmetry requirements limit their practicality for many applications; the fabrication process for non-centrosymmetric crystals is expensive and labor some. However, as previously mentioned, there are no symmetry requirements for third-order nonlinear interactions. Consequently, a wide variety of materials can be utilized to produce third-order nonlinear interactions, and in particular THG.[1] The use of polymers to produce these nonlinear interactions allow for useful materials to be molecularly engineered to increase their nonlinear susceptibilities.[1]

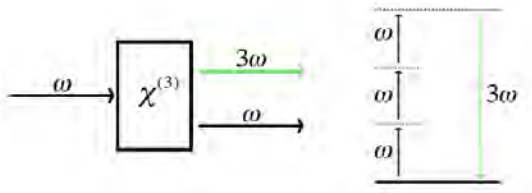

Figure 1: Geometry of THG Interaction and an Energy Level Description

A major development of nonlinear optical polymeric materials occurred in the 1980s with the development of organic conjugated polymers.[3] Highly conjugated π-electron systems display large third-order optical nonlinearities and when connecting donor and acceptor structures favor nonlinear optical responses.[1] In conjugated polymers, the electrons forming the π-bonds in the system delocalize along the molecular structure, resulting in either good electrical conductivity or large optical nonlinearities.[4] For this reason, organic π-conjugated polymers have attracted much attention in the field of nonlinear optics.[3] The π-electrons in these systems are the bonds responsible for the high optical nonlinearities exhibited by the conjugated polymer systems. These π-bonds are especially useful in the develop of push-pull molecules.[4] These push-pull molecules have a permanent dipole, but experience changes in their dipole moments upon optical excitation. Consequently, push-pull systems experience large cubic nonlinearities caused by intramolecular charge transfer in the excited state. Through the use of these polymers the range of potential applications for THG include: ultra-fast pulse characterization; [4] optical switching;[4] optical auto-correlation;[4] ultra-fast data processing;[5] and more recently proposed image restoration.[4] While a large collinear THG is desirable for all applications, those requiring more than one beam interacting in the material require a large noncollinear THG. In this paper, we intend to characterize the noncollinear THG amplitude of a polymer and determine which internal interbeam angle produces the strongest noncollinear THG amplitude.

The material used during experimentation consisted of a polystyrene matrix doped with a 20% weight of the push-pull chromophore 2-tricyanovinyl 3-hexyl-5(4-NN' diphenyl-4-dibutyl) vinyaniline thiophene.[6] The chromophore selected is comprised of an electron

donor group (amino functional groups) and acceptor end-groups (associated with cyanos) connected by a π-electron conjugated bridge; its molecular structure is illustrated in Figure 2.[4] Polystyrene was selected as the molecular matrix due to its inertness, transparency at the third-harmonic wavelength and easy processability in solution.[4] This material exhibits many properties that make it a desirable choice for third-order nonlinear interactions, which include: a large change in static electric dipole moment in the chromophore upon electromagnetic excitation;[4] small differences between the fundamental and third-harmonic indices of refraction; and low absorption at the third-harmonic wavelength. From the dispersion curve of the molecule, measured by spectral ellipsometry and illustrated in Figure 3, the index of refraction at the fundamental wavelength, 1.53 μm, and the third-harmonic wavelength, .510 μm, were determined to be 1.5942 and 1.5704 + .017i, respectively. From these indices of refraction, the absorption (α) at each wavelength can be determined through the following expression:

$$\alpha = \frac{4\pi \cdot n_i}{\lambda} \quad (2)$$

where n_i represents the imaginary component of the index of refraction. Since the fundamental wavelength lies in the infrared region, it is not absorbed in the material. The third-harmonic wavelength, however, does experience absorption since it falls in the visible range of the spectrum. This value was determined to be .00004 cm^{-1}.

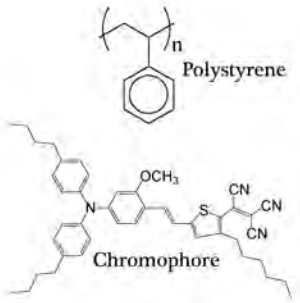

Figure 2: Molecular Structure of Polymer and Push-Pull Chromophore Used in Material

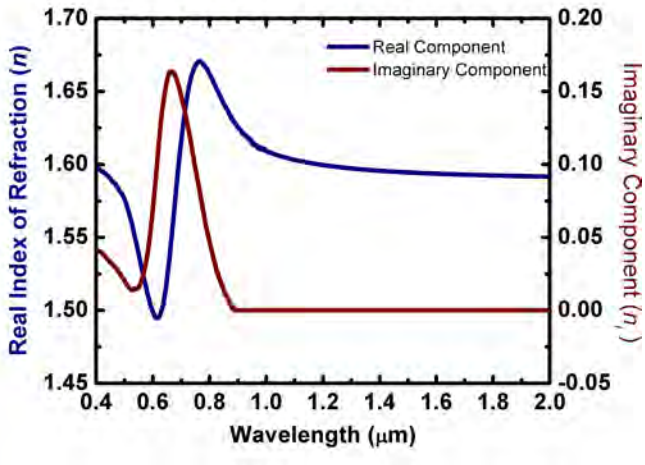

Figure 3: Dispersion Curve for Molecule Used in Experimentation

For the THG characterization, uniform thin films of the material were created by placing a sample in between two glass plates and melting the solids with a hot-plate. To control the thickness of the samples, calibrated bids were placed in between the glass plates. The bid thickness used to create the sample used during experimentation was 10μm. Once the films had been created, the edges of the glass plates were encapsulated with epoxy.
In the collinear geometry, a single beam is focused into a nonlinear medium to produce a THG that propagates in the same direction as the pump. The efficiency of the collinear geometry is controlled by its wave-vector mismatch. For this geometry, the wave-vector is mismatch is defined as the difference between the sum of three wave-vectors with frequency ω and the wave-vector of frequency 3ω.[2] A vector representation of this relation is illustrated in Figure 4. Simplifying this relation shows that this mismatch is effectively the difference between the indices of refraction at the two respected frequencies.

$$\Delta k = \frac{6\pi}{\lambda} \cdot \left(n(3\omega) - n(\omega)\right) \quad (3)$$

In order to measure the power of the collinear THG beam, it must first be separated from the fundamental with a dispersive prism. Since the two beams are traveling at different wavelengths, they will refract with different angles. This allows the collinear THG to be easily isolated from the fundamental and accurately measured. Noncollinear THG appears when two or more laser pulses, traveling in different directions and different wave-vectors, interact and overlap both spatially and temporally into the film.[4] Although both methods successfully create THG, the noncollinear geometry is of more interest.

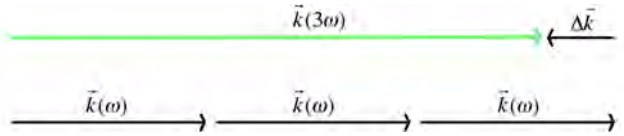

Figure 4: Vector Representation of Collinear Wave-Vector Mismatch

Unlike collinear THG, the wave-vector mismatch (k) produced between two plane-waves in a non-collinear geometry has an angular dependence on the internal interbeam angle (θ) of the beams:

$$\Delta k = k(3\omega) - k(\omega) \cdot \sqrt{5 + 4\cos(\theta)} \quad (4)$$

Consequently, effectively varying the internal interbeam angle can reduce the wave-vector mismatch and substantially increase the efficiency of the process. This unique quality in noncollinear geometries allows for high-resolution optical imaging with broad angular bandwidths.[4] Figure 5 shows the set-up used to create and isolate the collinear and noncollinear THG beams. The pulsed beam was created by an optical parametric oscillator (OPAL) pumped by a Ti:Sapphire laser (Tsunami) with a pulse width of 100fs and a repetition rate of 82MHz. A computer-controlled wave-plate and a polarizer were introduced at the laser output to clearly define the polarization of the incoming beam and control its intensity. This assisted in the characterization for both collinear and noncollinear THG. The beam was then spatially filtered using a 100μm pinhole

to create a beam with a very well-defined Gaussian intensity profile. The beam was then focused into the rectangular diffraction grating, inserted into the system to diffract the fundamental beam into four first-order beams used to create noncollinear THG. A detailed schematic of this process is shown in Figure 6. These beams are collimated by a lens of focal length *fc* before they proceed to a mask that blocks all but two of the first-order beams. A lens with focal length f_f then focuses them into the sample.

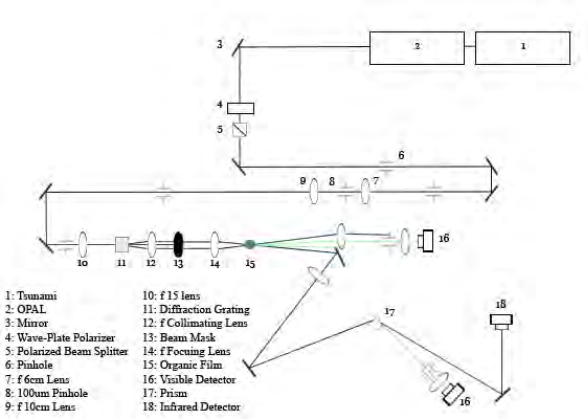

Figure 5: Optical Set-up Used to Produce and Isolate Collinear and Noncollinear THG

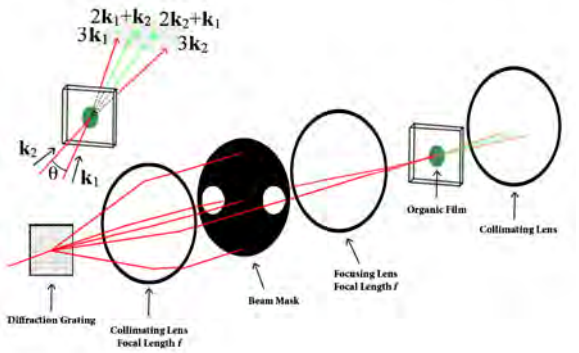

Figure 6: Schematic Representation of Optical Set-up Used to Create Noncollinear THG and Wave-Vector Diagram for Noncollinear Geometry

The propagation of this Gaussian beam was characterized through using the razor blade test and found to be in good agreement with Gaussian beam propagation theory. These results allowed for the beam's 1/e radii to be approximated at the sample using the relation:

$$\omega_o = \frac{\lambda \cdot f_f}{2 \cdot r_{ep}} \quad (5)$$

where r_{ep} represents the 1/e radius at the lens' entrance pupil. By varying the focal lengths of the collimating and focusing lenses, the internal interbeam angle incident upon the sample can be altered. Due to fabrication imperfections, the diffraction grating diffracts approximately 10% of the input energy into each of the first-order beams.[7] Consequently, the extent to which the internal interbeam angle could be altered was significantly restricted by low power levels.

As shown in the inset, the propagation directions for the four beams are in the directions $3\mathbf{k}_1$, $3\mathbf{k}_2$, $2\mathbf{k}_1+\mathbf{k}_2$ and $2\mathbf{k}_2+\mathbf{k}_1$, where $\mathbf{k}_1$ and $\mathbf{k}_2$ represent the wave-vectors of the fundamental beams. These four beams represent the four different ways to produce a beam with a frequency of 3ω, with beams propagating in directions $2\mathbf{k}_1+\mathbf{k}_2$ and $2\mathbf{k}_2+\mathbf{k}_1$ producing noncollinear THG and beams propagating in $3\mathbf{k}_1$ and $3\mathbf{k}_2$ producing collinear THG.[6] This quality allowed for both noncollinear and collinear THG powers to be recorded with the same optical set-up.

The collinear geometry was the first geometry to be investigated by removing the diffractive grating and using a 10 cm focal length lens to both collimate and focus the Gaussian beam onto the sample. As previously illustrated in Figure 5, the THG and fundamental beams were separated by a prism and collected with the use of calibrated visible and infrared detectors, respectively. Through measurements attained from both beams, a relationship between THG power and pump beam irradiance (pump power over beam area) was obtained. The experimental data, shown in Figure 7, revealed the expected cubic dependence. Normalizing these results to beam irradiance as opposed to pump power provided a THG power characterization independent of geometry. The THG power expression obtained through these experimental results is given below in equation 6:

$$P = A \cdot (x - x_o)^z \quad (6)$$
$$\text{with } A = 5.2\text{x}10^{-18},\ x_o = -10.4$$
$$z = 3.0$$

Using these results, the $\chi^{(3)}$ for the material can be estimated.

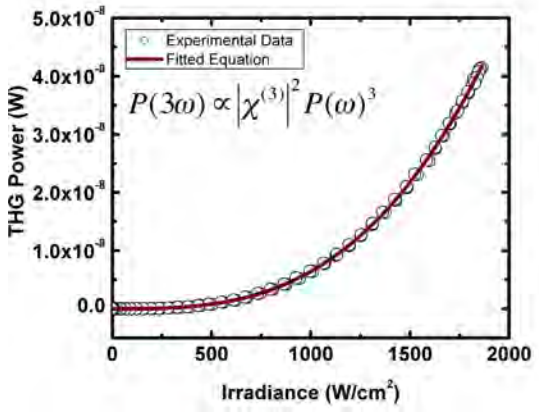

Figure 7: Characterization of THG Power as a Function of Incident Beam Irradiance

With a fundamental power, P(ω), of 95.5mW, a third-harmonic power, P(3ω), of 3.4nW was measured. Inserting these values into the following expression:

$$\chi^{(3)} = \frac{4 \cdot n(3\omega) \cdot c \cdot \lambda}{3\pi} \cdot \left(\frac{P(3\omega) \cdot n(\omega)}{P(\omega) \cdot n(3\omega) \cdot L^2 \operatorname{sinc}^2\left(\frac{\Delta k \cdot L}{2}\right)} \right)^{1/2} \quad (7)$$

where Δk is the wave-vector mismatch given by equation 3 and L is the sample thickness, revealed $\chi^{(3)} = 9.0 \times 10^{-12}$ *esu*.

For the noncollinear geometry, the diffractive grating was inserted into the set-up and the interbeam angle varied as previously described. The experimental data points attained for the noncollinear and collinear THG at 7.66° are illustrated above in Figure 8. The normalized noncollinear THG data was obtained for this geometry by taking the ratio between these two curves. Figure 9, provided below, shows the experimental data points (circles) obtained at each internal interbeam angle. Using a plane-wave approximation, the ratio between the THG power and the fundamental is given by the complex conjugate of the following equation:

$$F = \frac{\left(1 - e^{i\Delta k \frac{L}{\cos(\beta)}}\right) \cdot e^{-ik(3\omega)\frac{L}{\cos(\beta)}}}{n^2(3\omega) - \left(\frac{5 + 4\cos(\theta)}{9}\right) \cdot n^2(\omega)} \quad (8)$$

where $\beta = \tan^{-1}([\tan(\theta/2)]/2)$ and Δk represents the wave-vector mismatch given in Equation 4. Figure 9 also shows the predictions of this theoretical model for a 10μm thick sample (dashed line). Comparing these results to the experimental data revealed a large disparity between the two data sets. Upon further investigation, the sample thickness was measured to be approximately 32μm. This increase in thickness is most likely the result of thermal expansion caused by the intense laser pulses. As evident in Figure 9, the theoretical model using this thickness (solid line) yields a stronger correlation to the experimental data. There is still, however, a slight difference between the two data sets, indicating the plane-wave approximation used in deriving the model is not entirely valid. In order to obtain a more accurate expression with a stronger correlation to the experimental data, the theoretical equation will need to be re-modeled to describe the diffractive nature of the grating used in the optical set-up.

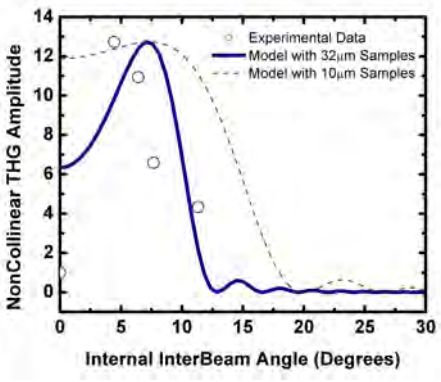

Figure 8: Experimental Data Illustrating Collinear and Noncollinear THG Power as a Function of Wave-plate angle with an internal interbeam angle of 7.66°

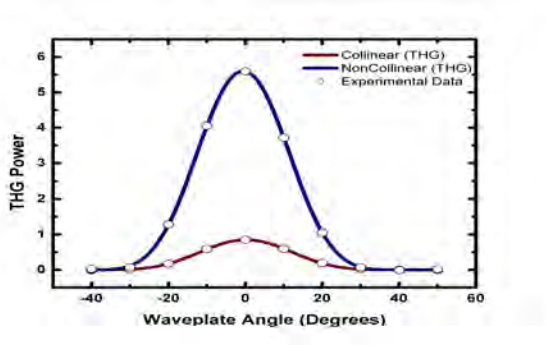

Figure 9: Noncollinear THG Amplitude as a function of Internal InterBeam Angle

In conclusion, an optical set-up was constructed to measure the THG produced from an amorphous polymer film doped with push-pull chromophores. Through these measurements, a characterization of the collinear and noncollinear THG in a polymer composite was obtained. With these THG power measurements, the $x^{(3)}$ of the material was experimentally estimated to be 9.0×10^{-12} esu. The noncollinear THG amplitude of the molecule was investigated and characterized as a function of internal interbeam angle. By doing so, the initial assumption of a 10μm sample thickness was shown to be inaccurate and a new sample thickness of 32μm was measured. Moreover, the plane-wave approximation used to derive the theoretical model was shown to be invalid with the use of a diffractive grating. In order to obtain a more accurate fit to the experimental data, the theoretical expression will need to be re-modeled to describe the characteristics of the diffractive grating used in the optical set-up.

Acknowledgements

Research support is gratefully acknowledged from the National Science Foundation's Center for Materials and Devices for information Technology Research (CMDITR) DMR-0120967. The author would also like to thank Canek Fuentes-Hernandez, Bernard Kipplen as well as the rest of the Kippelen Research lab for their assistance and support throughout the summer.

References

1. M. B. ROSA. ORGANIC MATERIALS FOR NONLINEAR OPTICS. SPRINGER, NETHERLANDS 2008
2. R.W. BOYD. NONLINEAR OPTICS. ACADEMIC, BOSTON. 1990.
3. H. S. NALWA. ADVANCED MATERIALS. 5. ISSUE 5, 341. (1993)
4. G. RAMOS-ORTIZ. PH.D. THESIS. UNIVERSITY OF ARIZONA. 2003.
5. C. FUENTES-HERNANDEZ, S. Y. TSENG, D. OWENS, B. KIPPELEN. APPL PHYS LETT. 91, (2007).
6. G. RAMOS-ORTIZ, M. CHA, B. KIPPELEN, G. A. WALKER, S. BARLOW, S. R. MARDER. APPL PHYS LETT. 29, 2525 (2004).
7. S. Y. TSENG, C. FUENTES-HERNANDEZ, B. KIPPELEN. OPTICS LETTERS. 32, 17. (2007).

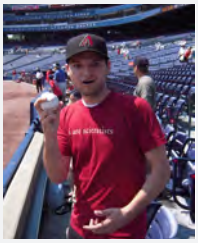

MICHAEL GAJ is a junior double degreeing in Optical Sciences and Engineering and Applied Mathematics at the University of Arizona.

Synthesis of Benzo[1,2-b:4,5-b']dithiophene Derivatives for OFET Applications

TAYLOR GIDDENS, Georgia Institute of Technology
Yulia Getmanenko, Seth Marder, Department of Chemistry and Biochemistry, Georgia Institute of Technology

Introduction

Technological advances are increasingly made possible through the use of organic semiconductors, which are used in such devices as organic photovoltaics (OPV), organic light emitting diodes (OLED), and organic field effect transistors (OFET).[1, 2] These devices generally have the advantage of being relatively inexpensive to produce (i.e. via solution processing) in comparison to their inorganic counterparts. Thiophene containing organic compounds are well known for their electronic properties and have been used as organic semiconductors in OFET devices[2]. Benzodichalcogenophenes, the target of this research, are a relatively young class of organic semiconducting materials, of which the sulfur containing homologue has recently been tested in OFET devices demonstrating charge mobility of 0.016 cm^2/Vs with relatively good stability.[3] Recently Pan *et al.* have reported efficient OFET based on a polymer (see Figure 1) with a benzodithiophene containing core (top contact configuration, on/off ratio 10^5-10^6, mobility 0.15-0.25 cm^2/Vs)[4].

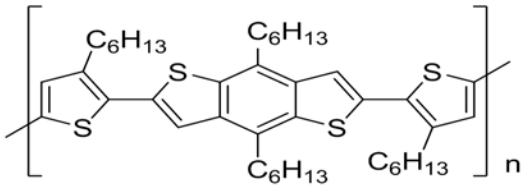

Figure 1. Structure of Poly(4,8-dialkyl-2,6-bis(3-alkylthiophen-2-yl)benzo[1,2-b:4,5-b'] dithiophene).

It is expected that the increased intermolecular interaction of larger chalcogenides, selenium and tellurium, will aid in charge transport. Recently a convenient method for the general preparation of benzodichalcogenophenes was reported[5], shown here in Scheme 1. In this method acetylene substituents on benzene rings simply undergo intramolecular cyclization with dicarbanion intermediates to form heterocyclic aromatic systems. This research will focus on the preparation of the materials containing these aromatic cores, expansion of the known synthetic route for the preparation of various substituted benzodichalcogenophene cores, computational study of the proposed materials, and examination of their charge transport.

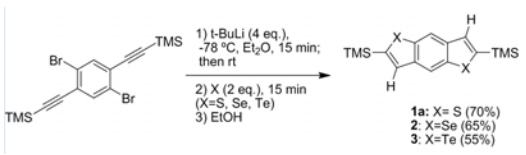

Scheme 1. General synthetic route to benzodichalcogenophenes.[5]

Results and Discussion

Synthesis

The general method reported in the literature[5] can be expanded by making several simple variations, including the use of different R groups rather than TMS and the trapping of the carbanion intermediate with different electrophiles, as shown in Scheme 2. It is anticipated that electronic properties and solubility can be tuned by varying the size and nature of the E-group and R-group (Scheme 2).

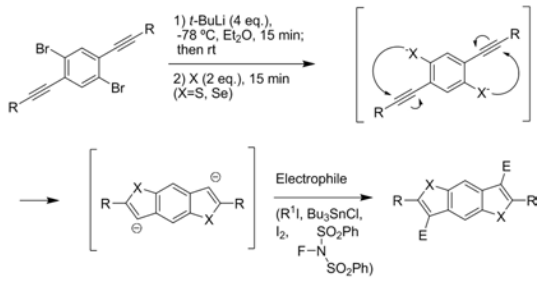

Scheme 2. Proposed flexible strategy for the synthesis of tetrasubstituted benzodichalcogenophene cores.

First, results from literature were reproduced to synthesize **1a** and the necessary precursors, as shown in Scheme 3. The low yield of **1a** may have been due to the substitution of ether in the literature with THF. Upon reproduction of literature results, iodine was attempted as a carbanion quenching agent rather than ethanol to install a group other than hydrogen at positions 3 and 7 of the aromatic core. HRMS and ^{1}H NMR showed no product **6**. Conditions need to be further investigated. The TMS groups at positions 2 and 6 of **1a** were converted to iodine by reacting ICl with it and the positions were subsequently substituted with 5-*n*-nonylthiophen-2yl and 5-*n*-pentadecylthiophen-2-yl to produce **8a** and **8b** as shown in Scheme 4. NMR was not successfully performed to date due to the low solubility of these compounds was poor in chloroform even at elevated temperatures.

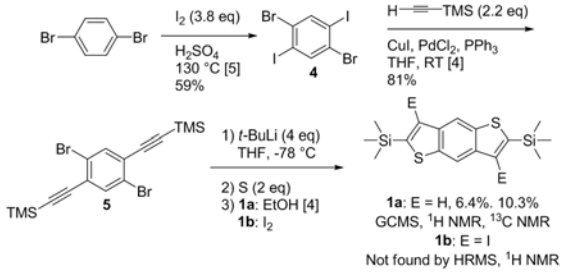

Scheme 3. Synthesis of 2,6-bis(trimethylsilyl)benzo [1,2-b:4,5-b']dithiophene and precursors.[5, 6]

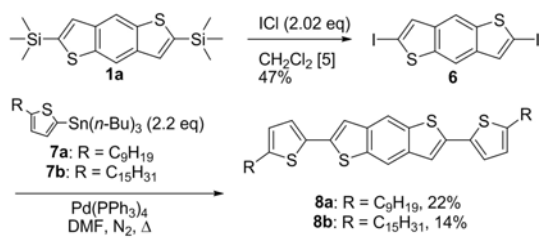

Scheme 4. Synthesis of 2,6-bis(trimethylsilyl)benzo [1,2-b:4,5-b']dithiophene and precursors.[5, 6]

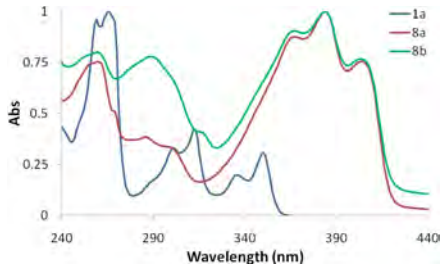

Figure 2. UV-vis of 1a, **8a**, and **8b** in THF.

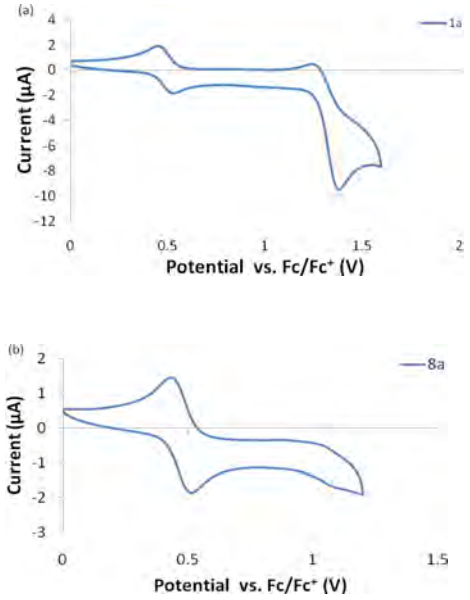

Figure 3. Cyclic volatammetry with internal ferracene of (a) **1a** and (b) **8a** in dichloromethane.

Electrochemical and Photochemical Properties

UV-vis spectra of **8a** and **8b** in THF show a red shift compared to **1a** as expected due to the extension of the π-conjugation. Cyclic voltammetry of **1a** in a 0.1 M solution of tetra-zbutylammonium hexafluorophosphate in dichloromethane with a scan rate of 50 mVs^{-1} showed a reversible oxidation peak at 0.82 V relative to the $E_{1/2}$ of ferracene (seen near 0.5 V in Figures 3a and 3b). The relative height the reversibleoxidation and reduction waves of 1a comes closer to unity at a scan rate of 1500 mVs^{-1}, which gives an estimated lifetime of the radical cation of approximately 0.38 s. CV of **8a** under similar conditions showed an irreversible oxidation peak at 0.6 V relative to ferracene. Poor solubility of **8a** may have caused a poor signal. Different acetelyne derivatives have yet to be explored in place of acetylene-TMS to vary substituents at positions 2 and 6 of the benzodichalcogenophene cores. This series of experiments could then be extended to the selenium and telurium homologues. Charge mobility of **8a** and **8b** will be measured in OFET.

Computation

Quantum chemical calculations were performed for variations of the benzodichalcogenophene cores as shown in Figure 3 using the NWChem computational package. The ground state (S_0) and the ±1 charge states equilibrium geometries for each compound were optimized at the ab initio density functional theory (DFT) level. Split valence polarized 6-31G(d) (6-31G*) basis set was employed for all atoms except for I, Se, Te (6-311G* for I, Se atoms; 3-21G for Te atoms) with DFT using the B3LYP hybrid exchange correlation functional. The total energies of the molecules from these calculations are used to calculate HOMO/LUMO energies and bandgaps (Figure 5), the electron affinity (EA), and ionization potential (IP) (Figure 6) for these molecules. Table 1 shows the correlation between the calculated energies and the observed experimental energies reported in literature. Calculations made using DFT methods are known to inaccurately calculate LUMO levels as higher than actual levels, thereby increasing the calculated bandgaps. However, the general trend is correct and calculated values can be used qualitatively. The calculations show that the larger the chalcogenide, the smaller the bandgap. F, I, and CF_3 were all calculated to stabilize the benzodichalcogenophene core compared to H as substituents on the 3 and 7 positions stabilizes molecule, as seen in Figure 4. While F and I were predicted to stabilize the molecule and decrease the bandgap, CF_3 was predicted to stabilize the molecule without significantly affecting the bandgap. Also, I was calculated to stabilize the molecule more than F.

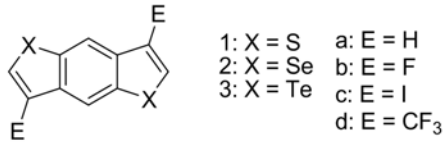

Figure 4. Structures of benzodichalcogenophenes studied in DFT calculations.

	HOMO/eV		Eg/eV		LUMO/eV	
	Calc	Exp	Calc	Exp	Calc	Exp
1a	-5.47	-5.6	4.39	3.6	-1.08	-2
2a	-5.42	-5.5	4.27	3.5	-1.16	-2

Table 1. Calculated and experimental[7] energetic structure of benzodichalcogenophenes.

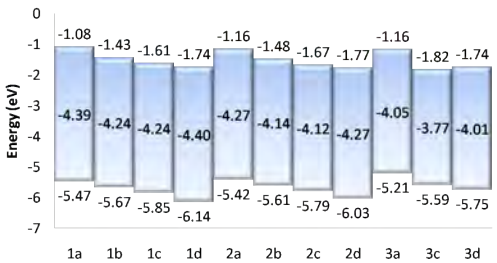

Figure 5. Calculated HOMO and LUMO levels of benzodichalcogenophenes **1a-3d**.

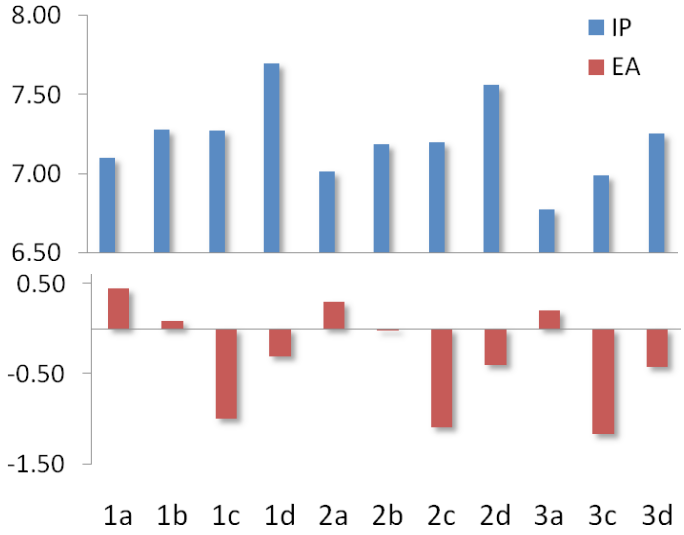

Figure 6. Calculated relaxed ionization potentials and electron affinities of benzodichalcogenophenes **1a-3d**.

Conclusion

The synthetic route to benzodithiophene core works, but the method/technique remains to be optimized. It is still unknown if quenching with electrophiles following cyclization is an effective method to introduce substituents to the core. Calculations may be a useful qualitative prediction tool for tailoring properties for new cores and choosing new benzodichalcogenophene core containing molecules to synthesize.

Experimental

1,4-Dibromo-2,5-diiodobenzene (4)[5]

Iodine (24 g, 94.5 mmol, 3.8 eq) and 1,4-dibromobenzene (24.6 mmol, 5.8 g) were added to a round bottom flask. Concentrated sulfuric acid (80 mL) was added and a condenser was attached. The deep purple mixture was heated for 5 hours. The flask was placed in ice and allowed to cool before pouring the mixture into 1 L of ice. The solid was vacuum filtered after ice was allowed to melt and washed with sodium thiosulfate (5 g in 50 mL water, then 20 g in 200 mL water). The sample was finely crushed and washed with sodium thiosulfate several times until the purple color was nearly removed. The crude material (light pink solid) was refluxed with benzene (20 mL), magnesium sulfate was added, and the mixture was gravity filtered while hot. The solution was cooled to room temperature, then in an ice bath and the off white needle-shaped crystalline material was vacuum filtered **4** (7.09 g, 59%): ^{1}H NMR ($CDCl_3$, 400 MHz): δ 8.04 (s, 2H); ^{13}C NMR ($CDCl_3$, 100 MHz): δ 142.3, 129.2, 101.3.

1,4-Dibromo-2,5-bis(2-trimethylsilylethynyl) benzene (5)[5]

$PdCl_2$ (35 mg, 0.2 mmol, 2.9 mol%), PPh_3 (130 mg, 0.5 mmol, 7.3 mol%), and 1,4-dibromo-2,5-diiodobenzene (**4**) (3.33 g, 6.8 mmol) were added to a three neck round bottom flask and stirred for 20 minutes under nitrogen. Diisopropylamine (20 mL) was added and trimethylsilylacetylene (1.34 g, 13.6 mmol) was added 10 minutes later, followed by the addition of CuI (74 mg, 0.388 mmol, 5.7 mol%). An additional amount of trimethylsilylacetylene (0.15 g) was added after 3 hours. Saturated NaCl solution (20 mL) was added and the organic phase was separated. Then aqueous phase was extracted 4 times with diethyl ether. The combined organic phases were washed with water, dried over $MgSO_4$, and the solvents were removed by rotary evaporation. The residue was dissolved in chloroform (20 mL) and toluene (10 mL) and purified by column chromatography twice (hexanes). The solvent was removed from combined fractions by rotary evaporation and **5** was obtained as off white crystals (2.36 g, 81%). ^{1}H NMR ($CDCl_3$, 400 MHz): δ 7.65 (s, 2H), 0.25 (s, 18H); ^{13}C NMR ($CDCl_3$, 100 MHz) δ 136.2, 126.3, 123.5, 102.9, 101.2,-0.46. GC-MS *m/z* 428 (M^+). This analysis is in agreement with the literature data.[8]

2,6-Bis(trimethylsilyl)benzo[1,2-b:4,5-b']dithiophene (1a)[5]

1,4-Dibromo-2,5-bis(2-trimethylsilylethynyl)benzene (**5**) (0.5 g, 1.17 mmol) was placed in a round bottom flask, anhydrous THF (15 mL) was added, and the mixture was placed in a dry ice/acetone bath to cool under stirring to -76 °C. *t*-BuLi in a pentane solution (3 mL, 4.68 mmol, 1.5 M, 4 eq) was added dropwise and stirred at -76 °C for 15 min, giving an orange solution with suspended precipitate. Gradually the mixture was allowed to warm to room temperature which dissolved precipitate and changed color to clear brown. Then sulfur powder (75 mg, 2.34 mmol, 2 eq) was added producing a deeply yellow brown solution and the mixture was stirred for 15 minutes. Ethanol (30 mL) was added, removing the yellow coloration. The sample was then stirred for one hour. Water was added and organic matter was extracted with chloroform. The solution was dried with magnesium sulfate, gravity filtered, and rotary evaporated. The residue was purified by column chromatography (100 mL silica gel, hexanes). The solid was then recrystallized from hexanes to give light brown needle shaped crystals (0.025g, 6.4%). ^{1}H NMR ($CDCl_3$, 400 MHz): δ 8.25 (s, 2H), 7.44 (s, 2H), 0.38 (s, 18H); ^{13}C NMR ($CDCl_3$, 100 MHz) δ 143.6, 140.6, 139.1, 129.8, 116.0, -0.39. GC-MS analysis showed the presence of two materials: the desired product (**1a**) *m/z* 334 (M^+) and a byproduct, trimethyl((2-(trimethylsilyl)benzo[b]thiophen-6-yl)ethynyl)silane *m/z* 302 (M^+).

3,7-diiodo-2,6-Bis(trimethylsilyl)benzo[1,2-b:4,5-b']dithiophene (1b)

Anhydrous THF was added to 1,4-Dibromo-2,5-bis(2-trimethylsilylethynyl)benzene (**5**) (0.5g, 1.17 mmol) in a round bottom flask under nitrogen. The solution was placed in a dry ice/acetone bath. *t*-BuLi in a pentane solution (3.1 mL, 4.68 mmol, 1.5 M, 4 eq) was added dropwise at -70 °C, changing the solution from light yellow to orange. Sulfur (0.085g, 2.6 mmol) was added to the solution. A solution of iodine (0.653g, 2.6 mmol) in anhydrous THF (15 mL) in nitrogen atmosphere was added to the solution dropwise at -74 °C. The dark brown iodine solution was readily consumed, leaving the color of the reaction solution only slightly deeper than before the addition. Sodium thiosulfate solution (5 g in 50 mL water) was added at -70 °C and solution was removed from ice bath to warm to room temperature. The mixture was then separated and the aqueous portion was extracted with hexanes (3 x 30 mL) and ethanol (1 x 30 mL). The solvent was removed using rotary evaporation. The solid

was dissolved in isopropanol and chloroform, gravity filtered over boiling isopropanol, and recrystallized to give the product, **1b**, as a yellow powder with some visible crystals (0.124g, 18.8%).

2,6-diiodobenzo[1,2-b:4,5-b']dithiophene (6)[9]

To DCM, 2,6-Bis(trimethylsilyl)benzo[1,2-b:4,5-b']dithiophene (**1a**) (0.04 g, 0.12 mmol) was added and cooled in an ice bath. A solution of ICl (0.0393 g, 0.24 mmol) in DCM (5 mL) was added, producing an opaque purple mixture with precipitate. The mixture was vacuum filtered and washed with ethanol (3 x 3 mL) giving a grey/off-white powder (0.025g).

2,6-Bis(5-*n*-nonylthiophen-2-yl)benzo[1,2-b:4,5-b']dithiophene (8a)

Tributyl(5-nonylthiophen-2-yl)stannae (0.0621 g, 0.124 mmol), $Pd(PPh_3)_4$,(.0001 g, 0.086 µmol, 0.1 mol%) and 2,6-diiodobenzo[1,2-b:4,5-b']dithiophene (**6**) (0.025 g, and 0.0566 mmol) were added to a round bottom flask and placed in nitrogen atmosphere. Anhydrous DMF (5 mL) was added and solution was heated with a heat gun, changing the color from a cloudy off white to clear yellow. Ice was added (5 g). The mixture was then vacuum filtered giving an olive green powder. Column chromatography was performed in silica gels (10 mL) eluted with hot $CHCl_3$. The solution was gravity filtered over boiling isopropanol and vacuum filtered giving **8a** as a yellow powder (12.4 mg, 22%). HRMS (EI) *m/z* 606.24872 (M^+) (calculated 606.24824).

2,6-(5-*n*-pentadecylthiophen-2-yl)-benzo[1,2-b:4,5-b']dithiophene (8b)

Tributyl(5-pentadecylthiophen-2-yl)stannae (0.058 g, 0.10 mmol), $Pd(PPh_3)_4$, (.0026 g, 2.3 µmol, 5.0 mol%) and 2,6-diiodobenzo[1,2-b:4,5-b']dithiophene (**6**) (0.02 g, and 0.045 mmol) were added to a round bottom flask and placed in nitrogen atmosphere. Anhydrous DMF (4 mL) was added and solution was heated with a heat gun, changing the color from clear yellow to olive green. Water was added (4 mL). The mixture was then vacuum filtered, giving an olive green powder, and rinsed with ethanol. Column chromatography was performed in silica gels (7 mL) eluted with hot $CHCl_3$ (300 mL). The solution was gravity filtered over boiling isopropanol and vacuum filtered giving **8b** as a yellow powder (8.5 mg, 14%). HRMS (EI) *m/z* 774.44151 (M^+) (calculated 774.43604).

Acknowledgments

Taylor Giddens would like to acknowledge the CMR and MDITR Staff, Dr. Yulia Getmanenko, Dr. Seth Marder, and Dr. Jean-Luc Bredas. This material is based upon work supported by the STC Program of the National Science Foundation No. DMR 0120967.

References

1. John , E. A., Angewandte Chemie Int. Ed., 2008, 47, 3, 452-483.
2. Roncali, J., P. L., and A. C., Adv. Mat., 2007, 19, 16, 2045-2060.
3. Yamaguchi, K., et al., Jap. J. App. Phy. Part 2-Let. & Express Let., 2007, 46, 29-32, L727-L729.
4. Pan, H., Y. L., Y. W., P. L., B. S. O., S. Z., G. X., J.A.C.S., 2007. 129, 4112-4113.
5. Takimiya, K., Y. K., H. E., N. N., T. O., J. O. Chem., 2005, 70, 10569-10571.
6. Hart, H., K. H., and C. J. F. D., J. O. Chem., 1985, 50, 17, 3104-3110.
7. Ebata, H., et al., Org. Let., 2007, 9, 22, 4499-4502.
8. Goldfinger, M.B., K.B.C., and T.M.S., J.A.C.S, 1997, 119, 20, 4578-4593.
9. Takimiya, K., et al., Chem. Let., 2006, 35, 10, 1200-1201.

TAYLOR GIDDENS has educational goals including earning a bachelor's degree in materials science and engineering, and a Ph.D. in chemistry.

The Effect of Processing Parameters on the Properties of Transparent SWNT Electrodes

JOSHUA GOMBERG Cornell University
Roderick Jackson, Samuel Graham, School of Mechanical Engineering, Georgia Institute of Technology

Abstract

Randomized single-walled carbon nanotube (SWNT) networks are a promising material in the field of transparent electrodes. These networks contain bundles of nanotubes which affect the overall conductivity of the film. A parametric study was carried out to analyze two parameters that affect conductivity: sonication time and SDS concentration. Electrodes were made with SDS concentrations of 0.25%, 0.5% and 1% and with sonication times of 30 minutes, 60 minutes, and 120 minutes. Sheet resistance and transmittance were measured for these electrodes, and conductivity was calculated using these data.

Introduction

Transparent electrodes are a necessary component in various electronic devices including light emitting diodes, solar cells, LCD and touch screen displays. With the development of flexible electronics, there is a need to extend the application space of transparent to accommodate the specific needs of flexible devices. At present, indium tin oxide (ITO) is the most commonly used transparent electrodes. However, like most transparent conductive oxides, ITO has limited flexibility and thus, alternatives for flexible applications are being developed. Another motivating factor in the search for alternatives to ITO is the rapidly increasing price of indium.

Carbon Nanotubes

One of the most promising materials for highly flexible transparent electrodes is a random network of single-walled nanotubes (SWNTs).[1] SWNT networks have great electrical conductance, optical transparency, flexibility, and fault tolerance.[1]

The wrapping vector, a measure of chirality which determines the direction a planar sheet of graphene is "rolled up" to form a carbon nanotube, can be expressed by the equation[2] as described in Figure 1:

$$C = n\hat{a}_1 + m\hat{a}_2 \qquad (1)$$

It can be expected[3] that carbon nanotubes display metallic electronic properties if the following equation holds true:

$$n - m = 3\ell \quad (\ell \text{ is an integer}) \qquad (2)$$

In cases where this equation does not hold, nanotubes display semiconducting behavior.

In general, any mixture of nanotubes contains roughly 1/3 metallic and 2/3 semiconducting nanotubes. Despite the fact that a minority of nanotubes display metallic behavior, there exists a percolation threshold where the film displays metallic properties as the number of metallic pathways increases with increasing film density as seen in Figure 2.

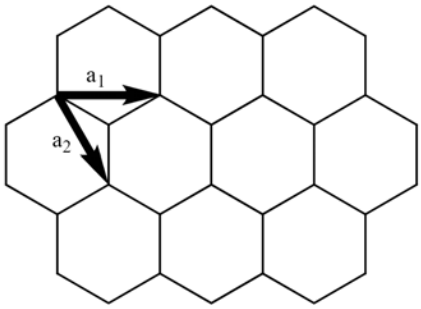

Figure 1. The unit vectors for determining the chirality.

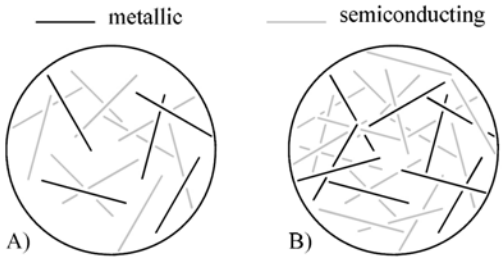

Figure 2. Sketch of an SWNT network A) below and B) above the percolation threshold. Metallic behavior dominates in B) due to the greater number of metallic pathways.

One method for forming a sufficient percolation network of metallic nanotubes is through the vacuum filtration of dispersed solutions of SWNTs. This is a complicated process which involves dissolution of the SWNTs in a surfactant solution followed by sonication, centrifugation, vacuum deposition onto the filter and finally transfer onto a glass or plastic substrate.

However, SWNT networks formed from vacuum filtration of a solution of nanotubes is comprised of individual SWNTs, because solvated nanotubes have a tendency to aggregate into bundles. Hecht et. al[4] have proposed that bundle diameter has an effect on conductivity. It is believed that the bundle diameter in the final SWNT network depends greatly on several factors that occur during the manufacturing process. Primary among these are the time in which the SWNT solution is sonicated and the amount of surfactant in the suspension.

Objective

Sodium Dodecyl Sulfate, SDS, is a common surfactant used to facilitate dissolution of nonpolar nanotubes in water. Adversely, SDS can interfere with nanotube-nanotube contacts and thereby raise sheet resistance since water alone cannot fully remove remnant SDS from the film. Additionally, sonication can break up both nanotube bundles and eventually the carbon nanotubes themselves through mechanical fatigue. To date, there has been no parametric study to elucidate the impact of sonication time and the SDS concentration in the SWNT solution on film performance. The subject of this research project was to address the needs for this parametric study in order to help optimize the processing conditions for SWNT transparent electrodes.

Notes on Sheet Resistance

The resistance of an isotropic material with uniform cross-sectional area can be found using the well-known formula,

$$R = \frac{\rho L}{A} \qquad (3)$$

where ρ is the resistivity, L is the length of the material, A is the cross-sectional area, and R is the resistance. For a rectangular region of a thin film,

$$A = W \cdot t \qquad (4)$$

where w is the width of the region and t is the thickness of the film, and thusly,

$$R = \frac{\rho}{t} \cdot \frac{L}{w} \qquad (5)$$

Because the length and width have identical values in a square-shaped region, its resistance can therefore be calculated as

$$R_S = \frac{\rho}{t} \qquad (6)$$

This value, called sheet resistance, is typically used to express the resistance of a thin film and can be used to find the resistance across any rectangular region using the formula

$$R = \frac{1}{w} \cdot R_S \cdot L \qquad (7)$$

At the length scales under consideration for transparent electrodes, the randomized SWNT network can be modeled as a 2-D isotropic film. Using the transfer line method (TLM), if several contacts of a constant width of 1 cm are deposited on the film with varying distances between each contact, then the sheet resistance can be found using the equation,

$$R_S = \frac{dR}{dL} \qquad (8)$$

where L is the length, measured in cm, between successive contacts. A sample Equation 8 can be applied by fitting a least-squares line to a plot of measured resistance between the contacts vs. length. The slope of said line is therefore equal to the sheet resistance. To ensure the most accurate sheet resistance measurements, a thin line must be scratched off the film above and below contacts.

From the sheet resistance, the effective dc conductance can be found using the equation

$$\sigma_{dc} = \frac{188\sigma_{op}}{R_S\left(\frac{1}{\sqrt{T}} - 1\right)} \qquad (9)$$

where T is the transmittance (for this project taken at a wavelength of 550 nm) and σ_{op} is the optical conductivity, which is equal to 200 S/cm.[4]

Procedure

1 mg P3-SWNTs (Carbon Solutions, Inc.) was massed out and placed into each of 9 vials. 3 vials each were then filled with 2 mL of 0.25%, 0.5%, and 1% SDS in distilled water, respectively. The 3 vials of each SDS concentration were then sonicated in a bath sonicator (VWR Model 75D) for 30 minutes, 60 minutes, and 120 minutes, respectively, on sonication setting 5. The samples were then placed in a centrifuge (VWR Galaxy 16D) for 1 hour at 16000g. The top 80% of the solution was retained following centrifugation.

For each of the 9 samples, 3-4 SWNT films were prepared in the following manner: for each film, a 1 μm cellulosic filter (GE Water & Processing Technologies) was placed over a vacuum and a dilute solution of SWNTs and DI water was filtered. To wash away any excess SDS that may be present in the film, an additional 30 mL of distilled water was poured over the film. The filter was then removed from the vacuum and dried on a hot plate.

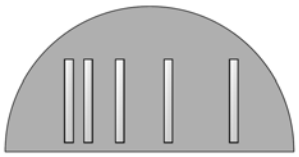

Figure 3. Diagram of silver contacts deposited on a SWNT film cut in half. The Ag lines are spaced 0.09, 0.29, 0.49 and 0.69 cm apart.

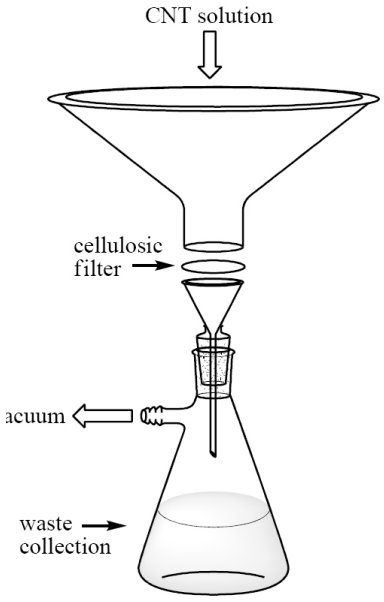

Figure 4. Vacuum filtration set-up for the formation of a SWNT network.

Each film was then placed face-down on a glass slide and wetted with isopropyl alcohol. After allowing excess the excess liquid evaporate, the slides were then placed over acetone vapor (generated by a beaker of acetone being heated on a hot plate) until the filter turned translucent, and then submerged in liquid acetone for 5-10 minutes. To promote adhesion, the slides were then placed on a hot plate to partially dry before being returned to the successive acetone baths for complete filter dissolution. Silver lines were then deposited on the transferred films for TLM sheet resistance measurements using a Kurt Lesker E-beam evaporator. The transmittance was subsequently measured using a UV/vis spectrometer.

Results and Discussion

From observation of Figure 5, conductivity was much lower for films made from solutions sonicated for 120 minutes compared to solutions of 30 and 60 minute sonication times. These reduced conductivities agree with the theory that films made from longer nanotubes produce higher conductivities, because long sonication times can lead to nanotube fracture from mechanical fatigue.

Also from Figure 5, the films made from 1% SDS solution demonstrated lower conductivities than their 0.5% and 0.25% counterparts. This can be the result of SDS interfering with nanotube-nanotube contact.

A

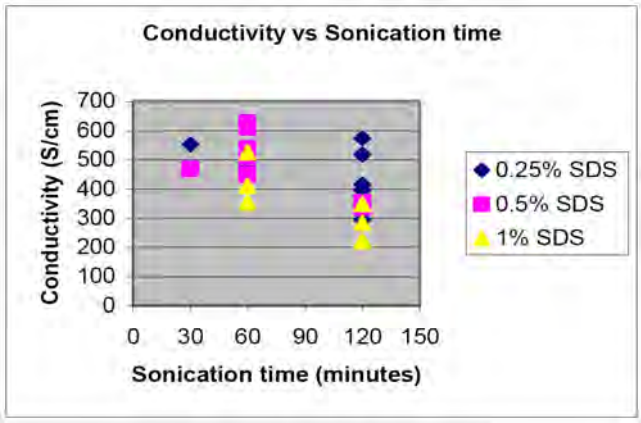

B

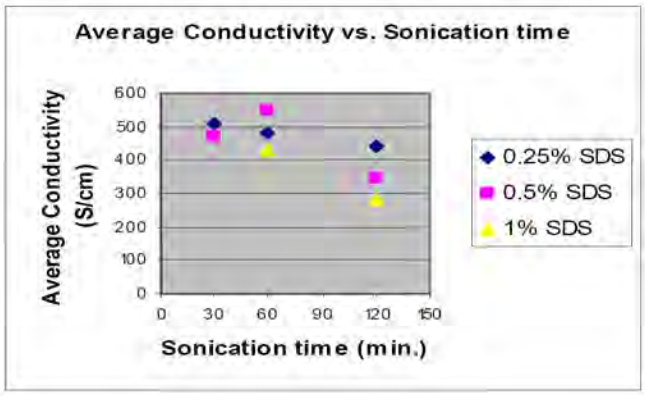

Figure 5. Graphs showing both A) conductivity of all films and B) average conductivity as a function of sonication time. Note the lower conductivities for films made from 1% SDS solution and/or 2 hours of sonication.

It must be noted that sheet resistances were much higher than expected and displayed a wide range of variability within identical data sets of SDS concentration and sonication time. In addition, the number of successful transfers varied between the data sets, so the average conductivity values found are not taken from identical numerical sets. However, the general trends noted in this report are clear.

An interesting trend that may warrant further study is the observed dependence of sonication time on the percentage of films that remain intact throughout the acetone transfer process. In this limited study, more films sonicated for 30 minutes lost adhesion to the glass slide during transfer than the other data sets. The scope of this project was too small to draw any definitive links but this may be a link worth further study in the future.

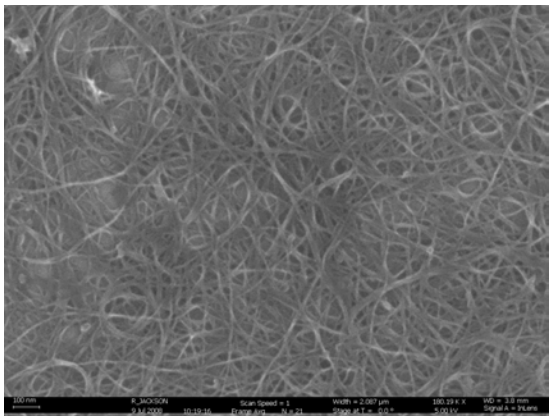

Figure 6. SEM image of a SWNT network.

Conclusion

Several trends can be seen from the data gathered. Films made with 1% SDS and/or 120 minutes of sonication time have lower conductivities than films with lower SDS concentrations and sonication times.Further investigation can be done to determine any adhesion effects due to low sonication times.

Acknowledgements

Research funded by CMDITR and the National Science Foundation No. DMR 0120967. This paper would not have been possible without help from the following people: Roderick Jackson (mentor), Dr. Samuel Graham (advisor), and the Marder Group (use of the UV/Vis spectrophotometer)

References

1. Grüner, G., J. Mater. Chem., 2006, 16, 3533-3539.
2. Dresselhaus, M. S.; Dresselhaus, G.; Avouris, P. Carbon Nanotubes. In Topics in Applied Physics;
3. Springer: Berlin, 2001. Jeroen W. G. Wilder; Liesbeth C. Venema; Andrew G. Rinzler; Richard E. Smalley; Cees Dekker; Nature 391, 6662, 59-62 (1998)
4. David Hecht D., Hu L., and Grüner G. Appl. Phys. Lett. 89, 133112 (2006)

JOSHUA GOMBERG is a student at Cornell University with a major in Materials Science and a minor in Mechanical Engineering.

Ambipolar Solution-Processed Organic Field-Effect Transistor with Al metal as Source/Drain Electrodes

ADRIAN GRANT, Tuskegee University
Xiao-Hong Zhang, Bernard Kippelen, Xuan Zhang, Seth Marder, Georgia Institute of Technology

Introduction

The transistor played an integral role in the technological development of the world in the past 70 years. It is essentially the basis of most modern switching and amplifying electronic applications. This makes up a major part of technology, therefore finding a less expensive, easier process to fabricate and also other applications is of profound interest to scientists and engineers.

The transistor currently used in today's technology, the inorganic Field effect transistors (FET) can either be manufactured as either a *p*-bulk (*n*-type/channel) or an *n*-bulk (*p*-type/channel) device. In Organic electronics it is possible to manufacture a FET that exhibits both *p*- and *n*-channel characteristics, termed an ambipolar OFET. This phenomenon was first discovered thirty years ago by Nuedeck and Malhotra in hydrogenated amorphous silicon thin film transistors (TFT).[1]

The performance and characterization of organic field-effect transistor (OFET) is currently a burning focus in research worldwide. Organic semiconductors (OSC) devices such as OFETs, OLEDs, etc. with more optimization and characterization, in the future could replace amorphous silicon technology in low-cost, large-area, flexible displays or sensors.[2] The ambipolar OFET may also have applications in complimentary oxide semiconductor (CMOS) inverter circuits. Instead of using two OFETs with different organic semiconductors, a single OFET with a common semiconductor material on the same substrate can be modified with both an *n*- and *p*-channel transistor alongside each other.[4] This will in effect reduce the complexity of fabrication of present transistor complimentary metal oxide semiconductor (CMOS) designed circuits.

Two companies, Polymer Vision and Plastic Logic interested in the commercialization of the technology, has announced their concern in flexible displays made of OSC materials for 2008.[3]

Ambipolar OFETs made of different semiconductor material as well are being researched to emit light (Light Emitting OFET (LETs)). LETs may have possible applications in display, lighting and communication system.[4]

Currently there are four known methods to develop an ambipolar OFETs, using two different metals as source and drain electrodes,[5] using a polymer blend as the active layer,[6,7,8,9] the use of two layers a *n*- and a *p*-type layer in a the OFET,[10] and the use of a single component as the active layer for the OFET. [4] The method that was used in this research is a single component ambipolar OFET made from an organic semiconductor which was synthesized to exhibit both *n*- and *p*- channel characteristics. Single component ambipolar OFETs that has the organic semiconductor vacuum deposited on the substrate have reported relatively high mobilities of 0.5 and 0.2 $cm^2 V^{-1} s^{-1}$ for hole and electrons respectively.[11,12] In contrast the single component ambipolar OFET that is solution processed has been reported to have electron and hole mobilities of 5×10^{-3} $cm^2 V^{-1} s^{-1}$,[11,13] a value that is in the order of two magnitudes lower than devices made from vacuum deposition. While vacuum depositions techniques produces higher mobilities it is more tedious and expensive than just spin coating on a polymer unto a substrate, for this reason there is much interest in solution processing ambipolar OFETs.

This research seeks to characterize and optimize an ambipolar solution-processed OFET with AL metal as source/drain electrodes.

Experimental/Computational Method

As seen in Figure 1. The top contact OFETs were prepared on heavily *n*-doped silicon (n^+-Si) substrates with 200-nm-thick thermally grown SiO_2 as gate dielectric ($\varepsilon_r = 3.9$). 50 nm of Au and 5 nm of Ti was deposited (using an e-beam system) on the back of the n^+-Si substrate as a layer to create a better contact of the gate electrode (n^+ doped Si) of the OFET. Ti is used as an adhesion layer for the gold onto to the Si-substrate. The SiO_2 layer was then treated with either a self-assembled monolayer (SAM) of octadecyltrichlorosilane (OTS) or a thin buffer layer of Benzocyclobutene (BCB). For clarity OFETs treated with OTS and BCB will be referred to as Q1 and Q2 respectively. OTS SAM with a long alkyl chain, revered as a good quality tunnel barrier to silanol groups on SiO_2 surface,[14] was formed by soaking the substrates in a 5 mM toluene solution of OTS for 15 h in a dry N_2-filled glovebox right after the substrates were oxygen-plasma treated for 2 min. The use of an OTS SAM also allows better control over the microcrystalline structure of the OSC.[15] While the thin films from diluted Cyclotene™ BCB were cross-linked at 250 °C on a hot plate for 1 h in a N_2-filled glovebox. The capacitance density C_{ox} (nF/cm^2) was measured from parallel-plate capacitors with 12 varying contact areas. The buffer layer on SiO_2 reduced C_{ox} from 16.6 to 16.2 nF/cm^2 with OTS, and 15.5 nF/cm^2 with BCB.

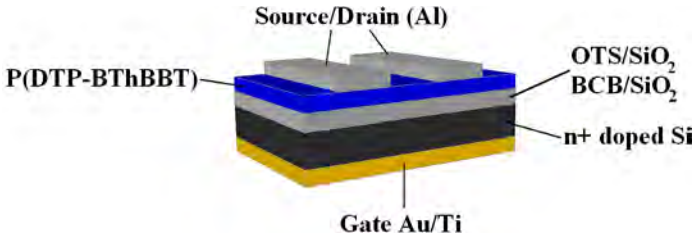

Figure 1. Diagram of the device structure of top contact OFET.

The OSC layer was then spin-coated on the treated SiO_2 (Q1: OTS, Q2: BCB) at 500 rpm for 60 s in a N_2-filled glovebox from a solution of 10 mg/ml in chlorobenze. The devices were then completed with a 100 nm-thick Al source and drain electrodes deposited through a shadow mask using a Spectros Physical Vapor Deposition (PVD) system. The samples were then transferred in a sealed vacuum container, to a N_2-filled glovebox (O_2, H_2O<0.1 ppm) at normal pressure (1 atm) for electrical analysis. The electrical measurements were performed using an Agilent E5272A source/monitor unit. After measurements were made on samples as fabricated, the samples were annealed at 110 °C and 150 °C for 30 minutes and electrically re-measured. Q1 and Q2 transistors underwent the same processing and electrical analysis.

Results

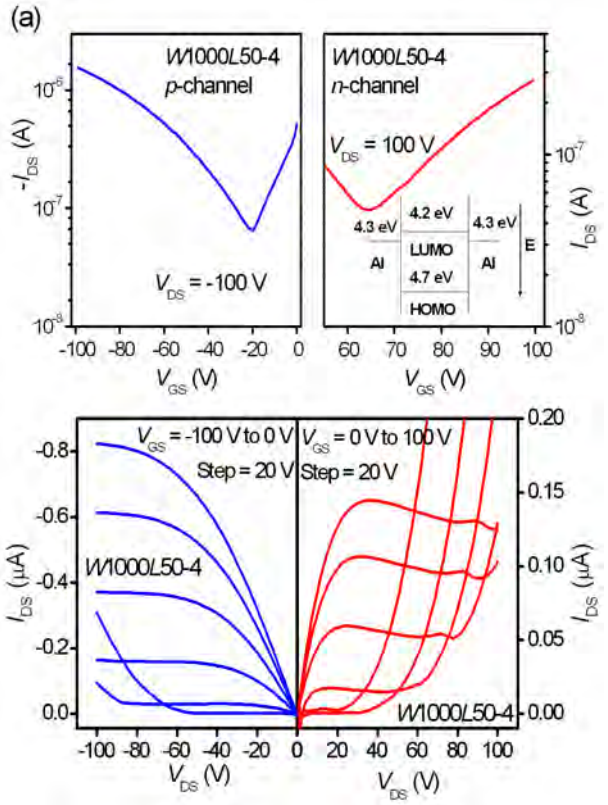

Figure 2. a) *n*- and *p*-type transfer and b) *n*- and *p*-type Output characteristics of top contact OFET Q1. The best *p*-channel and *n*-channel response were achieved when the device was annealed at 110 °C for 30 min and 150 °C for 30 min, respectively. (Inset is the simplified energy diagram, showing the LUMO and HUMO levels of the OSC and the work function of Al)

		Thermal Treatment	μ, (cm^2/Vs)	V_T, (V)
Q1	*n*-channel	150°C for 30min	5.8×10^{-4}	46.4
	p-channel	110°C for 30min	1.2×10^{-3}	-7.7
Q2	*n*-channel	Pristine	9.2×10^{-5}	10.1
	p-channel	110°C for 30min	3.7×10^{-5}	-12.3

Table 1. Electrical parameters of the solution-processed OFET with different device configurations. μ: carrier mobility, V_T: threshold voltage. C_{ox}: capacitance density of SiO_2 (16.2 nF/cm^2)

OFETs were operated in the accumulation mode and characterized in the saturation. To analyze the effect of different dielectric surface treatment (OTS/BCB) on the *n*- and *p*- channel charge transport, both transistor Q1 (with a channel length L = 50 μm and a channel width W = 1000 μm) and transistor Q2 (with a channel length L = 50 μm and channel width W = 2000 μm) were tested for the ambipolr charge transport. The two types of OFETs are only different in the dielectric surface treatment. Figure 2 shows the transfer (Drain-source current ± I_{DS} against gate-source voltage ± V_{GS} was plotted for both *n*- and *p*- channel) and output (± I_{DS} against drain-source voltage V_{DS} for increasing values of ± V_{GS} was plotted for both *n*- and *p*-channel) characteristics of the transistor Q1. The transfer and output characteristics of the transistor Q2 is shown in Figure 3.

Electron, hole mobilities and threshold voltage were determined using the square law model from metal-oxide-silicon field-effect transistor (MOSFET) as shown in Equation 1:

$$I_{DS} = \mu C_{OX} \frac{W}{L}(V_{GS} - V_T)^2 \qquad (1)$$

where μ is the field effect mobility, C_{OX} is the capacitance density of the gate dielectric, W is the channel width and L is the channel length V_T is the threshold voltage.

Both transistors show improvement in electrical characteristics after annealing at 110 °C and 150 °C.

The best *n*- and *p*- channel mobility of 5.8×10^{-4} and 1.2×10^{-3} cm^2/Vs was obtained for transistor Q1. While for transistor Q2, mobilities of 9.2×10^{-5} and 3.7×10^{-5} cm^2/ Vs were obtained for *n*- and *p*- channel transport, respectively. The threshold voltage for *n*- and *p*- channel transport of Q1 was 46.4 V and -7.7 V, respectively. While for Q2 threshold voltages of 10.1 V and -12.3 V for *n*- and *p*-channel respectively were achieved.

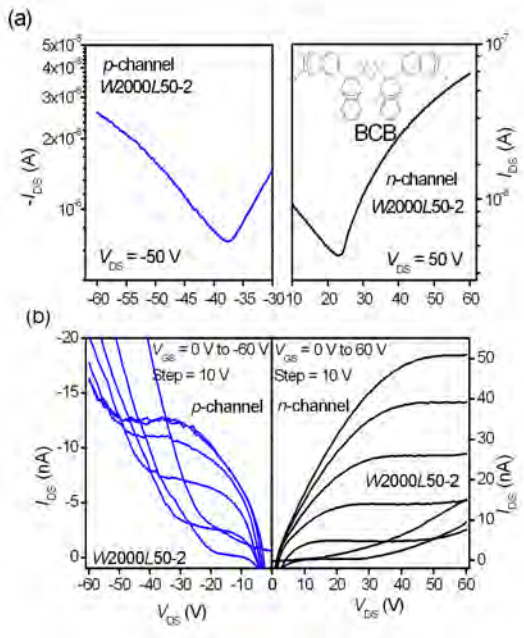

Figure 3. a) *n*- and *p*-type transfer and b) *n*- and *p*-type Output characteristics of top contact OFET Q2. The best *p*-channel and *n*-channel response were achieved when the device was annealed at 110 °C for 30 min and 150 °C for 30 min, respectively. (Inset is the diagram of the chemical structure of the BCB layer)

Discussion

The semiconductor exhibits ambipolar characteristics because Al, source and drain electrode which has a work function of 4.3 eV that is between the lowest unoccupied molecular orbital (LUMO) of the OSC) (4.2 eV) and the highest occupied molecular orbital (HOMO) (4.7 eV). The linearity of I_{DS} at low values of V_{GS} as seen in all the output characteristics, (Figure 2b and 3b) indicates that Al forms an ohmic contact with the organic semiconductor for both electron and hole transport. Transistor Q1 show a much better *p*-channel electric performance than that of *p*-channel, as shown in Table 1. The saturation current for the *p*-channel (- 0.82 μA) is over five times greater than that of the *n*-channel (0.14 μA). There was a low threshold voltage (-7.7 V) for the *p*-channel, while the *n*-channel threshold voltage was rather high (46.4 V). The high threshold voltage for *n*-channel transport can be attributed to the electron trapping by the hydroxyl groupresidues at the interface since the OTS SAM can not fully passivate the SiO_2 surface.[13, 16]

Therefore, the high *n*-channel threshold voltage of 46.4 V was greatly reduced to 10.1 V when a thin layer of BCB (Q2) instead of OTS (Q1) was used at the interface between the semiconductor and SiO_2, as shown in Figure 3 and Table 1. At the same time the *p*-channel threshold voltage (-12.3 V) was around the same as that of Q1 (-7.7 V). Consequently, transistor Q2 shows better *n*-channel performance than that of *p*-channel with a saturation current (51.0 nA) four times greater than that of the *n*-channel (-12.7 nA). However, both *n*- and *p*- channel mobilities in Q2 were lower than that of Q1. This may have been due to the thinness of the organic layer, and the spun film on the BCB tends to be very thin since the BCB surface has a high hydrophobicity. To spin films from a higher concentration may solve the problem.

Conclusion

Fabricated OFETs have demonstrated a typical ambipolar behavior with two different dielectric surfaces. The OTS treated dielectric (SiO_2) transistor (Q1) has shown better *p*-channel characteristics than *n*-channel and for the BCB treated dielectric transistor (Q2) the performance was reversed giving a better *n*- than *p*- channel, with less saturation current with the difference being in the magnitude of about 1600%. The semiconductor layer on the BCB treated dielectric was too thin and so mixed results were achieved (a decrease in threshold voltage and also reduced mobility). Possibly if the semiconductor layer was thicker the mobility results could be comparable to that of the SAM OTS layer.

Future work will be geared towards film morphology changes upon annealing, studying the dependence of mobility on the film thickness, emphasizing the *p*-channel electrical characteristics with Au as source/drain electrodes, and emphasizing the *n*-channel electrical characteristics with Ca as source/drain electrodes.

Acknowledgements

I would like to thank the National Science Foundation, Georgia Institute of Technology, the Kippelen group, the co-coordinators of the REU program and the REU students, for a great summer experience.

References

1. Lindner Th, G. Paasch, and S. Scheinert, "Operation and properties of ambipolar organic heterostructure field-effect transistors," Journal of Applied Physics 101 (1), 014502 (2007).
2. Ming L. Tang, Anna D. Reichardt, Nobuyuki Miyaki et al., "Ambipolar, High Performance, Acene-Based Organic Thin Film Transistors," J. Am. Chem. Soc. 130 (19), 6064-6065 (2008).
3. a) http://www.polymervision.com (accessed April 2008). b) http://www.plasticlogic.com (accessed April 2008)
4. S. Setayesh E. Smits M. Cölle E. Cantatore B. de Boer P. W M Blom D. M de Leeuw T. D. Anthopoulos, "Air-Stable Complementary-like Circuits Based on Organic Ambipolar Transistors," Advanced Materials 18 (14), 1900-1904 (2006).
5. Rost Constance, J. Gundlach David, Karg Siegfried et al., "Ambipolar organic field-effect transistor based on an organic heterostructure," Journal of Applied Physics 95 (10), 5782-5787 (2004).
6. E. J. Meijer, D. M. de Leeuw, S. Setayesh et al., "Solution-processed ambipolar organic field-effect transistors and inverters," Nat Mater 2 (10), 678-682 (2003).
7. Y. Hayashi, H. Kanamori, I. Yamada et al., "Facile fabrication method for p/n-type and ambipolar transport polyphenylenevinylene-based thin-film field-effect transistors by blending C[sub 60] fullerene," Applied Physics Letters 86 (5), 052104 (2005).
8. K. Tada, H. Harada, and K. Yoshino, "Field-Effect Mobility of Molecularly Doped Poly(3-hexylthiophene)" Jpn. J. Appl. Phys. 36 (1997) pp. L718-L720
9. J. D Wind S. A Jenekhe A. Babel, "Ambipolar Charge Transport in Air-Stable Polymer Blend Thin-Film Transistors," Advanced Functional Materials 14 (9), 891-898 (2004).
10. Cho Shinuk, Yuen Jonathan, Kim Jin Young et al., "Ambipolar organic field-effect transistors fabricated using a composite of semiconducting polymer and soluble fullerene," Applied Physics Letters 89 (15), 153505 (2006).
11. J. Zaumseil and H. Sirringhaus, "Electron and Ambipolar Transport in Organic Field-Effect Transistors," Chem. Rev. 107 (4), 1296-1323 (2007).
12. F. Meghdadi S. Günes N. Marjanovic G. Horowitz P. Lang S. Bauer N. S Sariciftci Th. B. Singh, "High-Performance Ambipolar Pentacene Organic Field-Effect Transistors on Poly(vinyl alcohol) Organic Gate Dielectric," Advanced Materials 17 (19), 2315-2320 (2005).
13. Lay-Lay Chua Jana Zaumseil Jui-Fen Chang Eric C.-W. Ou Peter K.-H. Ho Henning Sirringhaus & Richard H. Friend, "General observation of *n*-type field-effect behaviour in organic semiconductors" Nature 434, 194 - 199 (2005).
14. X. H. Zhang, B. Domercq, and B. Kippelen, "High-performance and electrically stable C[sub 60] organic field-effect transistors," Applied Physics Letters 91 (9), 092114 (2007).
15. X.-H. Zhang, B. Domercq, X. Wang, S. Yoo, T. Kondo, Z. L. Wang, B. Kippelen, "High-performance pentacene field-effect transistors using Al2O3 gate dielectrics prepared by atomic layer deposition (ALD)". Dir. Organ. Elec. 8 (2007) 718-726.
16. David L. Angst and Gary W. Simmons, "Moisture absorption characteristics of organosiloxane self-assembled monolayers," Langmuir 7 (10), 2236-2242 (1991).

ADRIAN GRANT hopes to finish his bachelors in Electrical Engineering and go on to get a masters and a PhD. after which he will work in the industry for a while and then start his own business.

Piezo-Electric Laser Control for Ultra-Cold Atom Manipulation

KEVIN T. GUDENKAUF, University of Arizona
Carlo Samson, Tyler Neely, Dr. Brian Anderson, University of Arizona

Introduction

The purpose of this research project was to design and create a system that will allow the movement of a pair of low power laser beams to be controlled, so that the lasers can be focused onto a Bose-Einstein condensate, or BEC, and scanned across it, producing vortices. This project included both the designing and building of a circuit to control both axes of motion, of both beams, as well as determining the optical setup required to focus the beams onto the Bose-Einstein condensate.

Results and Discussion

This summer's research produced a system consisting of a control circuit and an optical system that, together, allow a pair of low power laser beams to be successfully scanned across a BEC using either a single input, or separate inputs for each of the four axes involved.

Figure 1. The finalized control circuit in its housing.

The circuit amplifies a 5 volt (max.) input signal to the 60 volt (max.) signal that is required to get sufficient displacement from the piezo-electric disks. The circuit also allows for an offset of up to 60 volts to be added to the output going to each axis; this, combined with input amplitude adjusting potentiometers, and a switch that allows the user to invert the input signal (so that it is a 0 to -5 volt signal) allows the displacement of both beams to be fully adjustable in angle. The optical set-up includes the use of a Mach-Zender interferometer to allow for only one laser to be used, and the piezo disks are placed in the mounts of the interferometer's mirrors.

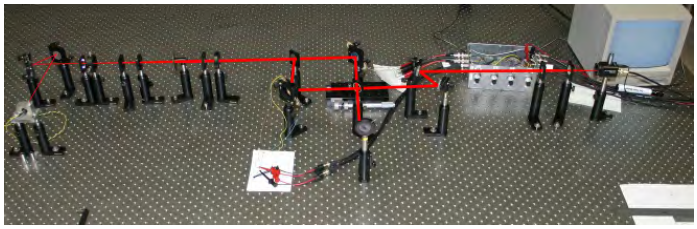

Figure 2. The optical set-up, where the beam originates from the left, moves through the interferometer, whose mirrors contain the piezo disks connected to the control circuit, and is finally focused down to a small point after recombining at the end of the interferometer.

This laser control system worked as intended, and produced a displacement of 120-150 microns, with a beam diameter of 10-28 microns, which was deemed sufficient for use in future experiments.

Conclusion

The final control system is successful in completing all that was needed of it, and the beam displacements produced will be helpful in various future experiments to further our scientific knowledge of how BECs form, and how vortices form and interact with each other.

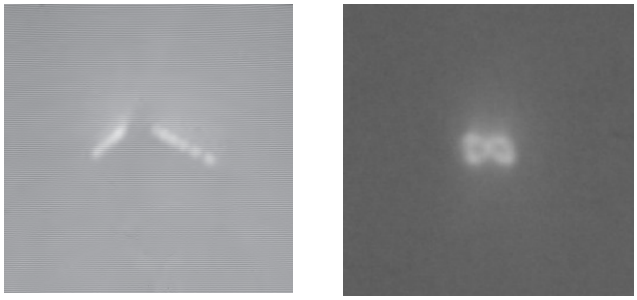

Figure 3. Images of the beam moving with: a single 0-5V input (left), and two separate sinusoidal inputs using function generators (right).

Acknowledgments

Funds for this research were provided by the Center on Materials and Devices for Information Technology Research (CMDITR), and the NSF Science and Technology Center No. DMR 0120967. I would also like to thank Dr. Brian Anderson, who allowed me to participate in his lab, as well as Carlo Samson and Tyler Neely for their help and guidance.

KEVIN T. GUDENKAUF is a student at the University of Arizona, and is currently earning a degree in physics. He will be applying to Graduate school in 2010.

Novel Mixed-Crystal System for Studying Single Molecule Photophysics

ELIZABETH JIMENEZ, California State University, Stanislaus
Eric D. Bott, Erin A. Riley, University of Washington

Introduction

The Reid lab is interested in understanding single-molecule (SM) photo-physics in various salt crystal hosts. Previously studied crystal systems have been largely inert and static. To further probe single-molecule (SM) behavior, we will begin new research on a crystal host with dynamic properties. This new host system, triglycine sulfate (TGS), is both ferroelectric and piezoelectric, allowing us to perturb the SM environments in situ by a number of possible methods. This will provide greater insight into the host's involvement in the photo-physical processes responsible for the unique optical phenomena observed in SM systems.

Previous work has focused on studying the intermittent fluorescence of SMs. Known as blinking, it is manifested as time-dependent switching between discreet intensity states by a molecule under continuous irradiation. Analysis of these traces yields insight into the fundamental processes responsible for this behavior. We wish to collect and analyze blinking traces from SM in TGS crystals and attempt to correlate blinking statistics perturbations from our dynamic crystal host.

As TGS is a new host system, we must first understand the macroscopic-level properties before delving into SM-level analysis. Heavily dyed crystals of TGS doped with pyranine (**a**) and pyranine tetrasulfonate (**b**) as shown in Figure 1 were successfully grown seen in Figure 2, and their optical properties investigated. These measurements lend greater insight into the guest-host interaction in TGS, opening the doors for SM studies.

Methods

TGS crystals were grown by controlled evaporation of a supersaturated TGS solution (300g/L) in the presence of **a** and **b** at both heavily doped (10^{-3} M) and dilute (10^{-8} M) concentrations suitable for SM studies.

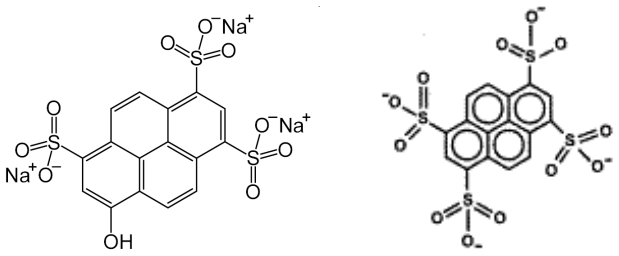

a) Pyranine **b**) Pyranine tetrasulfonate

Figure 1: Molecular structure of both dyes used.

Seed crystals less than 1 mm in the longest dimension nucleated after one day of growth. Seeds were harvested and placed in dishes containing a warm growth solution consisting of the seed growth solution with failed seeds re-dissolved. Crystals ~ 2cm point to point were harvested 2-3 days later using a total of 20-30 ml growth solution.

Absorbance spectroscopy was used to determine the dye content of the crystal, and inclusion ratio (mol dye/ mol TGS). A calibration curve of concentration vs. absorbance for dye solutions of **b** was collected, from this plot the molar absorptivity at 376 nm was determined to be 45000 L/cm•mol. Using this, the concentration of a solution of re-dissolved crystal was determined, and the moles of dye in the crystal were calculated. The inclusion ratio was determined to be 3.3 x 10^{-4} mol dye/mol TGS, as compared to the growth solution concentration of 1 x 10^{-5} mol dye/ mol TGS. This indicates that there is a driving force for the dye to incorporate into the crystal

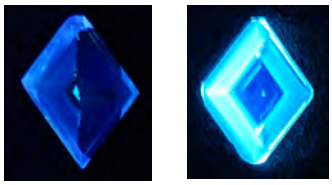

a) b)

Figure 2: Dark field fluorescence of dyed TGS.

Dark field images of the crystals are shown in Figure 2. From these images it is evident that the dye only incorporates into certain sectors of the crystal, demonstrating chemical specificity in the dye incorporation mechanism.

To further investigate the host/guest interaction, polarized absorption and fluorescence measurements were conducted. Using a polarizing microscope, the optical axes of the crystal were identified, and the crystal's habit was characterized as shown in Figure 3. Polarized absorption spectra were obtained by placing a polarizer in the incident light path of the spectrometer and rotating it in alignment with the two optical axes. Due to low dye concentrations, this data could not be analyzed; instead, polarized emission measurements were used, a much more sensitive technique at low concentrations. These measurements were taken similarly by placing polarization optics in front of the detector of the fluorimeter. From the ratio of intensities of the two polarizations the bulk alignment is calculated as follows:

$$\theta = \arctan\left(\frac{I_{\parallel}}{I_{\perp}}\right)$$

The bulk alignment with respect to the long axis was found to be 84°. This preferential alignment will be further investigated at the SM level, as previous studies have shown a wide distribution of molecular orientations may exist.

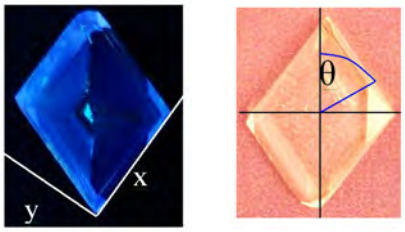

Figure 3: Ferroelectric Z direction (x,z,y) (a,b,c) normal to axes indicated in dark field fluorescence. The average alignment of molecules is also shown in reference to optical axes.

Fluorescence spectra of TGS dyed crystals and growth solution were acquired as well as fluorescence lifetimes to understand their comparative statistics (Figure 4). The fluorescence spectra of the crystal are slightly red shifted from the solution spectra, as well as the relative intensities of the features. The crystal for example, has a much stronger emission peak at about 500 nm than the solution. This indicates that the dye is experiencing different interactions with the crystal solvent than in solution which is crucial to know for SM studies.

Fluorescence lifetimes were measured for b in various environments using a Time-Correlated Single Photon Counting (TCSPC) system (Fluorotime, Pico Quant). Results are shown in Figure 5.

Large differences in the lifetimes were observed from crystal to solution. The solution spectra were especially interesting, showing drastic variations in lifetimes, as well as deviations from single exponential behavior. Whether this was due to the dye interaction with TGS or with itself was investigated briefly by doing concentration studies on both. It was found that dye concentration was the only factor that contributes to variations in lifetime and deviations from single-exponential behavior. Possible explanations include dye-dimerization; however a rigorous study needs to be performed to eliminate any possibility that this is an artifact of instrument set up. The macroscopic lifetime of the dye in crystal will be compared to SM TCSPC measurements in the future.

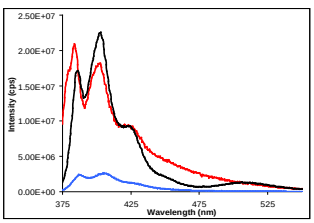

Fluorescence emission spectra of TGS dyed with **b**, $\lambda_{excitation}$ = 375 nm

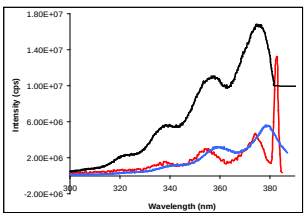

Fluorescence excitation spectra of TGS dyed with **b**, $\lambda_{emission}$ = 403 nm

Figure 4: Fluorescence intensity vs. wavelength for pyranine dye in various media; in solution (red), crystal (longest dimension), and crystal (short dimension). Similar trends are evident in the fluorescence spectra for both emission (left) and excitation (right). Evidence shows a slight red-shift in intensity wavelength peak for excitation wavelength.

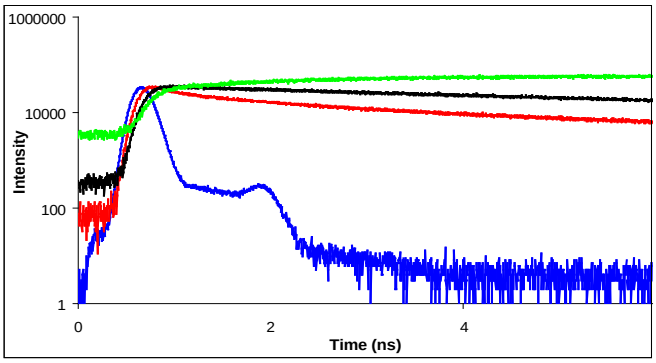

Figure 5: Fluorescence lifetimes depicted for **b** in various concentrations of dye. Shown in semi-log plot, solution in red (10^{-3} M), crystal in black (10^{-5} M), in SM concentration (10^{-8} M). IRF is also shown in blue. Lifetimes determined to be 11.75 ns, 7.65 ns and 3.85 ns, respectively.

Future Work

TGS crystals were grown from low concentrations of dyes suitable for SM studies. Future work will be to determine the distribution of SM orientations in TGS, and the distribution of lifetime behavior analogous to the bulk measurements presented in this work. The ferroelectric properties of dyed TGS must also be characterized in order that a driving electric field can be used to perturb the SM under investigation. These experiments will be completely novel; no other research group has access to the control that this experimental design will allow us to investigate the fascinating and confounding photophysics of SM systems. Because of its dynamic properties, the crystal system may add a degree of complexity with the ability to perturb the crystal structure. Further studies may give insight in to the perturbation expectations of single molecules in situ. Understanding the host involvement of the ferroelectric crystal systems may shine some light on photo-physical properties of single molecules isolated in crystal hosts.

Acknowledgements

I would like to thank Eric and Erin and the Reid Group in general. They have provided me with the assistance and support necessary for me to accomplish so much in such a short time. I would like to thank Marya and the STC office for their wonderful support and organization that has made this whole event possible. I would also like to thank the NSF STC-CMDITR 2008 Summer REU program for their continued support of science and academia.

References

1. Wustholz K., Bott E., Isborn C., Li X., Kahr B., Reid P. J. Phys. Chem. C 2007, 111, 9146-9156
2. Jona, Shirane. 1962. Triglycine Sulfate and Isomorphous Crystals. New York: The MacMillan Co.
3. Wustholz K., Kahr B., Reid P. J. Phys. Chem. B 2005, 109, 16357-16362
4. Wustholz K., Sluss D., Kahr B., Reid P. Inter. Rev. Phys. Chem. 2008, 27, 167-200

ELIZABETH JIMENEZ is earning her B.S. in Physics. Afterwards, she plans to look into graduate school for Physics, Physical Chemistry, or Astronomy and to further explore research in science and technology.

Studies of the Optical Properties of Self-Assembled Photonic Crystals Infiltrated with Conjugated Polymers

MENG KANG, Duke University
San-Hui Chi, Joseph Perry, Georgia Institute of Technology

Objective

The objective of this project is to infiltrate polyacetylene into microstructures of self-assembled photonic crystals (PCs) using capillary action on a monomer undergoing ring-opening metathesis polymerization (ROMP) and to determine the optical properties of these polymer infiltrated PCs.

Background

PCs are periodic structures composed of high and low refractive index domains.[1] PCs possess photonic band gaps (PBGs) that can affect the propagation of electromagnetic waves with wavelengths located at the PBG.[2] Methods of PC fabrication include 3D lithography and self-assembly.[3] With each method, the location of the PBG, or the wavelength of maximum reflectance, can be manipulated by varying the size and refractive indices of each component and their periodic structures.[4] This study focused on engineering the PBG locations of self-assembled synthesized PCs via infiltration of conjugated polymers, enabling the alteration of the effective refractive index and the resulting optical properties of PCs.

To fabricate a self-assembled PC, or so-called synthetic opal, microspheres of selected materials with uniform size distribution (deviation < 10%) were used. The PBG location of a self-assembled PC can be estimated using the equation[5]

$$\lambda_{\max} = \left(\frac{8}{3}\right)^{1/2} D\left(n_{sphere}^2 V_{sphere} + n_{void}^2 V_{void} - \sin^2\phi\right)^{1/2}, \quad (1)$$

where D is the diameter of the structural spheres, n is the refractive index of the sphere or the void, V is the volume fraction of the sphere or void, and Φ is the light incident angle. As detailed in Equation 1, the size of spheres, the refractive indices of sphere and void, and the volume fractions of spheres and void are the main variables that affect the PBG position, λ_{max}. Among these factors, the effective refractive index,

$$n_{eff} = (n_{sphere}^2 V_{sphere} + n_{void}^2 V_{void})^{1/2} \quad (2)$$

plays a crucial role in PBG and reflectivity of a PC, as well as the spectral width of the reflection peak,[6]

$$R = \left(\frac{n_i - n_{eff}}{n_i + n_{eff}}\right)^2 \text{ and } \Delta\lambda \propto \left(n_{eff} L\right)^{-1}, \quad (3)$$

where R is the reflectivity of a PC, n_i is the refractive index of the medium from where light is incident into a PC, $\Delta\lambda$ is the minimum resolvable bandwidth of the reflected wavelength, and L is the thickness of a PC. From Equations 1-3, it can be seen that adjusting the PC effective index results in variations in the reflected wavelength, the corresponding reflectivity of the PC, as well as the spectral width of the reflection peak.

To engineer the reflected wavelength and the related optical properties of a PC, it is necessary to manipulate the refractive indices of both structural components. One approach is to infiltrate the PC void with a selected material that possesses a refractive index higher than that air, which has a refractive index of 1.0. Infiltrating voids with other high-index material results in a higher n_{eff} and an overall longer λ_{max}. With a higher n_{eff}, the PC would possess increased R and reduced $\Delta\lambda$, resulting in higher spectral resolution and efficiency. Furthermore, successful infiltration of void space with selected materials would enable advanced PC designs and, subsequently, broader applications. For example, the infiltration of materials with large optical nonlinearities could potentially produce intensity-tunable PCs.

Due to their unique characteristics, polymers have been a popular choice for infiltrating PCs.[7] However, current research has reached a bottleneck of low infiltration ratio due to the low solubility and the thermal stability of polymers in PCs.[7] In order to achieve a higher infiltration ratio, one possible approach is *in situ* polymerization. This proposed scheme was based on the idea of epoxy inversed opal, where the opal is immersed in a viscous fluid of epoxy resin, followed by the polymerization of epoxy resin. With less than 5% shrinkage of the volume between liquid and solid, a very high percentage of polymer infiltration efficiency was achieved.[7] In analogy to the polymerization of epoxy from liquid resin, certain conjugated polymers such as polyacetylene can be synthesized from liquid monomer via ROMP (see Scheme 1).[8] A liquid monomer (e.g. mono-substituted cyclooctatetraene, R-COT) allows initial infiltration of the void space with the monomer, followed by ROMP within the PC structure. R-COT can be polymerized into long-chain substituted polyacetyelenes with various metathesis initiators such as the second-generation Grubbs' initiator (see Scheme 1). This initiator for the polymerization process is known for its mild reactivity and air-stable properties.[8] The synthesized substituted polyacetylenes have a high refractive index of around 2.2 in the telecommunications spectral regions.[8] Filling a PC with such a high-index material would increase the n_{eff}, resulting in enhanced R and reduced $\Delta\lambda$. In addition, polyacetylene also exhibits large third-order optical nonlinearities.[8] Thus, the prospective of polyacetylene-infiltrated microstructures enabling control of light propagation becomes possible.

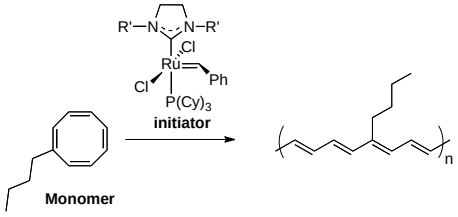

Scheme 1. ROMP of *n*-butyl-COT (as monomer) with second-generation Grubbs' initiator.

This study presents the current progress on self-assembled PC synthesis, infiltration of substituted polyacetylenes via ***in situ*** polymerization, as well as the polyacetylene infiltrated PCs' resulting linear optical properties.

Methods

Two types of microspheres, made from the hydrophilic silica (n=1.37) and the hydrophobic polystyrene (n=1.59), were used to synthesize self-assembled PCs. The influence of the different microspheres' physical properties (e.g. hydrophilicity, density, and size) on the growth of PCs, the infiltration of conjugated polymers, and the result.

1. Preparation

Substrates, 1 inch x 0.5 inch glass slides, for growing the silica- and polystyrene-based synthetic opal films are cleaned thoroughly with piranha solution (concentrated H_2SO_4 : 30% H_2O_2 = 3 : 1). Slides were submerged in piranha solution ing optical properties are examined. for approximately 4 hours, then rinsed with de-ionized water and sonicated for 5 minutes repeatedly until the pH of glass surface was neutral. The slides were then rinsed with methanol and baked in the oven at 120 °C.

Microspheres of silica and polystyrene were used as received. Solutions of silica and polystyrene beads with various diameters (400nm and 700nm for silica and 300nm for polystyrene) were prepared. Six different concentrations ranging from 0.001% to 1% were obtained by diluting the parent solutions with de-ionized water.

2. Fabrication of self-assembled PCs

Two opal growth methods were tested in this study. The first method utilized capillary action to pull microspheres into thickness-controlled cells, while the second method involved controlled sedimentation of microspheres on the surfaces of substrates. Both growth methods were used to determine the superior growth method.

With the capillary-action method, two clean glass slides spaced by a 25µm Teflon spacer were clamped together to form a capillary cell. Capillary cells were stood vertically in 3.5mL of microsphere solution in 5mL plastic beakers. For the sedimentation method, one single clean glass slide was stood at an angle of approximately 60° from the ground in a 3mL plastic beaker containing 2.5mL of microsphere solution. For both methods, beakers were covered by crystallizing dishes to reduce the fluctuation of solution evaporation rate throughout the film growth period. For each experimental condition, two samples were prepared.

3. Synthesis of monomer and polymer

Under the flow of nitrogen, a 1-liter RBF was charged with 500mL of anhydrous diethyl ether and 19.2 grams of distilled COT. The reaction mixture was allowed to cool down to 0 °C in an ice bath. Slowly, 147mL of *n*-butyl lithium (2.5M in hexane) was added over the period of 30 minutes under the nitrogen counter-flow. The mixture was then stirred at room temperature for an additional hour. At room temperature, oxygen was bubbled through the reaction mixture for 2 hours until the formation of an orange solid was observed. When oxidation was complete, the reaction mixture was treated with 42.6mL of 1M $HCl_{(aq)}$ in an ice bath. The mixture was extracted with pentane, and the orange organic layer was dried over anhydrous $MgSO_4$. The solvent was then removed under reduced pressure. The product (*n*-butyl-COT) was characterized by NMR and the purity was verified as 99% by GC-MS. The product, *n*-butyl-COT, was transferred into an argon-filled glove box and run through columns of neutral aluminum oxide (Al_2O_3), which had been baked at 150 °C, to remove moisture and remaining inorganic impurities prior to polymerization. Purified *n*-butyl-COT was stored under 20 °C.

4. Infiltration of substituted polyacetylenes into PCs via *in situ* polymerization

Two approaches to achieve polyacetylene infiltration via *in situ* polymerization were investigated. The monomer-to-initiator equivalent ratio for the *in situ* polymerization was ~450 : 1. The first method involved the pre-mixing of 100µL liquid *n*-butyl-COT with 100µL initiator solution (~0.01M, in spectral grade dichloromethane, DCM). While low-weight molecules dominated and the solution mixture was still fluid, the mixture was infiltrated into the PC by capillary action force. The second method involved the pre-coating of initiator on the sphere surface. The initiator was dissolved in DCM with calculated concentrations and the initiator solution was filled into PCs by capillary force. Solvent was removed under vacuum and the liquid monomer was then infiltrated into the initiator-coated PC to begin ROMP. For this method, the issues of homogeneously distributing initiators on the surface of spheres and properly controlling the amount of monomer and initiators in the PCs had to be noted in order to reduce the gradient of concentration of reactants.

5. Characterization of polyacetylene-infiltrated PCs

The optical properties of a PC, such as the reflectance and transmittance, before and after polymer infiltration were determined using an UV-Vis-Near IR spectrometer (SHIMADZU UV-3100). The microstructures of the infiltrated PCs and the infiltration ratio will be determined using a scanning electron microscope (SEM) by fracturing and coating the films with ~1nm gold particles.

Results and Discussion

Taking into consideration the bead sizes available for this study, silica beads of 400 and 700nm, and polystyrene beads of 300nm were chosen for opal film synthesis. During opal film fabrication, the issue of density was taken into consideration. Silica has a density of 2.2 g/cm^3 while polystyrene has a density of 1.05 g/cm^3. Following a comparison to the density of water (n=1.30), 1.0 g/cm^3, it was expected that polystyrene beads would show better suspension in water. Accordingly, during the ~1 month opal growth period, sedimentation of heavier silica was observed at early stage while the

most concentrated polystyrene solution still showed relatively good suspension throughout most of the growth period. The status of microsphere suspension is expected to influence the packing structures and percentage of structural defects present in the resulting opal films.

In order to gain initial insights into the relationship between optical properties, sphere sizes, and effective refractive indices, predicted PBG wavelengths of silica- and polystyrene (PS)- based PCs infiltrated with materials with various refractive indices were calculated according to Equation 1. To simplify calculations, the refractive indices at different wavelengths were assumed to be constant and the microstructures of the PCs were assumed to possess face-centered cubic (FCC) packing throughout the whole area of investigation. Also assuming normal incident light, the calculated reflection wavelengths (λ_{max}) of silica- and polystyrene-based PCs with different sphere sizes and with different void materials were calculated and are shown in Figures 1-5. When the difference in void refractive indices is ~ 0.1, e.g. comparing THF and toluene infiltrated films, it is probable that the shift in reflection peaks of the two films will be very similar. As can be seen in Figures 3 and 4, a difference of less than 30nm in reflection peak was calculated between THF and toluene infiltrated films. Depending on the quality of film growth and ratio of infiltration, the two peaks may become indistinguishable.

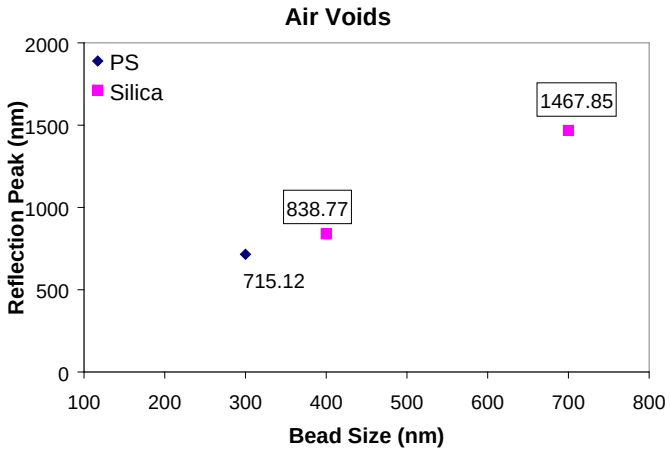

Figure 1. Calculated reflection wavelengths of PCs with air (n=1.00) filled void.

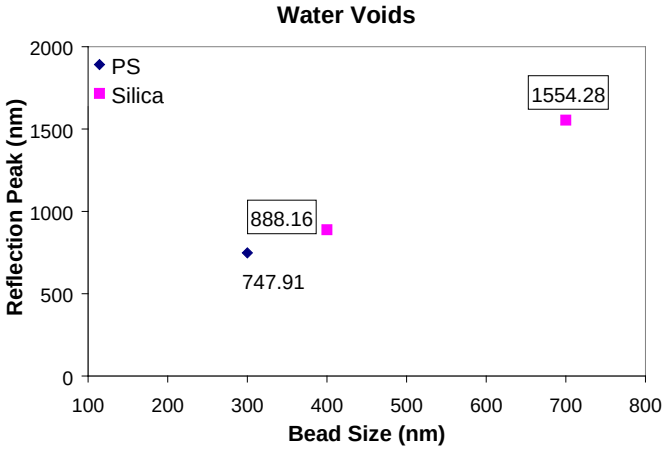

Figure 2. Calculated reflection wavelengths of PCs with water (n=1.33) filled void.

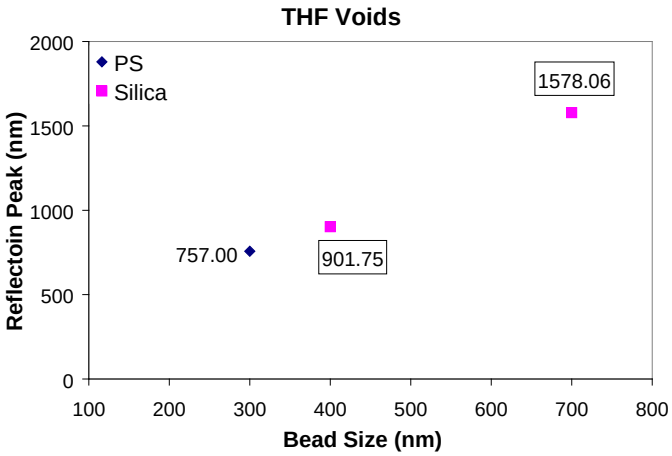

Figure 3. Calculated reflection wavelengths of PCs with tetrahydrofuran (THF) (n=1.41) filled void.

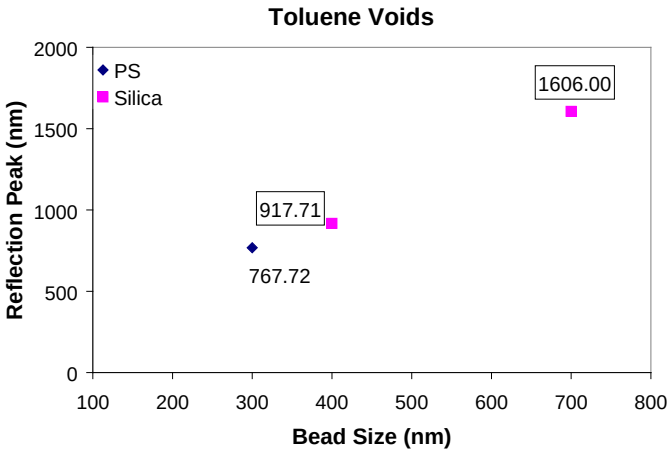

Figure 4. Calculated reflection wavelengths of PCs with toluene (n=1.5) filled void.

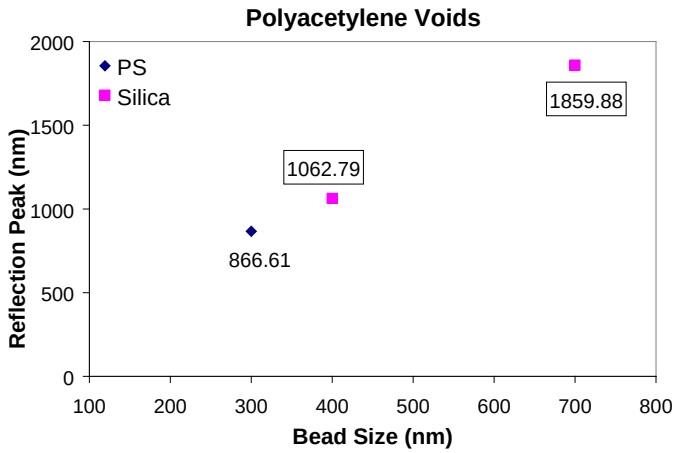

Figure 5. Calculated reflection wavelengths of PCs with polyacetylene (n ~ 2.2) filled void.

To carry out the infiltration of substituted polyacetylenes into PC void spaces, it was necessary to determine how the viscosity of the polymerizing solution affects the degree of infiltration. Based on the packing density of a FCC packing structure for 700nm diameter PC spheres, the width of the void space was calculated to be approximately 289nm. For 300nm diameter PC spheres, the

width of the void space was calculated to be approximately 125nm. Because void space of PCs is extremely miniscule, the viscosity of the polymerizing monomer and initiator mixture had to be controlled carefully. In a preliminary study, 4 pairs of piranha-cleaned slides without spacers were clipped together based on the assumption that there was still some tiny spacing between the glass slides, the tiny PC void space could thus be modeled. First, 100µl of *n*-butyl-COT was mixed with 100µl of 0.01M initiator-DCM solution to start off the ROMP. Then, after 3, 5, 7, and 9 minutes after the initiation of the ROMP, these clipped clean slides were dipped into the polymerizing solution. Both the height of the solution migrating in the clipped slides as well as the solution color in each cell after approximately 10 minutes of polymerization were observed (See Table 1). As noted in Table 1, the mixture solution still migrated to the cell top after 7 mins of polymerization. However, since the lighter colors potentially represent the low molecular weight portions of the polymerizing mixture, the relatively lighter color of the reacting mixture after 10 mins of polymerization indicated that only monomers and polymerizing low molecular weight oligomers were transferred into the cell. When high molecular weight oligomers are left out of the cell, the equivalent ratio of low to high molecular weight species in the cell was changed compared to a typically prepared film and might result in less dense polymer and lower filling ratio. From this preliminary test, it was determined that the best infiltration time of the polymerizing solution was within 3 minutes after the initiation of polymerization.

Since the growth period of opal films occurred over 1 month, several old films made in 2004 were used for initial studies of polymer infiltration and optical properties. The results are detailed below. Before infiltrating polymers into PCs, the transmission and reflection spectra of PCs were taken as references. Typical transmission and reflection spectra of silica opal films are shown in Figure 6. In this study, six films (Samples 1-6) made of 700 nm silica microspheres and 1 film (Sample 7) made of 400 nm silica microspheres were used for polymer infiltration. The reflection peaks for Samples 1-6 were at approximately 1400nm, which corresponded to the calculated value of 1467.85nm. Sample 7's reflection peak was around 780nm, which corresponded to the calculated value of 838.77nm. Differences between the calculated and measured λ_{max} could have been caused by differences and defects in packing structure of the opal films during and after growth. Ordered packing structure over a large opal film area is a factor in self-assembled PC fabrication that is difficult to control. It can be seen that most reflection peaks and transmission dips were very wide, and their values did not add up to 100%. Since the absorption of silica and polystyrene in these wavelengths was small, the loss is possibly due to scattering caused by unstructured domains in the opal films.

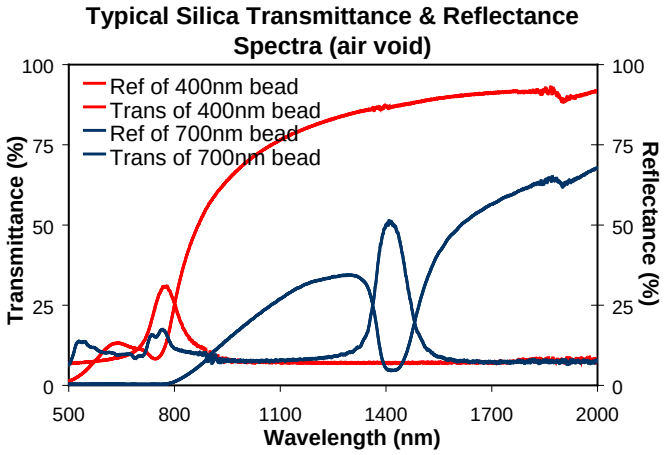

Figure 6. Typical transmission and reflection spectra of silica opal films made from 400nm and 700nm spheres with thickness of 15µm and 25 µm, respectively.

Samples 1, 2, 3, and 5 were then filled with solvents of various indices in order to observe the changes in the transmission and reflection spectra. The transmission and reflection spectra of films before infiltration, with solvent filled, and after solvent was removed are shown in Figures 7-10. The spectra taken after solvent removal indicated minimal structural alteration by the various solvents, though SEM was not performed in order to preserve the entirety of the films for infiltration with polyacetylene by capillary force soon after. Sample 1's void was infiltrated with DI water and another spectrum was taken two days after removal (see Figure 7). Sample 2 was infiltrated with toluene (see Figure 8). Sample 3 was infiltrated with THF (see Figure 9). Sample 4 broke into two pieces during testing. Polymerizing polyacetylene was dropped onto one side of Sample 4 for a test comparison. Sample 5 was infiltrated with polyacetylene by pre-mixing the monomer and initiator solutions followed by infiltration of the polymerizing mixture immediately (see Figure 10). Sample 7 was also infiltrated with polyacetylene by the pre-mixing method (see Figure 11). Samples infiltrated with substituted polyacetylene were immediately stored in an argon-filled glove box to prevent oxidization. When comparing calculated reflection peaks for the 700nm silica-infiltrated PC's to the actual reflection peaks acquired experimentally (see Figure 12), the actual reflection peak wavelengths for air, toluene, and polyacetylene were shorter than as calculated, whereas the water and THF reflection peaks were longer. The deviation were on the scales of 45-85nm with the

	3 min after	5 min after	7 min after	9 min after
Color of solution in the slide after mixing for	Mostly dark brown throughout; noticeable color gradient: color becoming lighter from top to bottom of slide	Mostly light brown on top portions and dark yellow on bottom portions of slide	Slide is very light brown at top and yellow at bottom	Only a small brown blotch at the bottom of the slide; solution did not infiltrate much at all
Height of solution penetrated into slides	Filled to top of slide	Filled to top of slide	Filled to top of slide	Very bottom of slide

Table 1. Qualitative observations of slides dipped into the ROMP reacting solution at 3, 5, 7, and 9 minutes after start of polymerization.

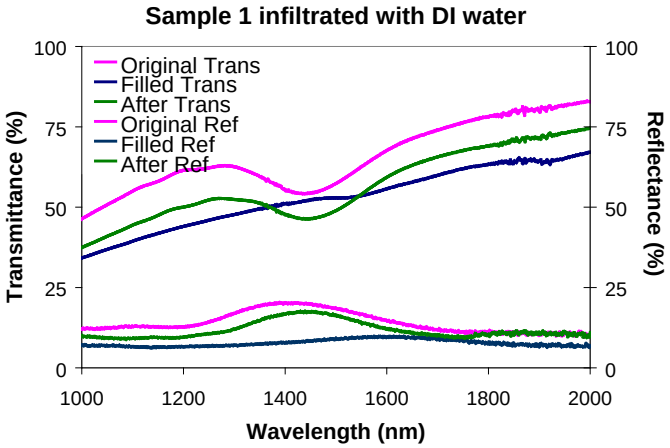

Figure 7. Transmission and reflection spectra of Sample 1 infiltrated with DI water.

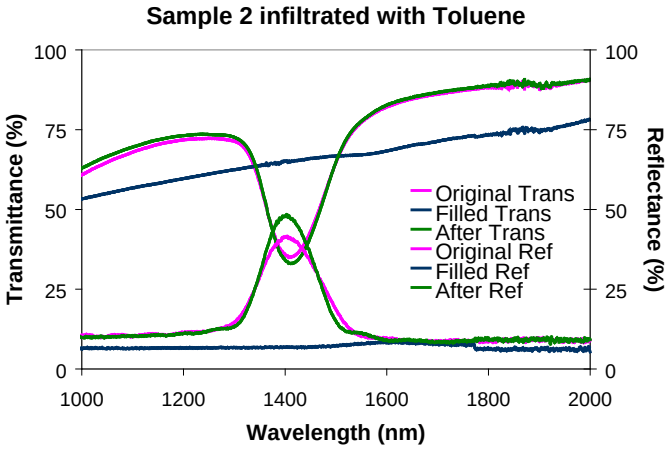

Figure 8. Transmission and reflection spectra of Sample 2 infiltrated with toluene.

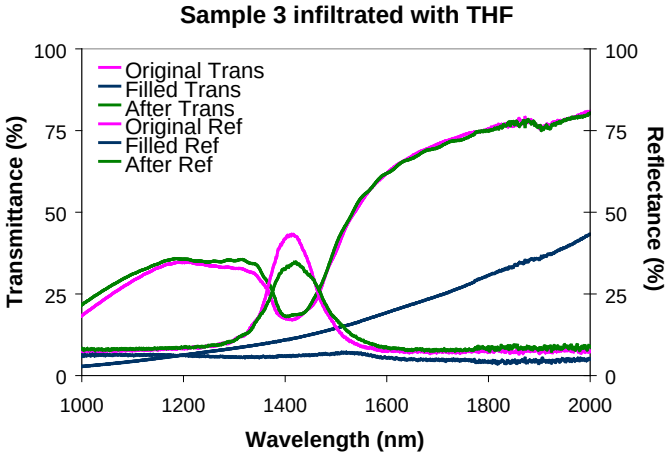

Figure 9. Transmission and reflection spectra of Sample 3 infiltrated with THF.

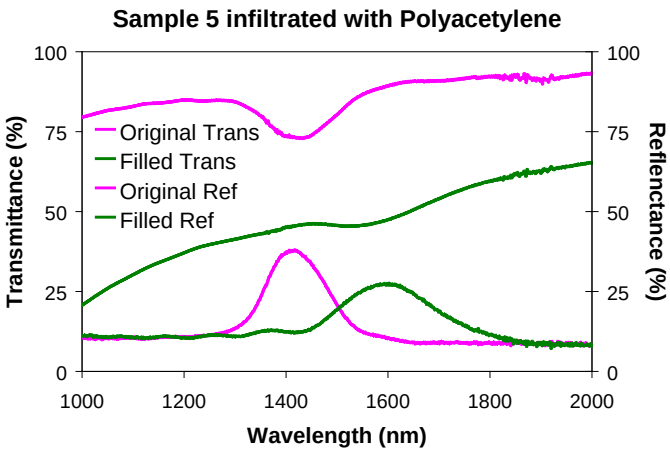

Figure 10. Transmission and reflection spectra of Sample 5 infiltrated with polyacetylene.

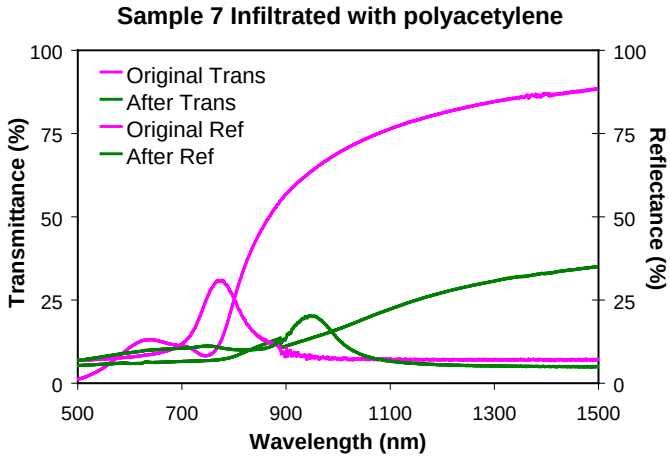

Figure 11. Transmission and reflection spectra of Sample 7 infiltrated with polyacetylene.

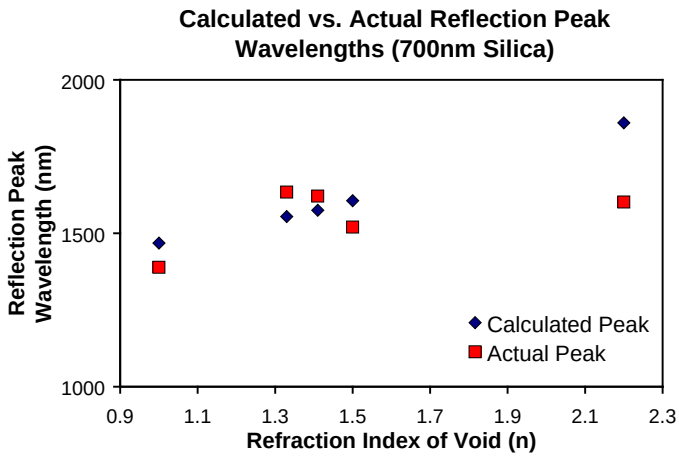

Figure 12. .Calculated vs. actual reflection peak wavelengths of 700nm silica opal films.

exception of the silica polyacetylene infiltration, whose reflection peak was shorter than the calculated wavelength by a 100-300nm. The results were much as predicted, since the effect of polyacetylene infiltration by capillary force would have a large disturbance on the microsphere packing structure and thus greatly reducing the PC efficiency. The reflectance and transmittance of water-filled PC is much lower than other infilled samples as a result of near-index matching. On the other hand, the reduced reflectance and transmittance of polyacetylene-filled PC is probably due to the large disturbance of packing structures during infiltration of more viscous polymer solution, some oxidation of polyacetylene during experimentation, as well as the inhomogeneity in polyacetylene infiltration of the area examined. In addition, the transmission peak of Sample 7 after polyacetylene infiltration cannot be observed because polyacetylene shows large absorption at similar wavelengths.

SEM images of the samples were taken and analyzed one week after start of polymerization. It was noted that the polyacetylene had penetrated to different depths in Sample 2 (see Figure 13) indicating good infiltration, as opposed to just coating the surface. However, the infiltration had disturbed much of the opal film structure and appeared to be very inhomogeneous throughout the whole film (see Figure 14). It is possible that the inhomogeneity of polyacetylene infiltration was caused by high molecular weight oligomers or polymers polymerizing and blocking the small PC void space as they penetrated into the opal film. Thus the rest of the lower molecular weight material was not able to continue penetration up the same path.

Conclusion

When infiltrating synthetic opal films with materials of different refractive indices, a shift of the reflection wavelengths of the PCs in the range of a few tens, and in the case of polyacetylene, a few hundreds of nanometers was observed. However, in most cases, the reflectance of the film became less effective as evident from the wider and shorter reflection peak band. SEM results showed the method of in situ polymerization can potentially be used to infiltrate polyacetylene into microstructures such as PCs, though the issues of inhomogeneity and structural alteration have to be further studied. In addition, the solvent used in the ROMP process (DCM) dissolved PS beads, so the influence of hydrophobicity on the film structure has yet to be investigated after neat ROMP or polymerizing utilizing a different initiator when infiltrating PS films. Additional experiments are currently being done to test polyacetylene-filled films.

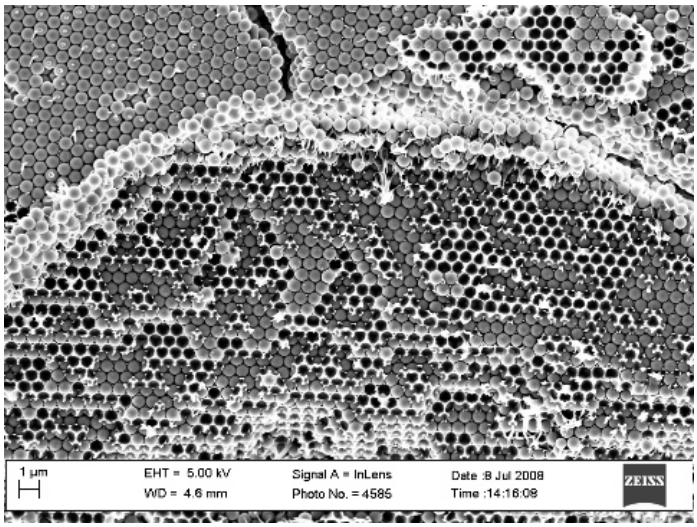

Figure 13. SEM of Sample 2 infiltrated with polyacetylene.

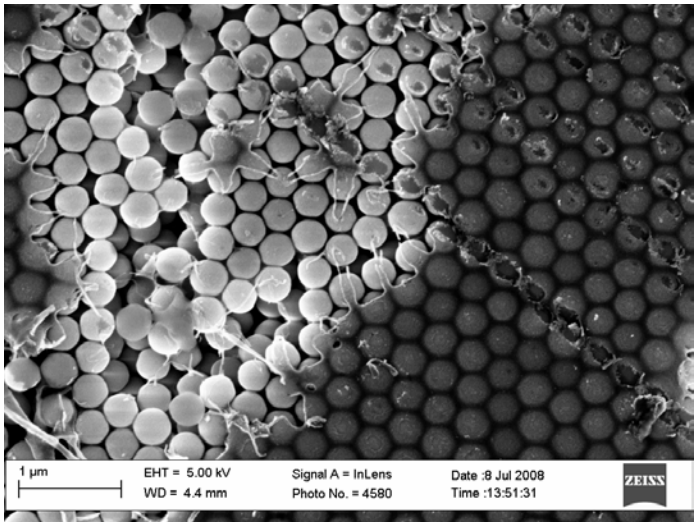

Figure 14. SEM of Sample 7 infiltrated with polyacetylene.

Acknowledgements

This research is supported by the National Science Foundation (NSF) and Center on Materials and Devices for Information Technology Research (CMDITR), DMR-0120967. I would like to thank the NSF, CMDITR undergraduate research program, Georgia Institute of Technology, and all coordinating personnel for providing me with the opportunity to carry out my research. I would also like to thank Dr. Joseph Perry, San-Hui Chi, Philseok Kim, Nicholas Haase and the rest of the Perry lab for patiently guiding me through my project.

References

1. P.N. Prasad, Nanophotonics, John Wiley & Sons, Hoboken, NJ, 2004.
2. C. López, Adv. Mater. 15 No. 20, 1679-1704 (2003).
3. Y. Xia, B. Gates, and Z. –Y. Li, Adv. Mater. 13 No. 6, 409-413 (2001).
4. B. Gates and Y. Xia, Adv. Mater. 12 No. 18, 1329-1332 (2000).
5. Z. –Z. Gu, A. Fujishima, and O. Sato, Chem. Mater. 14, 760-765 (2002).
6. E. Hecht, Optics, Addison Wesley, San Francisco, CA., 2002.
7. F. Meseguer, A. Blanco, H. Míguez, F. García-Santamaría, M. Ibisate, C. López, Colloids and Surfaces A: Physiochem. Eng. Aspects 202, 281-290 (2002).
8. S. –H. Chi, J. M. Hales, C. Fuentes-Hernandez, S. –Y. Tseng, J. –Y. Cho, S. Odom, Q. Zhang, S. Barlow, R. R. Schrock, S. R. Marder, B. Kippelen, J. W. Perry, Thick Optical-Quality Films of Substitued Polyacetylenes with Large, Ultrafast Third-Order Nonlinearities and Applications to Image Correlation, Adv. Mater., in press.
9. Based on the assumption that the volume of an opal film is 1cm (W) x 2cm (L) x 25μm (H), for FCC packing, the volume of the void space is 1cm x 2cm x 5 x 10^{-4} cm^3 x 0.26 = 13 x 10^{-4} cm^3 = 13 x 10^{-4} mL. The molecular weight of the monomer (n-butyl-COT, C12H16) is ~ 160 g/mol and the density is about 1 g/L, 13 x 10^{-4} mL = 13 x 10^{-4} g of monomer is needed, which is equivalent to 8.1 x 10^{-6} moles of monomer. Because the ratio of monomer to initiator (second generation Grubbs' initiator, M.W. = 848.97 g/mol) is ~ 450:1, the moles of initiator needed = 8.1 x 10^{-6} mol/450 = 1.8 x 10^{-8} mol. Thus the concentration of initiator solution needed is (1.8 x 10^{-8} mol)/(13 x 10^{-4} mL of void space) = 1.38 x 10^{-5} mM.

MENG KANG is currently a biomedical and mechanical engineering dual major at Duke University. She plans to obtain a Ph.D. in engineering after completing her undergraduate studies.

Two-Photon Polymerization of Hydrogels for Biological Applications

ANDREW KOLTONOW, University of Michigan
Ajit Bhaskar, Joseph Perry, Department of Chemistry , Georgia Institute of Technology

Background and Motivation

Multiphoton absorption polymerization (MAP) is a process where a polymerization reaction is initiated by the simultaneous absorption of two or more photons by an initiator. Because multiphoton absorption is nonlinear with respect to light intensity, it confines the reaction to the focal point of a powerful laser beam (see Figure 1), allowing for the fabrication of arbitrarily complex three-dimensional structures with sub-100nm resolution. This technique has been used to fabricate structures such as photonic crystals quickly and easily. However, the use of MAP has been largely confined to stiff resins[1].

Hydrogels are crosslinked polymeric materials that swell in water. Hydrogels are of particular interest in such biologically relevant applications as tissue scaffolds, because their properties can be tailored to mimic a variety of tissues. Recent evidence suggests that interactions between cells and scaffolds are controlled to a large extent by the texture of the scaffold[3], and for this reason future applications may depend on the ability to pattern hydrogel structures in three dimensions with sub-micron resolution.

If MAP could be adapted to hydrogel materials, it would offer a far greater degree of control over the features formed than is currently available for these materials. Perhaps more importantly, because the process uses infrared light instead of ultraviolet, it may allow structures to be fabricated in situ, obviating the need for surgical implantation. However, before MAP can be extended to these materials, the materials must be studied using conventional single-photon methods to form a basis for comparison.

The purpose of this work is to examine the relationship between the composition of the gel, the exposure conditions, the feature resolution, and the ability of the gel to swell in water, and to identify compositions for later MAP studies.

Figure 1: A fluorene dye is excited in single-photon absorption (left) and two-photon absorption (right). Note that the singlephoton absorption takes place over the entire volume accessed by the beam, while the two photon absorption is confined to the focal volume.[2]

Methods

All chemicals are purchased from Sigma – Aldrich unless otherwise noted and were used without any additional purification. Mixtures of varying proportions of the monomers 2-hydroethyl methacrylate (HEMA) and N-vinyl-1-pyrrolidinone (NVP), one of the two crosslinkers ethylene glycol dimethacrylate (EGDMA) and poly(ethylene glycol) dimethacrylate (PEGDMA) (average M_n = 850), and the commercial photoinitiator Irgacure 819, purchased from Ciba Inc., were made. A clean glass substrate was functionalized with methacrylate groups by rinsing with a solution of 3-(trimethoxysilyl) propyl dimethacrylate in methanol and baking dry. The substrate was placed in contact with the monomer mixture, so that the functionalized surface of the glass would be incorporated into the polymer. The sample was polymerized by a single-photon absorption, by exposing to ultraviolet light at 365 nm (Blak-Ray, model B 100) through a patterned mask for the prescribed amount of time, as illustrated in Figure 3. The resulting gel was soaked in polar solvent for approximately 1-2 hours to remove unreacted monomer. Optical microscopy was performed to estimate feature resolution, and contact profilometry was performed to estimate the cross-sectional areas of features. Samples were then swollen overnight in either deionized water or aqueous phosphate-buffered saline solution, and examined for swelling by optical microscopy, contact profilometry, and fluid mass uptake measurements. The viscosity of the monomer mixture was altered by the addition of known biocompatible polymers that are not expected to take part in the polymerization reaction, and was estimated by visual inspection.

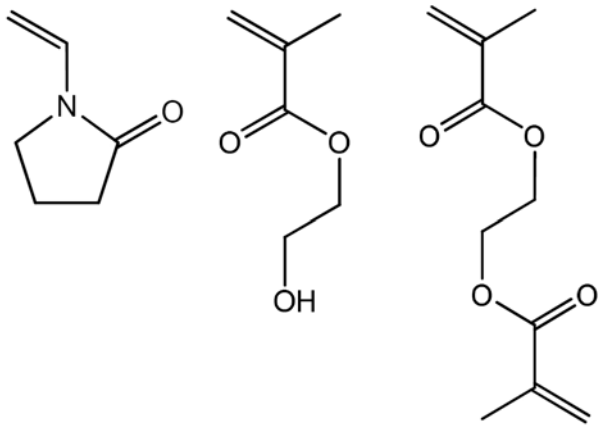

Figure 2: Monomers used. Left: N-vinyl 2-pyrrolidinone (VP) Center: 2-hydroxyethyl methacrylate (HEMA) Right: ethylene glycol dimethacrylate (EGDMA) PEGDMA (not pictured) is similar to EGDMA, but with a longer bridge between the two methacrylate groups.

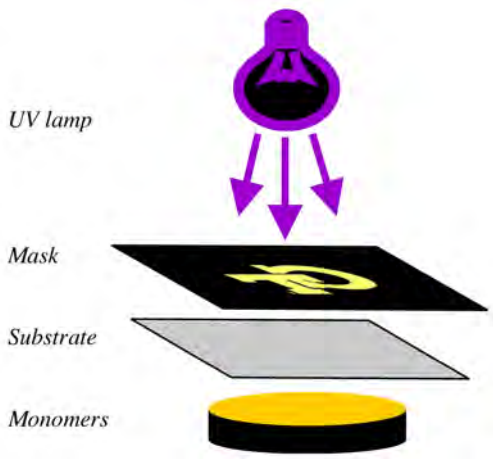

Figure 3: Schematic of setup used to form hydrogel structures on substrate.

Results

As the proportion of crosslinker in the monomer mixture decreased below 15% by weight, or the proportion of initiator decreased below 10%, the size of the smallest resolvable features increased dramatically. This trend is illustrated in Figure 4. At the higher concentration of crosslinker and initiator, features as small as 40-50 microns could be distinguished. When the fraction of crosslinker present was halved to 7.5%, the minimum feature size doubled, to 80-100 microns. A similar, but slightly less dramatic trend was noted with regard to the initiator concentration. As the crosslinker fraction was halved, the minimum feature size increased by approximately 50%. Very little variation in resolution was observed at higher concentrations of crosslinker, nor between the two different crosslinkers studied.

Mass uptake measurements taken on a sample exposed without the mask detected a small amount of swelling. However, profilometry measurements of patterned samples showed no significant swelling.

The monomer mixtures containing PEGDMA appear to be more viscous than those containing EGDMA. Additionally, those mixtures in which other biocompatible polymers dissolved appear to show increased viscosity, roughly corresponding to the amount of polymer dissolved. The most viscous of these is the mixture saturated with about 8 mass percent cellulose, with a honey-like consistency. This mixture has been patterned, but the resulting gel has not yet been imaged or swollen.

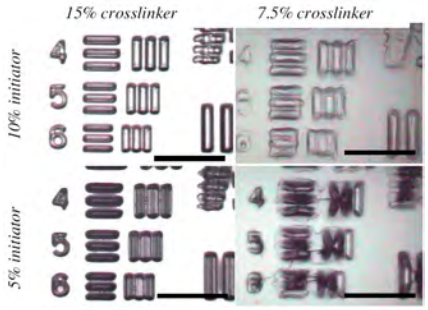

Figure 4: resolvable feature size versus composition. Decreasing the amount of crosslinker or initiator in the system leads to a marked decrease in resolution. Scale bar is 1 mm.

Discussion

While other researchers report swelling factors or 20 to 50 percent for bulkpolymerized gels of the compositions used here[4], no significant swelling was seen in these patterned samples. This discrepancy likely arises from the difference in extent of reaction. The work cited involved reacting all of the monomer to form a gel, guaranteeing that the bulk composition of the gel directly corresponded to the composition of the monomer mixture used. However, in the case presented here, very little of the monomer mixture is allowed to react, and so the bulk composition of the gel is dictated by the kinetics of the reaction.

In the copolymerization of HEMA and VP, HEMA has been shown to add to the growing chain end much faster than VP, regardless of which species the radical is on. In the copolymerization of HEMA and EGDMA, EGDMA reacts with the radical much faster than HEMA[5]. A kinetic study of the three component system (HEMA/VP/EGDMA) has not been published, but there is reason to expect that EGDMA will react far faster than the other two components. Since only a small portion of the monomer mixture in the cell is polymerized, the composition of the solid will depend on the rates at which the various monomers react, and so the solid material likely contains a much greater fraction of EGDMA than the original monomer mixture did. This would almost certainly prevent the material from swelling noticeably. To control the composition of the hydrogel structures in single-photon absorption polymerization and MAP, it is necessary to know the reactivity ratios of the components. This might be achieved by compositional analysis of the alreadypatterned samples.

One factor preventing the patterning of samples with lower crosslinker concentrations is the sharp loss of resolution as crosslinker concentration decreases below about 15% (note: that is to say, 15 wt% crosslinker in the unreacted monomer mixture). It has been suggested that the drop off in resolution is caused by an increase in the amount of time taken for the material to reach its gel point (the point at which the polymer chains are sufficiently entangled that the material will behave as a solid). Prior to the gel point, the polymer is somewhat more free to flow about, and so the formation of the solid is not confined to the points that were exposed to light.

From this it follows that the resolution issue will persist under two-photon exposure conditions, as it is not related to the initiation of the reaction. It also follows that the resolution issue can be improved by decreasing the time it takes the material to gel once initiated. This can be done by increasing the amount of crosslinker used, or by increasing the functionality of the crosslinker. Alternately, this can be done by beginning the polymerization with oligomers instead of monomers – the critical size can be reached faster by building the chain from longer links. The latter approach essentially amounts to decreasing the amount of units that need to react before the gel point is reached.

This problem might also be addressed not by reaching the gel point faster, but by inhibiting diffusion, so that a growing chain would take longer to move a unit distance away from the point where it was initiated. This would allow the reaction to take place over a longer time scale while still allowing the pattern to be well resolved. This might be achieved by conducting the reaction below room temperature. Altering the temperature would slow the reaction, however, and the

net effect might be undesirable. Also, if this reaction is intended to be conducted in vivo in the (distant) future, then it would not be prudent to pick a methodology that requires the monomer to be chilled. Another route by which a decrease in diffusion might be achieved is increasing the viscosity of the starting monomer mixture, by dissolving cellulose acetate or a similar polymer in the neat monomer. Study of the pattern formed from the cellulose acetate-containing mixture might yet reveal an improvement in resolution.

The use of a longer crosslinker does not appear to detriment the resolution of the pattern. It has not been shown whether the use of the long crosslinker will affect the swelling of the gel, as no swelling has been observed. There is still reason to expect that the long crosslinker will increase the amount of swelling in a swellable gel, for multiple reasons. The longer bridge should create more space in the gel for water molecules to fill. The greater mass means that compared to the short linker, the long crosslinker will have a lower crosslink density. Because the long crosslinker has a weight higher than the entanglement weight of PEGDMA, it is also possible that one of the two ends will be hidden in the coils of the chain, and the molecule will not form a crosslink. In that sense, some of the PEGDMA molecules may simply act as monomers with very large pendant groups.

Future work

A recommended next step in this work is toexamine the kinetics of the reaction. In orderto make structures of predictable composition, it is necessary to know the reactivity ratios of all the components of this system with respect to one another. These might be determined by compositional analysis of already patterned samples. A study of the relationship between composition, diffusion coefficient, and time-to-gel would allow for the prediction of the resolution limit, though for the purposes of this project it may suffice to simply establish an empirical relationship between the composition and the resolution limit. A rudimentary understanding of the kinetics of this reaction would be vital to anyone trying to design an MAP-formed hydrogel to specifications.

Another essential task is to explore means of improving feature resolution in lightly crosslinked samples. As discussed previously, this might be accomplished by using oligomers instead of monomers or multifunctional branching linkers instead of two-functional crosslinkers to decrease the time-to-gel.

The addition to the mixture of hydrophilic polymer chains that won't be incorporated into the gel is a modification that may serve several purposes. It would effectively make the unreacted monomer mixture more viscous. This may decrease the diffusion effects that allow the chain to drift away from the spot at which it was initiated, though a decrease in diffusion coefficient may slow the reaction, negating the beneficial effect of preventing chain movement. A decrease in viscosity may also make convection more difficult, thus slowing the drift of chains and simplifying heat transfer issues.

Once these issues are resolved, hydrogel scaffolds will be fabricated by MAP and studied to reconcile any differences between the single-photon polymerized and MAP hydrogels.

The system might then be altered to incorporate biodegradable links, so that a biodegradable scaffold can be patterned. This would be of interest in applications where a temporary scaffold is called for. Similarly, dyes might be incorporated into the polymer, allowing the scaffold to be easily imaged. There is a vast variety of other functionalities that might be incorporated.

Conclusions

MAP is an interesting means of fabricating structures in three dimensions with submicron resolution. It may be possible to extend this method to hydrogel materials, opening up a variety of otherwise unrealizable applications. A mixture of HEMA, VP, and a dimethacrylate

crosslinker has been studied with the intention of optimizing it for MAP. Progress has been made, but problems with swelling and resolution persist, so the system is not yet ready for MAP.

Acknowledgements

This work was supported by the STC Program of the National Science Foundation No. DMR 0120967. Thanks to Dr. Andrew Lyon for his helpful advice.

References

1. L. Li and J.T. Fourkas. Mater. Today 2007, 10, 6, 31-37
2. Belfield Group website, Univ. of Central Florida. Accessed 7/21/2008. http://belfield.cos.ucf.edu/
3. L. Richert et al. Adv. Mater. 2008, 20, 1488–1492.
4. D.M. Blanco et al. J. Biomater. Sci. 1997, 8(9), 709.
5. N. Ajzenberg et al. J. Appl. Polym. Sci. 2001, 80, 1220.

ANDREW KOLTONOW is a junior at the University of Michigan in Ann Arbor, Michigan. He plans to pursue a Ph.D., possibly in polymer chemistry.

Layer-by-Layer Assembly of CdTe and CdSe Semiconducting Nanocrystals: Toward Solution Processable Inorganic Type-II Heterojunction Solar Cells

AVERY LINDEMAN, Harvard College
Clayton Shallcross, Neal Armstrong, Department of Chemistry, University of Arizona

Introduction

Modern society relies heavily on non-renewable, ecologically unfriendly sources of energy like coal and fossil fuels. However, as energy demand increases, it is clear that these methods will be unable to sustain our current way of life in the long-term. In an effort to satisfy global energy needs while reducing greenhouse gasses released into the atmosphere as a result of energy production, solar power—which is present in large amounts all over the planet but which is, as yet, a largely unused energy source—must play a greater role in the production of the world's power. Current commercially available photovoltaic devices, such as those made from crystalline silicon, are efficient, but also extremely costly, limiting their ability to make a large-scale impact in energy production. Conversely, organic photovoltaic devices (which are less expensive due to less expensive materials and ease of processibility relative to traditional silicon solar cells) are not yet efficient enough to be implemented commercially. An alternative is sought in an effort to produce a solar cell that is both efficient and affordable enough to be realistically implemented. For this purpose, layer-by-layer thin films of CdTe and CdSe nanocrystals (NCs) are investigated as potential components of a type-II heterojunction solar cell.

Background

Nanocrystals are an attractive material for photovoltaic research due to their broadband absorption and charge transfer properties, as well as their distinct size-dependent energetic characteristics (band gap, absorbance) that result from the quantum confinement of electrons in the NCs.[1, 2] Combining layers of two different kinds of NCs has been proposed to lead to a new type of photovoltaic device (the "Type II Heterojunction"). The favorable movement of electrons upon photoexcitation is driven by the staggered energy levels of the NCs (Figure 1).[1]

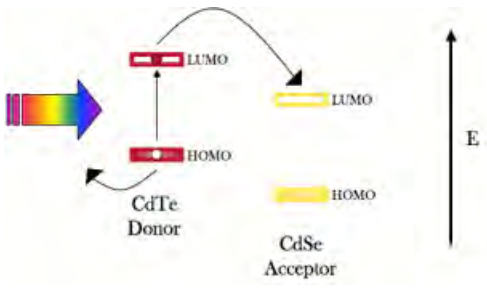

Figure 1. An energetic depiction of the NC donor-acceptor solar cell.

Semiconductor NCs present a cost-effective, solution processable alternative to organic photovoltaic devices (OPVs). The production and efficiency of solar cells made via Layer-by-Layer (LbL) deposition was investigated by first developing a standard LbL procedure and then by fabricating and testing devices on LbL bilayer thin films.

In LbL deposition of NC thin films, NCs are deposited approximately one layer at a time by repeatedly dipping an activated ITO-on-glass substrate into NCs dissolved in hexanes and alternating with dips in 0.1 M ethanedithiol (EDT) solution (thought to remove some of the ligands left on the surface of the NCs from the synthesis process). Figure 2 illustrates the LbL deposition method as proposed by Nozik et al.[3]

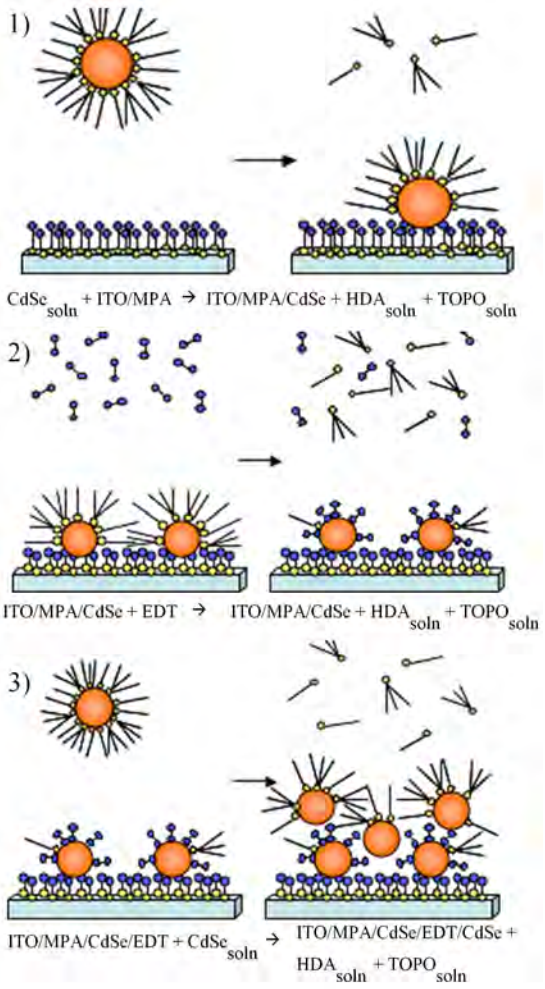

Figure 2. LbL Deposition of HDA/TOPO capped CdSe NCs onto MPA-activated ITO. Steps 2 and 3 are repeated until the film reaches the desired thickness, allowing time to dry in between dips. The replacement of HDA/TOPO (on CdSe crystals) and ODE (on CdTe crystals) with EDT reduces the spacing between NCs and generates a more tightly packed film, ideal for device fabrication.[1]

Methods

Materials

HDA/TOPO capped CdSe Nanocrystals (30% ligand by mass) in hexanes, 8-octadecene (ODE) capped CdTe Nanocrytals (60% ligand by mass) in hexanes, ethanedithiol (EDT), 3-mercaptopropionic acid (MPA), acetonitrile, hydroiodic acid (HI), cadmium chloride ($CdCl_2$), methanol (CH_3OH), Al wire, ethanol-cleaned 1"X1.5" pieces of ITO.

Layer-by-Layer Assembly of NC Films

Unless specified, all processing occurred inside a nitrogen glove box. HI-etched MPA-activated ITO was dipped for several seconds in filtered (0.45um) NC solution, then removed slowly; excess moisture was wicked away from film. Dry film was then dipped for 5 seconds in 0.1 M EDT solution in acetonitrile, removed, and allowed to dry. This dipping cycle was repeated to generate the desired film thickness (measured in dip number). NC concentration and dipping time were both investigated for their effects on film quality.

Layer-by-Layer Assembly of NC Bilayer Films

The dipping process was executed with 1.5 mg/mL CdTe solution for desired thickness (25 dips). Subsequent layers of CdSe were deposited with the same procedure (first with 0.1 mg/mL CdSe, and then with 2.0 mg/mL CdSe solutions, 10 dips in each). All solutions were filtered before dipping using a 0.45um syringe filter.

Sintering and Annealing of Bilayer Films

Select films were sintered using a well-known technique[4]: a saturated solution of $CdCl_2$ in methanol was filtered (0.45 um) and spin-cast onto bilayer films; films were then heated for 15 minutes at 200 °C, removed quickly, and allowed to cool. Excess $CdCl_2$ was removed from the film by rinsing in deionized water. Sintered films were returned to N_2 glovebox to prevent film oxidation. Annealed films were heated at approximately 200 °C for 15 minutes in N_2 glove box.

Thin Film Characterization

Thin-film morphology was obtained using Scanning Electron Microscopy (SEM); absorbance data was obtained using UV-visible spectroscopy. Absorbance data was taken at five distinct spots on each film (two locations at the top, one in the center, and two at the bottom of the dipped region) to investigate film uniformity and ensure accurate average absorbance values.

Device Fabrication and Testing

Al contacts (100 nm thick) were deposited directly onto the CdSe surface of the bilayer thin films using physical vapor deposition. Current-voltage device (*J/V*) data was obtained using a 100mW illumination source. IPCE data was obtained using a white light illumination source, passed through a J-Y holographic grating monochromator and then demodulated with a lock-in-amplifier. Photocurrent efficiencies were calibrated using a calibrated silicon photodiode.

Results and Discussion

Monolayer film quality was investigated as a function of concentration of NC solution as well as dipping time in NC solution. Of these two factors, NC concentration appeared to play the most significant role in films of CdSe: SEM images of films made from 4 mg/mL CdSe in hexanes (Fig. 3a) showed significant cracking across the surface of the films, suggesting that too many layers of NCs were being deposited in any given dip (the same cracking can be seen in EDT treated spin-cast films assembled by Nozik et al[2]). Consistently smooth films (ideal for Al deposition) were generated when the NC solution was diluted to 2mg/mL (Fig. 3b). CdSe films produced by repeated 5-second dips in NCs displayed no significant difference in quality from films produced by repeated 15-second dips in NCs.

Due perhaps to the different ligands on the surface of the CdTe NCs versus the CdSe NCs, or to the higher ligand-to-NC ratio observed in the CdTe (60%) versus the CdSe (30%), dipping time played a greater role in the deposition of CdTe films, while NC concentration continued to have a large influence on film quality. Films assembled from 5-second dips in 1.5 mg/mL CdTe (Fig. 3c) were consistently porous and textured, ideal for the subsequent deposition of CdSe in device fabrication (more surface area at the interface between the donor and acceptor materials may increase device efficiency as a result of increased electron diffusion).[5]

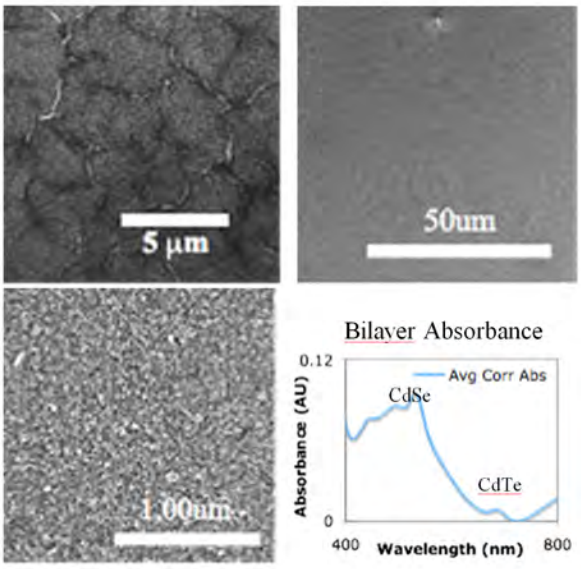

Figure 3: SEM of monolayer NC thin films (clockwise from top left). (a) Film made from 4mg/mL CdSe solution. (b) Film made from 2mg/mL CdSe solution. (c) Film made from 5-second dips in 1.5mg/mL CdTe solution. (d) Absorbance data for a bilayer film.

Characterization of Bilayer Thin-films with UV-visible Spectroscopy and SEM

SEM of bilayer films confirmed the smoothness of the top CdSe layer onto CdTe films (Fig. 3d). Absorbance data taken of bilayer films displayed two excitonic peaks corresponding to the first excitonic peaks of both CdTe and CdSe, suggesting that the bilayer absorbance across the visible spectrum is comprised of a linear combination of the absorbencies of CdTe and CdSe (Fig. 3d).

Evaluation of Devices

Devices made from as-prepared bilayer films were extremely inefficient and displayed very low short-circuit current (J_{sc}) and open-circuit voltage (V_{oc}) values. Devices made from oxidized films had equally disappointing J-V curves.

Device efficiency was improved by sintering or annealing the bilayer films prior to Al deposition. Sintering in air in the presence of $CdCl_2$ proved extremely beneficial under certain conditions (the most promising J-V curve, shown in Figure 4a, is of a sintered film); however, heating beyond 200 °C or for longer than 15 minutes had a detrimental impact on the quality of devices made from the film (Figure 4b). Annealed films with limited exposure to oxygen also generated decent J-V curves, although results were not as promising as those obtained for the sintered devices.

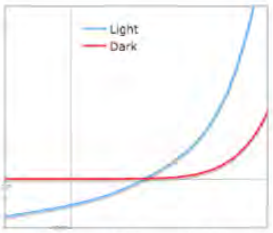

	V_{oc}	J_{sc}	P_{max}	FF	Efficiency
300C	0.51	-1.25	-.15	0.23	0.15%
200C	0.57	-5.32	-0.94	0.31	0.94%

Figure 4. Current-voltage data for devices made from bilayer thin films. (a) Light and Dark J-V curves for the best device made from a sintered thin film (15 min 200C). (b) J-V data for devices made from films that lost NC character when sintered (300C) vs. films that did not.

IPCE Data and its Implications

Incident Photon Current Efficiency data for the sintered film mirrored the absorbance data taken for the same film (Figure 5a). This implies that NC character was preserved in the sintering process, and that both the CdTe and CdSe layers contributed to the generation of photocurrent in the device. IPCE data for the film annealed in N_2, shown in Figure 5b, displays a clear drop-off in photocurrent generation beyond the first excitonic peak of CdTe, but gives little indication of the CdSe and CdTe excitonic peaks observed in the sintered film. This could imply that nanoparticle character was lost in the annealing process, but further investigation of the annealing process is necessary before such a conclusion can be definitively reached.

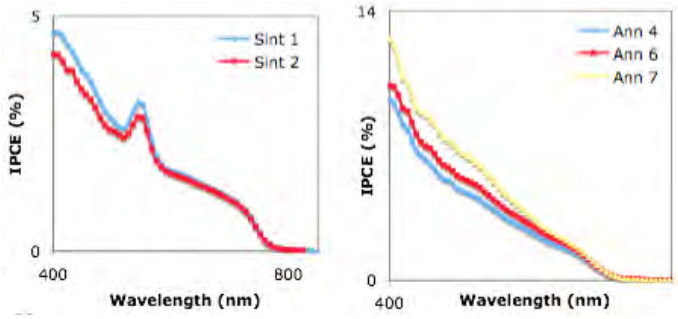

Figure 5. (Clockwise from top) IPCE data for (a) sintered and (b) annealed films.

Conclusions

To assemble an effective PV device using LbL-assembled thin films of CdTe and CdSe, films must be sintered in the presence of $CdCl_2$ or heated in the absence of air. The heating and sintering processes likely serve to decrease the distance between NCs, thereby increasing the ability of electrons to travel through the film. Nanoparticle character should be retained during the sintering process in order to retain generation of photocurrent within the cell. Further study is required to optimize the sintering process.

By varying the thickness of the CdTe and CdSe layers within the film, device efficiency and photocurrent generation could be improved. An in-depth study of the effect of layer thickness on device specifications is needed to maximize the output of these CdTe/CdSe NC solar cells. Further study is also required to determine the exact effect of relative nanocrystal size on device efficiency. Once a variety of NC size combinations and layer thicknesses have been explored, processing conditions can be optimized to generate solar cells with improved output.

Further investigation must also be conducted to improve the interface between the CdTe and CdSe layers; a clean interface reduces the possibility of recombination of electron-hole pairs, thereby maximizing photocurrent, but the current LbL method results in some mixing of CdTe and CdSe at the interface of the bilayer due to solubility of the NCs in hexanes (seen in absorbance data of NC solutions after bilayer fabrication). By briefly heating the CdTe thin-film to remove excess ODE prior to CdSe deposition (theoretically reducing the solubility of the NCs at the surface), mixing of the NCs at the interface of the bilayer could be minimized.

Additional future directions for this research include the incorporation of a charge-carrier layer such as C_{60} between the NC film and the Al contact, as well as the already-active research area of utilizing NCs as absorbent layers in other PV devices.

Acknowledgements

Funds for this research were provided by the Center on Materials and Devices for Information Technology Research (CMDITR), and the NSF Science and Technology Center No. DMR 0120967.

Special thanks to Dr. Armstrong and Clayton Shallcross for taking on a laboratory newbie. Thanks also to Dio Placencia for his help with physical vapor deposition and for copious troubleshooting in the lab.

References

1. Gur, I; Fromer, N. A.; Geier, M. L.; Alivisatos, A. P. Air-Stable All-Inorganic Nanocrystal Solar Cells Processed from Solution. Science 310 (2005).
2. Murray, C.B.; Norris, D. J.; Bawendi, M. G. Synthesis and Characterization of Nearly Monodisperse CdE (E = S, Se, Te) Semiconductor Nanocrystallites. J. Am. Chem. Soc. 115, 8706-8715 (1993).
3. Luther, J. M.; Law, M; Song, Q.; Perkins, C. L.; Beard, M. C.; Nozik, A. J. Structural, Optical, and Electronic Properties of Self-Assembled Films of PbSe Nanocrystals Treated with 1,2-Ethandithiol. ACSNano 2(2); 271-280 (2008).
4. McCandless, B. E.; Moulton, L. V.; Birkmire, R.W. Recrystallization and Sulfur Diffusion in CdCl2-Treated CdTe/CdS Thin Films. Prog. Photovolt. Res. Appl., 5, 249-260 (1997).
5. Forrest, S. R. The Limits to Organic Photovoltaic Cell Efficiency. MRS Bulletin 30 (2005).

AVERY LINDEMAN is a Chemistry concentrator at Harvard College. She has nebulous plans to continue in academia.

Dickson Charge Pump Measurements for Comparison of Voltage Gain Efficiencies with Organic Solar Cells

DANIEL J. LUM, Louisiana State University
Matthew Trotter, Gregory Durgin, Department of Electrical Engineering, Georgia Institute of Technology

Introduction

Organic solar cells have recently been introduced that exhibit characteristics desirable for DC power production. They are lightweight, and flexible, and above all, cheaper than ordinary silicon solar cells. One serious drawback is their poor power efficiency, which has never exceeded five percent . In contrast, their silicon counterparts produce power at approximately 20% efficiencies for commercial cells. These organic solar cells offer a greater hope for greener renewable energy applications because of their durability and low cost. However, an alternate problem associated with their alignment must first be overcome. When designing power supply systems from organic solar cells, a designer may attempt to arrange them in a typical rectangular solar cell array, but this may not be the most efficient method for increasing their output voltages to levels required by everyday electronic applications. Current research is attempting to determine whether Dickson charge pumps with an organic solar cell array input can prove to be a more efficient design solution that boosts the voltage to practical levels while maintaining high power efficiency. This summer, the objective is to calculate and measure the power efficiencies of a two-, four-, six-, and eight-stage Dickson charge pump to find the most compatible circuit for optimal organic solar cell performance.

Experimental

The first step is to analyze the Dickson charge pump with analytical methods to derive equations for power efficiency, which may be dependent on the number of stages, diode threshold voltage, stage capacitance, output capacitance, load resistance, and input voltage. Calculating the highest efficiency for each circuit design is a challenge because multiple variables are involved in the calculation and are, in many cases, interdependent. A logical solution is to manipulate the equations that govern this particular circuit and monitor the effects. If an equation representing the efficiency in terms of capacitance, frequency, and resistive load can be derived, perhaps a maximum could be acquired from basic calculus techniques. Unfortunately, this circuit is nonlinear and analytical methods are impractical.

An alternate approach using simulation software may be a more beneficial solution. PSpice is a circuit simulation program that can handle complex mathematical expressions and display results graphically. In the simulator, the designer can calculate the equivalent resistance of the solar cell power circuitry and match the load resistance for optimal power transfer. Once the optimal load resistance is determined, the excitation frequency within the circuit can be varied to yield the highest efficiency when given a specific input voltage. Another benefit of using this simulator is its ability to optimize a circuit. Assuming certain parameters are specified, the program has the capability of enhancing the performance of the circuit by tweaking those parameters to arrive at a desired outcome. Once theoretical models of the solar cells have been designed, these circuits will be built and tested.

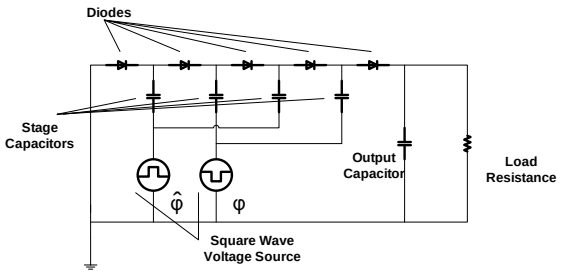

Figure 1. A four-stage Dickson charge pump schematic as drawn in PSpice.

Four Dickson Charge pumps composed of two, four, six, and eight stages were designed. Figure 1 shows a four-stage Dickson charge pump. The capacitors were set in series and separated by the diodes to direct the current and multiply the voltage from a power source. Two, out of phase, square-wave voltage sources were added to the circuit to represent the voltage signal coming from a clock circuit powered by the organic solar cells. This timer circuit is actually composed of a timer and an inverter that generate a square wave voltage. This square wave voltage is essential for the charge pump because it allows one half of the capacitors to charge while the other half discharge and vice-versa. It is this motion that allows the circuit to pump the voltage. The rise time of the clocks in the simulations were made almost ideal with a negligible duration of one nanosecond. The output capacitance needed to be large enough to reduce the large ripple voltage produced at the load and was set to be three times the value of a stage capacitor. The values of the load resistance, the clock frequency, and the stage capacitance were set to be parameters that were constantly altered according to a weighted scale by the PSpice Optimizer in an attempt to reach the highest possible efficiency while maintaining a relatively high voltage gain. Higher efficiency received preference over voltage gain. Stage capacitance was ignored.

$$V_{out} = V_{in} - V_t + N\left[\left(\frac{C}{C+C_S}\right)V_{in} - V_t\right] - \frac{N \cdot I_{out}}{(C+C_S)f} \quad (1)$$

Equation 1 represents output voltage as a function of input voltage, diode threshold voltage, number of stages, stage capacitance, stray capacitance, output current, and frequency[2]. From Equation 1, high frequencies improve the voltage gain and reduce actual

stage capacitance needed but do affect the capacitor's ability to charge and discharge based on their RC time constant. Dickson also demonstrates that the circuit resistance is also dependent on frequency[3].

$$Rs = \frac{N}{(C + Cs) f} \qquad (2)$$

As seen in Equation 2, a greater frequency yields a lower circuit resistance. Therefore, greater frequencies are favorable but are limited by the RC time constant as mentioned earlier. However, others have shown that optimal performance frequencies lie in the megahertz range[2].

In the simulations, the power efficiency was measured by dividing the time averaged output power through the resistor by the time averaged sum of the two input power sources. The time average was actually a moving time average over 9 microseconds. The only variables not altered by the PSpice Optimizer were the number of stage capacitors and the input voltage. The input voltages were varied in even numbers from 2 to 10 volts for each of the 4 circuits, which make 20 simulations. A total of 84 simulations were recorded. The extra 64 simulations were taken to ensure the power efficiencies were not due to local minima or maxima within the program.

Simulation Results

Maximum efficiencies of approximately 60% were expected at the two-stage circuit and were predicted to drop with every additional stage. Instead, the maximum power efficiencies approached 90% whereby the lowest efficiencies were actually recorded at the two-stage circuit. In addition, the simulated efficiencies only increased with increasing voltage up to the maximum input at 10 volts. These results also suggest that the efficiency is not inversely proportional to the stage number, which is counter-intuitive. The method by which the power efficiencies were measured may not be exact but appear to be the best available method. An alternate method aside from PSpice is to mathematically solve in terms of charge moving through the system as shown by Tanzawa and Tanaka . Figures 2 and 3 are three-dimensional plots of the results.

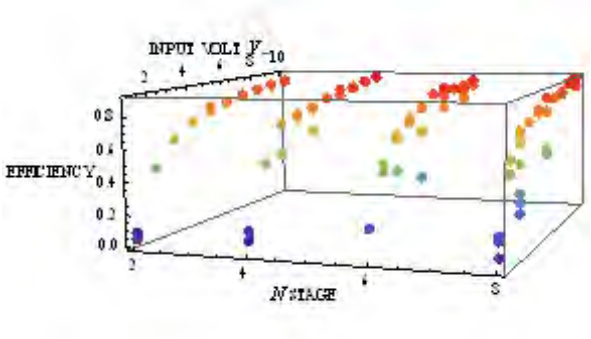

Figure 2. The efficiency from PSpice simulations in terms of stage number and input voltage

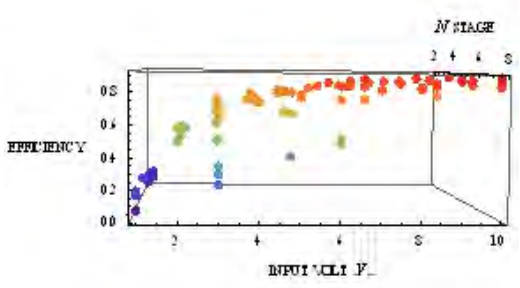

Figure 3. The efficiency from PSpice simulations in terms of stage number and input voltage (Alternate View)

Maximum efficiencies of approximately 60% were expected at the two-stage circuit and were predicted to drop with every additional stage. Instead, the maximum power efficiencies approached 90% whereby the lowest efficiencies were actually recorded at the two-stage circuit. In addition, the simulated efficiencies only increased with increasing voltage up to the maximum input at 10 volts. These results also suggest that the efficiency is not inversely proportional to the stage number, which is counter-intuitive. The method by which the power efficiencies were measured may not be exact but appear to be the best available method. An alternate method aside from PSpice is to mathematically solve in terms of charge moving through the system as shown by Tanzawa and Tanaka . Figures 2 and 3 are three-dimensional plots of the results.

Figure 3 shows a common property of the Dickson charge pump at lower input voltages. There is a dramatic drop in efficiency below 2 volts. Therefore, these solar cells will need to be initially stacked to provide at least 2 volts for these pumps to operate at approximately 50% efficiency. Greater voltages are ideal, but are limited by the efficiency of stacking solar cells. In the end, the number of stages will need to be determined by the required output voltage and the load resistance.

Once the simulations were complete, each circuit was built on a breadboard. A 555 timer and a CMOS complementary inverter were used to generate a square wave voltage. At first, the wave was very weak and could not support the circuit. The three transistors within the CMOS series inverter were then placed in parallel and provided enough current driving capability to power the circuit. The frequency was then altered by switching in different clock capacitors in parallel and in series until frequencies of 100 kHz, 200 kHz, and 300 kHz were achieved with respectable square waves. The power efficiency can be determined by the following equation[2]:

$$\eta = \frac{Pout}{Pin} = \frac{Vout * I_{Load}}{I_{Consumption} * Vi} \qquad (3)$$

$$\eta = \frac{Vout}{Vin\left[(N+1) + \left(\frac{N * Cp * Vin * f}{I_{Load}}\right) + \left((2N+1) * \frac{Cs}{C+Cs}\right)\right]}$$

Equation 3 shows efficiency as a function of input voltage, diode threshold voltage, number of stages, stage capacitance, stray capacitance, current, and frequency. The diode threshold voltage is the voltage drop across each diode, which is about .7 volts for the

common diodes used in the measurements. Stray capacitance is unwanted capacitance between any two conductors close together within a circuit. A more general definition was implemented because stray capacitance was assumed to be zero and the current measurements through the resistor were inaccurate.

$$\eta = \frac{Vout^2}{Rload * I\_load * Vin} \quad (4)$$

Equation 4 defines the efficiency in broader terms of the squared output voltage, the load resistance, and finally both the current and voltage entering the circuit. When the circuits were tested, three other variables apart from the frequency were changed. The second variable involved the two clock resistances of the 555 timer. These two resistances were interchanged throughout in three different pairs of 51 kΩ and 1 kΩ, 510 kΩ and 10 kΩ, and finally 1 MΩ and 20 kΩ. Input voltage was the third variable. The minimum input voltage needed was determined to be 2.5 volts. This was near the minimal value needed to drive the circuit and the 555 timer. This result corresponded well with the predicted minimal value. Five volts and 10 volts were also used. Once testing began, it was noted that the square wave and frequency were heavily dependent on the size of the load, the fourth variable, which imposed a lower limit of approximately 36 kΩ before the square wave was deformed and boosting no longer resulted. Other loads included 100 kΩ and an open circuit to find the maximum voltage gained. In all, there were 324 different variations to the four circuits that needed to be tested.

Circuit Measurement Results

Once testing was completed, there was a dramatic difference in the simulated efficiencies and the measured ones. In these measurements, the highest efficiencies occur at approximately 30% - a great deal lower than the 90% efficiencies predicted by PSpice. In the measurements, the efficiency also appears to be more dependent on the stage number than the simulations would suggest. However, there is a general trend: as the stage number and voltage increase, the efficiency increases. At some point it is suspected that these efficiencies will eventually level off and yield lower values. In addition, one calculation by Tanzawa and Tanaka defines the estimated expected efficiency as follows[4].

$$\eta = \frac{Vout}{(N+1) * Vin} \quad (5)$$

The measured voltage was substituted into the equation and plotted in Figure 4. Figure 5 corresponds closely with the simulated results. As both the stage number and the input voltage increase, the efficiency also increases along the same values predicted by PSpice. From the data above, it can be inferred that the Dickson Charge pump itself is operating with decent efficiency. The power inefficiency lies in the 555 timer and inverter circuit. According to the data sheets, the 555 timer will consume a few milliamps and requires a supply voltage of approximately 2.5 volts. This circuit may be the dominant reason why the efficiency only increases with the increased stage number. Each additional stage offers more resistance and, due to the high resistivity of the 555 timer, the resistive loads are not matched properly yielding even lower power efficiencies. In essence, the efficiency should increase with additional stages until the circuit resistance matches the resistance of the timer circuit. Also, the 555 timer maintains optimal performance at around 10 volts. This may also explain why the circuit performed better with higher voltages.

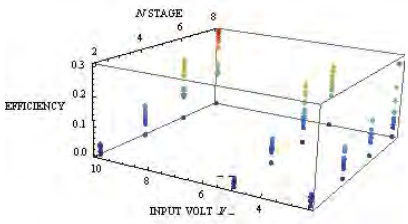

Figure 4. Actual efficiency as a function of input voltage and stage number

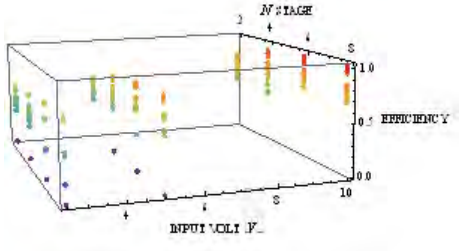

Figure 5. Estimated efficiency as a function of input voltage and stage number

Therefore, a solar cell could never power this timer circuit. Before any comparison with solar cells can be made, the power consumption of the timer must be minimized. There are a few possible solutions. An effort will be made to use a more efficient timer. A 7555 timer consumes current on the order of micro amps and has a lower supply voltage. Recent measurements show a dramatic increase in efficiency when implementing the 7555 timer. Minimum efficiencies of 38% were achieved at two volts input while maximum efficiencies of 53% were achieved at 15 volts input. These measurements were taken with a ten stage charge pump. The two stage measurements demonstrated very poor efficiencies, as predicted by the previous simulations and measurements. This may suggest that mismatched impedances do not account for the unexpected increasing efficiencies with increasing stage numbers. It appears that the eight stage charge pump is simply more efficient than the two stage. At what stage number the efficiency eventually decreases is unknown. Further research is required but will probably show that the required stage number is dependent on the input voltage. Other improvements may be to increase the operating frequency. The initial circuits proposed in PSpice may eventually be tested once improvements have been made. An organic solar cell only produces a few micro amps and about half a volt, but any improvement in this Dickson Charge Pump may allow for an optimized balance in sacrificing a little power efficiency by stacking solar cells in series for higher voltages to power this charge pump.

Conclusion

The timer circuit is providing a far greater power burden and resistive load than any organic solar cell can operate. The timer may also

be offsetting anticipated results whereby the efficiency unexpectedly increased with increased stage number. However, the information is useful in that it implies more than 2 stages of the charge pump may be used to obtain maximum efficiency. The timer circuit will be improved before anticipated comparisons to solar arrays are made. Further testing will acquire the appropriate stage number required in a delicate and optimal balance of voltage gain and power loss.

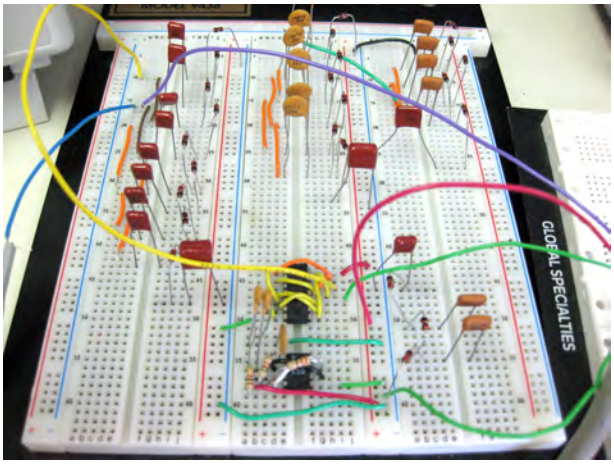

Figure 6. Four Dickson Charge Pumps and the timer circuit on a breadboard used in testing.

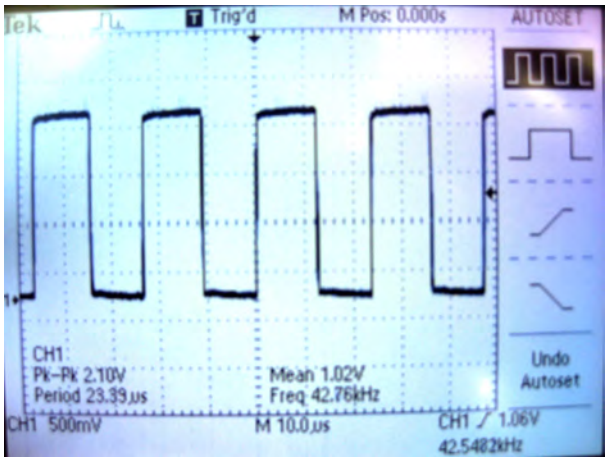

Figure 7. The square wave voltage produced by the timer circuit as viewed with an oscilloscope.

Acknowledgements

This material is based upon work supported by the STC Program of the National Science Foundation No. DMR 0120967

Joey Duvall, PhD. Student, Electrical Engineering, Georgia Institute of Technology

Lorne Liechty, PhD. Student, Electrical Engineering, Georgia Institute of Technology

Ruoju Liu, Masters Student, Electrical Engineering, Georgia Institute of Technology

Ryan Pirkl, PhD. Student, Electrical Engineering, Georgia Institute of Technology

References

1. Herald, Hoppe, and Niyazi S. Sariciftci. "Organic Solar Cells: an Overview." Journal of Materials Research 19 (2004): 1924-1945.
2. Ahmad, M. R., T. R. McNutt, H. A. Mantooth, and M. M. Mojarradi. "A Technique to Increase the Efficiency of High-Voltage Charge Pumps." IEEE Transactions on Circuits and Systems 53 (2006): 364-368.
3. Dickson, John F. "On-Chip High-Voltage Generation in MNOS Integrated Circuits Using an Improved Voltage Multiplier Technique." IEEE Journal of Solid-State Circuits 11 (1976): 374-378.
4. Tanzawa, Toru, and Tomoharu Tanaka. "A Dynamic Analysis of the Dickson Chrge Pump Circuit." IEEE Journal of Solid-State 32.8 (1997): 1231-1240.

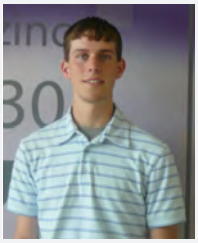

DANIEL LUM is a physics student attending Louisiana State University. He intends on pursuing a Ph.D. along with research in quantum optics.

Fabrication and Characterization of Bulk Heterojunctions Based on Low Band Gap Polymers

ARIEL S. MARSHALL, University of Central Arkansas
Joseph Perry, Philseok Kim, Department of Chemistry and Biochemistry, Georgia Institute of Technology

Introduction

Photovoltaic (PV) technology is rapidly growing and promises to be a new advancement towards alternative energy. The organic materials used in PV devices offer benefits such as flexibility, tunable optical properties, low cost and processability that are not seen in silicon based solar cells used today. Devices consisting of donor and acceptor materials mimic natural photosynthetic reactions by a photoinduced electron transfer from donor to acceptor material. This charge transfer can be turned into current therefore converting light to electricity.

Donor materials in these high efficiency devices are often conjugated polymers. These polymers are very desirable semiconducting materials because of their absorption properties and their ability to be deposited on substrates at low costs. Their quasi-infinite π system results in material with great directional conductivity. The highest efficiencies in organic PV cells have been obtained through bulk heterojunction devices (BHJs) containing poly(3-hexylthiophene), P3HT and [6,6]-phenyl-C_{61} butyric acid methyl ester, PCBM.[1] By increasing the interfacial area between donor and acceptor material, BHJs allow for intermixed layers and easier charge transport.

Polyacetylene (PA), the simplest conjugated polymer, is often used as a backbone in donor materials.

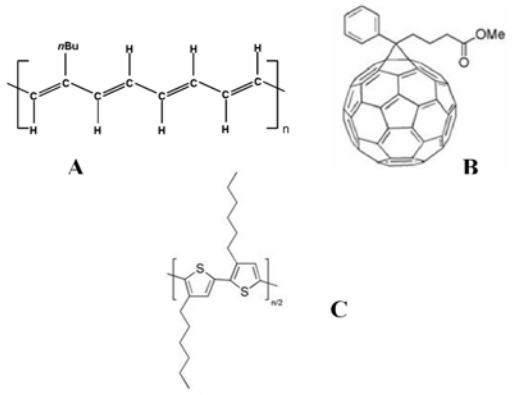

Figure 1. Molecular structures of PA, polyacetylene (A), PCBM (B), and P3HT (C).

Polyacetylene possesses a low band gap making it an ideal material for light-harvesting. However, PA is very unstable under ambient conditions. Its highly conjugated chain leads to easy oxidation of the material. Also, PA produced using the Shirakawa method is generally non processible due to its insolubility after polymerization. This is a very undesirable attribute for film processing.

A potential solution is to deviate from the standard Shirakawa method used to make this polymer and employ ring opening metathesis polymerization (ROMP). By starting the film fabrication process with a liquid monomer and using ROMP method as the polymerization method, a processible film can be made from PA.

The objective of this project is to fabricate composite films based on polyacetylene and PCBM and to test whether photogeneration of charge carriers occurs in such materials. Transient absorption measurements were performed on both the PA:PCBM blends as well as P3HT:PCBM as a standard comparison for the measurements.

Experimental

All solvents were ACS grade and used after degassing with nitrogen purging. UV-vis absorption spectra were recorded using a Shimadzu UV-Vis-NIR scanning spectrometer (UV-3101PC) in a dual beam geometry.

Scheme 1

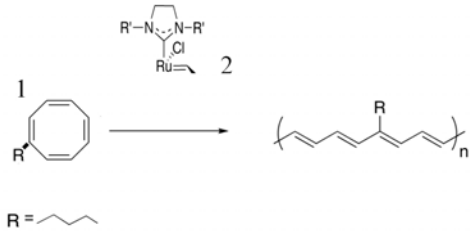

2.1. Preparation of PA:PCBM blend

The structures of the monomer and catalyst used are shown in Scheme 1. Mono-substituted *n*-butylcyclooctatetraene (1) was prepared using a method reported previously.[2] Polymerization of *n*-butylcyclo octatetraene via the ROMP method was carried out under ambient conditions using a ruthenium-based 2nd generation Grubbs catalyst (2). The ROMP reaction was performed by dissolving the initiator (0.3 mg) and PCBM (2.6 mg) in a minimal amount of degassed dichloromethane (100 μL).

2.2. Preparation of P3HT:PCBM Blend

Thin films of P3HT:PCBM were prepared by dissolving PCBM (Aldrich, >99.5%) and regioregular P3HT (Rieke Metals) in chlorobenzene as described in in the literature[3]. The mixture was then filtered through a 0.2 μm Teflon syringe filter. A blend combination of 0.8:1 by weight (PCBM:P3HT) was studied.

2.3. P3HT:PCBM and PA:PCBM Film Fabrication

Films of both PA:PCBM and P3HT:PCBM were prepared on glass substrates. The substrates were thoroughly cleaned in an ultrasonic

bath with soap, DI water, and ethanol for 30 minutes and dried in a dry nitrogen stream. The substrates were then exposed to cold air plasma for 3 minutes at 750 W power and 3 SCFH (standard cubic feet per hour; 1 cubic feet = 28.3 L) to increase the hydrophilic properties of the substrate.

The P3HT:PCBM layer was deposited on the substrates via spin-coating at 1000 rpm for 60 seconds giving an approximated thickness of 260 nm. The coated substrates were then soft baked at 140°C for 10 minutes and quenched to room temperature on an ice-cooled metal block.

The PA:PCBM blend was deposited on the glass substrates via drop casting and spin-coating at 1000 rpm for 60 seconds. After the PA:PCBM solution had been deposited, the films were stored in an argon-filled glove box. Thicknesses of the films were measured by using a contact profilometer (Dektak 6M, Veeco, see Table 1)

2.4. Transient Absorption Measurements

Ultra-fast transient absorption measurements were performed using a second harmonic (532 nm) of a nanosecond Q-switched Nd:YAG laser (Spectra-Physics, Newport Co., Quanta-Ray Pro 250-10) as the pump beam. The laser pulse energy was kept at 2 mJ. A 250 W tungsten-halogen lamp controlled by 300W radiometric power supply (model 69931, Oriel, Newport Co.) was used as the probe beam.

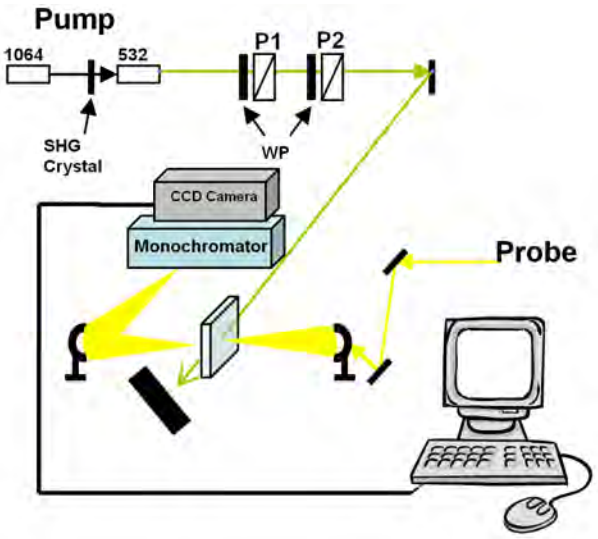

Figure 2. A schematic of pump probe experiment

Results and Disscussion

3.1. P3HT:PCBM Transient Absorption Measurements

Figure 3a shows the normalized UV-Vis absorption spectrum of 1:0.8 (wt./wt.) PCBM:P3HT thin film. Transient absorption (TA) measurements were performed on the samples (see Figure 3b).

The TA spectra display a large peak at 532 nm due to the scattered pump beam. The second largest peak at ~560 nm is accredited to a Stokes line that may be due to the residual solvent. The other broader peaks ranged over 540-650 nm are possibly due to the depletion of the absorption of P3HT. No noticeable change due to electronic transitions of P3HT:PCBM was observed. Charge carrier photogeneration and recombination of P3HT occur at an extremely fast time scale. With a reported charge carrier lifetime of ~1.5 ns4, the transition occurred at a time scale faster than our measuring system. Also, the recombination of the blend was too weak to be seen by this method.

A

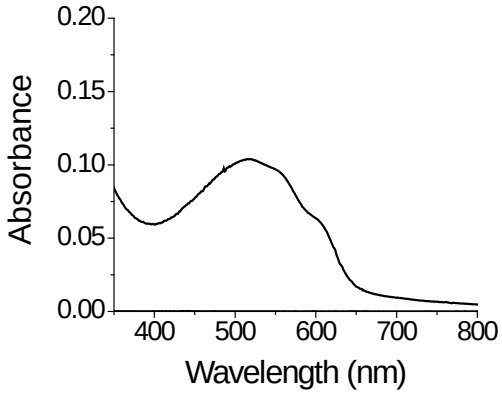

B

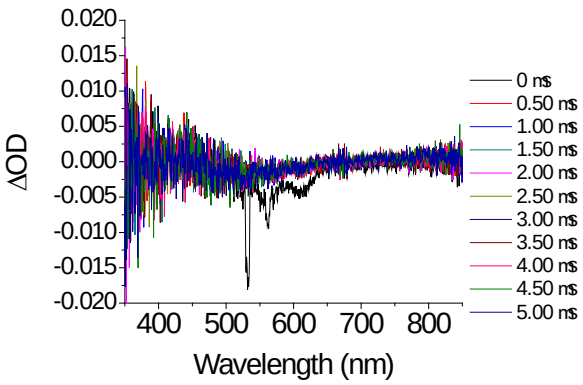

Figure 3. Normalized UV-Vis absorption spectrum (a) and transient absorption spectra using pump probe method (b) of 0.8:1 PCBM:P3HT thin film.

3.2. Marcus Theory Calculations

Marcus theory calculations were performed on PCOT to calculate its rate of electron transfer using the following equation.

$$k_{et} = \left(\frac{4\pi^2}{h}\right) t^2 (4\pi\lambda RT)^{-1/2} \exp\left(\frac{-\lambda}{4RT}\right)$$

Where k_{et} is the rate of electron transfer and λ is the internal reorganization term.[5] The electron transfer rate of PCOT was calculated to be 2 x 10^{11} s^{-1} which is slightly slower than the decay rate of the singlet excited state of polyacetylene (10^{12} s^{-1})[6] suggesting that photogeneration in this system is possible.

3.3. PA:PCBM Transient Absorption Measurements

Thickness measurements were collected for PA:PCBM samples (Table 1). Both deposition methods produced films with non-uniform thicknesses. Films showed large scattering and uneven surface due to clustered PCBM.

Sample	Speed (rpm)	Thickness (nm)
1	1000	380
2	DC	4390
3	DC	15,760

Table 1. Thickness measurements of both spin cast and drop cast (DC) PA: PCBM samples.

UV-vis data was collected from the PA:PCBM film and pure PA showing a broad absorption band over visible and near-infrared region with a maximum absorbance at ~500 nm.

The optical density of the PA:PCBM films were too large for TA measurements to be performed.

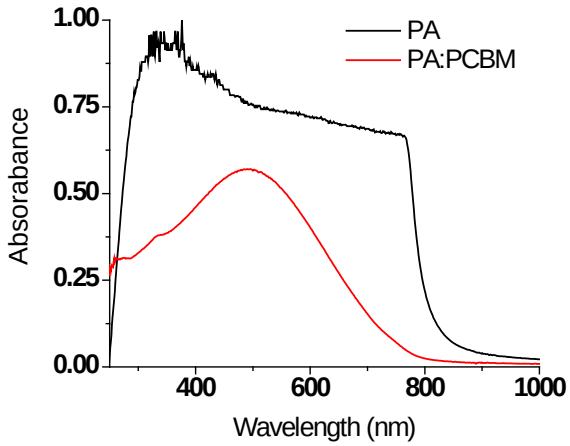

Figure 4. Normalized UV-Vis absorption spectra of thin films of PA and PA:PCBM spin coated on a glass slide.

Conclusions and Future Work

Both P3HT:PCBM and PA:PCBM films were prepared and characterized by UV-vis absorption. PA:PCBM films showed a large absorption extending from the visible to the near-infrared region, but the optical density of the films were too large for TA measurements to be performed. Also, the PA:PCBM films showed a large accumulation of PCBM clusters which calls for different preparation methods, such as ultrasonic separation of PCBM. Systematic variations of thermal treatment of PA:PCBM system would reveal the phase behavior of this mixture and lead to the optimized condition.

TA measurements were performed on P3HT:PCBM films, but due to the fast decay of the blend, no electron transitions or recombination was observed.

Acknowledgements

This material is based upon work supported by the STC Program of the National Science Foundation No. DMR 0120967. I would like to acknowledge Georgia Institute of Technology: Philseok Kim (mentor), Dr. Joseph W. Perry (advisor), San-Hui Chi, Dr. Matthew Sartin, and Matteo Cozzuol, University of Central Arkansas: Dr. P. J. Desrochers (advisor).

References

1. Coakley, Kevin M.; McGehee, M. D. Chem. Mater. 2004, 16, 4533.
2. J.T Miller, C.W. DeKock, M.A. Brault, J. Org. Chem. 1979, 44, 3508.
3. M. Reyes-Reyes, K. Kim, D.L. Carroll. Appl. Phys. Lett. 87, 083506 (2005)
4. Ceasare Soci; I. Hwang; C. Yang; D. Moses; Z. Zhu; D, Waller; R. Gaudiana; C. J. Brabec; and A. J. Heeger. SPIE. 2006, 6334, 63320D-1-63340-D-4.
5. J.L. Bredas; D. Beljonne; J. Cornil; J. P. Calbert; Z. Shuai; and R. Silbey. Synthetic Metals, 125, (2002), 107-116
6. L. Rothberg; T. M. Jedju; S. Etemad; and G. L. Baker. J. of Quant. Electronics. 24, 311-314 (1988).

ARIEL MARSHALL is from Benton, AR. She is a recent graduate from the University of Central Arkansas (Conway, AR) and received her B.S. in Chemistry (ACS certified). She has since decided to continue her education to graduate school at the Georgia Institute of Technology with a focus on chemistry.

Attenuating Conductivity in Electro-optic Devices via Sol Gel Deposition of TiO_2

JOHN R. MILTON

Ben Olbricht, Philip Sullivan, Larry Dalton, Chemistry Department, University of Washington

Introduction

Electro-optic (EO) activity is achieved through alignment of dipolar organic chromophores. A process known as poling is used to order the molecules. Poling involves heating up the material to its glass transition temperature, at which the molecules can rotate and, thus, align to an applied electric field. Conductivity limits the magnitude of the poling field and can also cause electro-chemical decomposition both of which degrade EO activity.

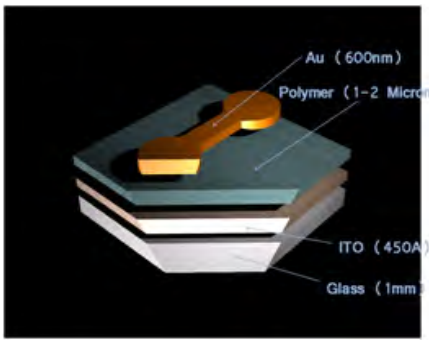

Figure 1. Basic slab waveguide model

The model above shows the layers of a basic slab waveguide. The device poles by applying a voltage across the gold (Au) and the Indium Tin Oxide (ITO), ergo; there is a poling field across the polymer.

Poling is the process by which molecular dipoles align in the presence of an external or "poling" electrical field. In poling, an electric field is applied to a polymer/chromophore composite material while the polymer is heated up to the glass transitional phase allowing for chromophore reorientation. After alignment the polymer is cooled to lock in chromophore order rendering the EO material active.

Experimental

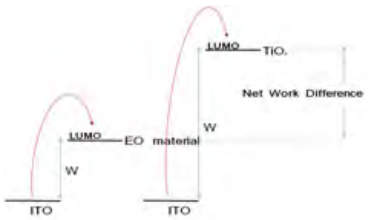

Figure 2. Work function comparison of EO to TiO_2. Increase resistivity by spin coating the ITO glass slide with a thin layer of TiO_2.

There is a theory to mitigate the conductivity EO devices and this process requires the addition of buffer layers. One mechanism of an EO material is charge injection. By depositing a buffer layer, such as Titanium dioxide TiO_2, the barrier for charge injection can be increased due to the high electronic energy levels relative to the electrodes. Therefore, it can be predicted that TiO_2 buffer layers reduce conduction in the device, yielding improved poling and thus higher electro-optic activity.

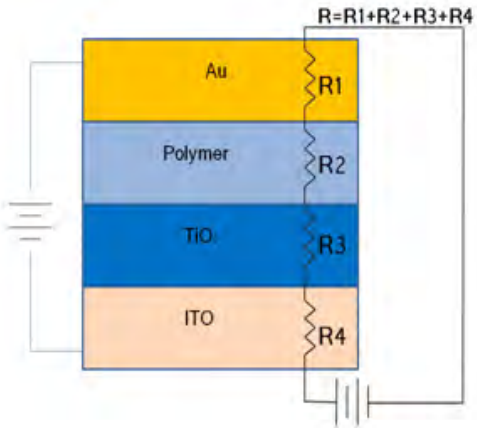

Figure 3. Modulator resistances

Each layer of the device can be seen as resistors set in a series with each other. The TiO_2 will have the largest resistance and it will limit the amount of holes injected into the polymer from the ITO, thus, strengthening the poling field and preventing electro-chemical decomposition of the chromophore.

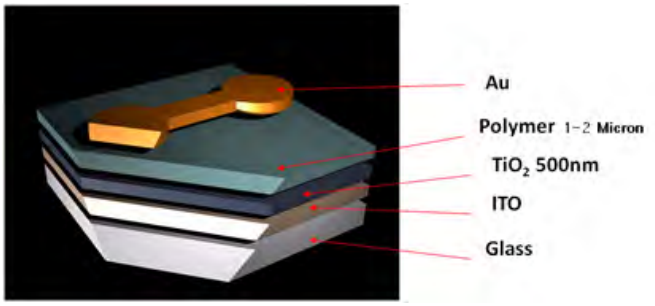

Figure 4. Blocking layer model

Sol gel method TiO_2 spin deposition was used on glass slides; in theory, sol gel can generate high quality TiO_2 thin films. The quality of the TiO_2 film is greatly dependent on how fast the sol gel nucleates. Sol gel films deposited according to the method outlined in the literature resulted in nucleation. Doubling the quantity of HCl resulted in high optical quality films. The dielectric constant of the TiO_2 thin film is dependent on the annealing temperature, and is highest at ~700 degrees Celsius. However, the temperature that the TiO_2 was subjected to was 450 degrees Celsius—the maximum sustained temperature that the glass substrate could withstand. Thus, increasing the dielectric constant compared to films prior to annealing[1]. With a high dielectric constant, the TiO_2 film has a high capacitance meaning that it can store large amounts of charge and maintain the poling field strength.

TiO_2 capacitance is important because the device is layered as so; Indium Tin Oxide (ITO)/TiO_2/polymer/Au. With ITO directly in contact with the polymer, sending current through the device will make a large amount of electrons move through the chromophores which, can cause electro-chemical breakdown or catastrophic device failure. By introducing a TiO_2 layer, the device can take substantially more voltage high conduction via charge injection. The decrease of current implies that you can apply a stronger field across your polymer, thus, giving a higher r_{33} from the polymer.

Results

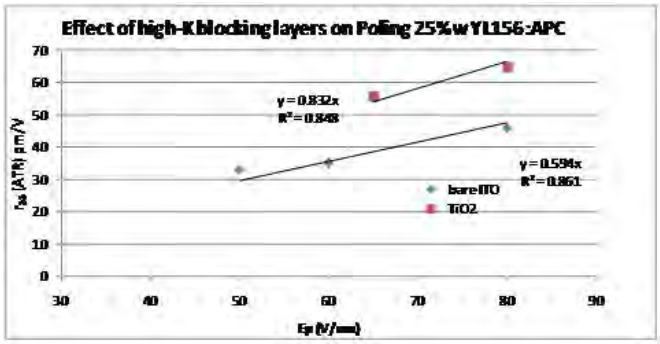

Graph 1. Effect of high-k blocking layers on Poling 25%w YL156:APC

This data shows that a layer of TiO_2 between the ITO and the polymer, a higher r_{33} is achieved relative to bare ITO. The graph above shows a stronger field across the polymer (x-axis), the increased potential current input without chromophore break down (slope).

Discussion

Attenuating conductivity in electro-optic (EO) materials represents an important advance towards high-performance devices. It can be shown that conductivity has number of disadvantages in EO devices. For example, conductivity can limit the magnitude of the poling field applied to establish chromophore order, and can limit the reproducibility of EO activity. Through sol gel deposition of high transparency, low roughness and high optical quality TiO_2 films, an increase of as much as 40% in electro-optic activity can be realized.

Acknowledgments

A special thanks to the NSF, University of Washington, Larry Dalton Group, Center of Materials and Devices for Information Technology (CMDITR) for supporting my research. Thanks to my mentor Benjamin C. Olbricht with assistance from Philip A. Sullivan, Antao Chen, and Larry Dalton. Other thanks go out to my "Hooked on Photonics" program organizers Marya Dominik and Jeanne Small.

References

1. M.J. Alam, D.C. Cameron, J. Sol-Gel Sci. & Tech. 25, 137 (2002).

JOHN R. MILTON

A Spectroscopic Analysis of a Candle Flame Light Source

ANGELA N. PARKER, Norfolk State University
Dr. Carl Maes, University of Arizona

Objective

An analysis was conducted on the familiar blackbody emission spectrum of a candle flame. Blackbody distribution emits at all wavelengths in the electromagnetic spectrum. However, this particular blackbody distribution contains an unknown doublet that peaks approximately at 754nm and 757nm. The types of candles that emit this doublet are paraffin, olive oil, and kerosene. The objective of this particular research is to find out exactly what atomic species is emitting brightly in these particular flame sources that may be causing this anonymous doublet to appear. Figure 1 is a spectroscopic reading of a candle flame.

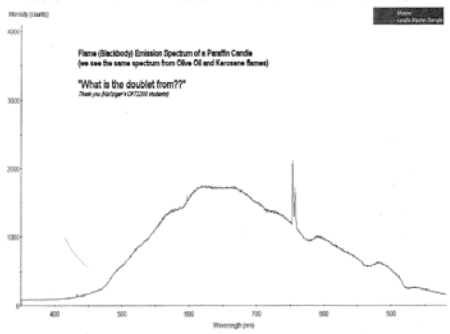

Figure 1. Spectrometer reading of a candle flame

There are many possibilities as to why the doublet appears, simply because so many factors are involved in the process of a burning candle. The properties of the candle include many materials that react when heated. The containments of a candle play an important role as to why this doublet is being emitted.

Background Information

Before actually starting the experimental phase of this research, one must be knowledgeable of a few things. The electromagnetic spectrum is a huge factor in the degree of this research. The EM spectrum can simply be defined as the range of wavelengths in which light is emitted. The spectrometer, which is an instrument that determines the intensity of various wavelengths in a spectrum of light, utilizes the EM spectrum greatly. It would also be very significant to be aware of what blackbody emission is. Blackbody emission emits radiation at all wavelengths in the spectrum. One of the most well known things to emit a blackbody spectrum would be the sun. An example of blackbody radiation is illustrated in Figure 2.

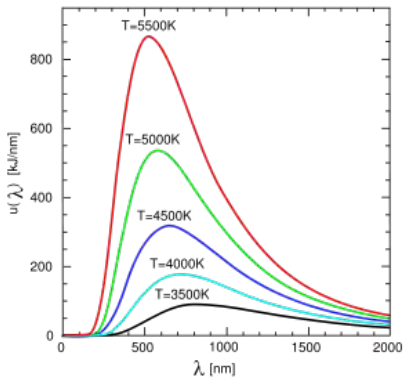

Figure 2. General blackbody emission spectrum

It was Plank's Law that first described blackbody radiation. It states that the spectral radiance of electromagnetic radiation at all wavelengths from a blackbody at temperature T. as a function of frequency ν.[2] Planck's law is written as:

$$I(\nu, T) = \frac{2h\nu^3}{c^2} \frac{1}{e^{\frac{h\nu}{kT}} - 1}.$$

Wien's displacement law is a law that states that there is an inverse relationship between the wavelength of the peak of the emission of a blackbody and its temperature.[3]

$$\lambda_{max} = b / T$$

λ_{max} is the peak wavelength in meters

T is the temperature of the blackbody in Kelvins

b is a constant: 2.89 x 10^6 nm K

In this case the T is the temperature of the candle flame (1,930 K), which would then be multiplied by the λ_{max} that would then produce the constant b.

Experimental/Research Methods

Before even analyzing the candle flame, various other light sources were first tested. Using the Ocean Optics Spectroscopy software and a spectrometer, a range of other light sources were observed. A spectrometer simply determines the intensity of various wavelengths in a spectrum of light. Some of the light sources observed include the following: a florescent light bulb, a helium-neon laser, and a UV sodium light. After observing these light sources and becoming familiar with the functions of the computer software involved, the candle flame was then brought into action.

Figure 3. The candle and spectrometer

It was identified that the candle flame would emit a blackbody distribution containing an unknown doublet. Therefore, many other flame sources were then observed, merely to see if there were any similarities to the doublet emitted from the candle flame. Many of the flame sources observed included: a propane torch, an ignited Q-tip and a match stick. Preceding these observations many literature searches were to be done to determine whether there were any other materials (not necessarily light sources) that also contain a doublet. After much searching, it was found that alkali metals also emit a doublet. This led to many intriguing experiments using alkali metals. However, since there was really no possible way to find a pure alkali metal source that was easy to obtain, many sources that contained a large amount of an alkali metal seemed to be the next best thing to acquire. Sodium and potassium are two alkali metals that are commonly found in foods. Some of the test subjects used included salt (NaCl), potassium chloride (KCl), and a banana. To give energy to these materials, they were burned in a propane torch. Without being burned these different materials would only be emitting infrared radiation at room temperature. Room temperature, which is about 298K, emits at about 10 microns and obviously cannot be seen by the naked eye.

When the materials containing sodium were burned, they emitted a peak at around 587nm and a small doublet similar to the one seen in the candle flame. On the other hand, the potassium emitted a doublet at the same intensity and wavelength as the candle flame did. Although it was assumed that the goal of finding out what was causing the doublet was accomplished, the data first had to be compared to a justifiable source.

Calibrations

All of the results found in this research could not be considered valid until the accuracy of the spectrometer could be confirmed through a calibration using a legitimate reference. All the calculated data collected during experimentation was compared to the National Institute of Standards and Technology (NIST) website. The measured data surprisingly did not match up with the theoretical data on the NIST website. Therefore a systematic approach was taken to hopefully calibrate the spectrometer readings that were being used to attain the measured data. Four other light sources were then tested with the spectrometer. These sources included neon, helium, krypton, and argon lights. These particular lights were used because they peak at many wavelengths throughout the spectrum. This would allow many comparisons of theoretical lines and measured lines.

The theoretical lines and calculated lines were matched up as closely as possible. Measured strong lines were matched with similar strong lines of the theoretical data. The same was done with the persistent measured lines and theoretical lines. There were very few lines that were exactly the same. Scatter plots were constructed that consisted of the theoretical data from the NIST website versus the difference in the theoretical data and the measured data. Figure 4 is a scatter plot diagram of helium.

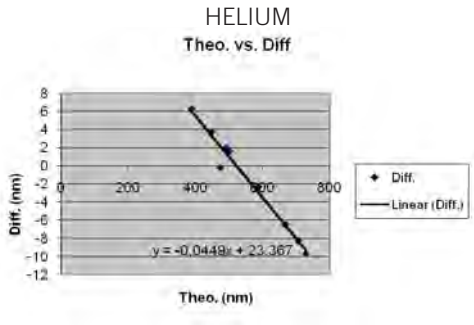

Figure 4. Theoretical data versus the difference in the measured data and the theoretical data.

From there the slope of the best fit line was found. The best fit line basically illustrates the linear relationship between the theoretical data and the difference in the theoretical data and the measured data. The sodium spectra line value and the potassium spectra line values were then substituted into the value of x in the slope equation. When placing that value in for x, y would then equal the approximate difference in the measured lines of sodium and potassium compared to the theoretical values of sodium and potassium.

Results/Conclusion

When the calibrations were completed it was concluded the ocean optics spectrometer was definitely inaccurate as far as the values of the sodium and potassium lines are concerned. The sodium lines were off by about 2nm and the potassium lines were off by approximately 12nm.

The calibration data shows that at the wavelength of potassium, the spectrometer measure reads the theoretical wavelengths of 766.5 and 770 nm to be displayed as 754 and 758 which agrees greatly with the actual measured wavelengths of 754 and 757 nm. So, using the calibration curve the ocean optics spectrometer could actually be quite accurate. Therefore, it is concluded that potassium is the atomic species that is causing the doublet to appear.

As stated previously, so many factors are involved in the process of a burning candle. All candle wicks are treated with a range of flame resistant solutions in a procedure known as mordanting. Mordants include various salts including potassium. Without mordanting the wick would be destroyed by the flames and the flow of the melted wax to the flames would cease. This is one logical explanation for the presence of potassium in the emission of a candle flame.

Acknowledgements

This work has been made possible by Norfolk State University and the Science and Technology Center (STC) on Materials and Devices for Information Technology Research (MDITR), No. DMR 0120967. I would like to thank Dr. Arlene Maclin of NSU and Dr. Carl Maes of the U of A, who have both given me this opportunity to succeed as a student as well as a researcher.

References

1. National Institute of Standards and Technology (NIST). "Physics Laboratory: Physical Reference Data." http://physics.nist.gov/PhysRefData/Handbook/index.html (July 2008)
2. Principles of Lasers (4th ed.). (1998). New York, NY: Plenum Press.
3. University Physics (11th ed.). (2004). San Francisco, CA: Pearson Education, Inc.

ANGELA N. PARKER is a junior optical engineering student at Norfolk State University. Upon graduation in 2010, she intends on pursuing a Masters in optical communications.

Effect of Salts on the Drop Size Dependence of the Water Contact Angle

KIM REISHUS, Taylor University
Marcel Lucas, Elisa Riedo, School of Physics, Georgia Institute of Technology

Introduction

Scientists are researching many natural surfaces in order to mimic their unusual surface properties[1]. For example, Gecko toes have thousands of setae on their toes, making them a strong adhesive surface, and allowing the Geckos to climb up smooth, vertical surfaces with ease. Researchers have synthesized the setae in order to develop a strong adhesive that has applications in engineering.[2] Also, at Georgia Tech a coating has been developed imitating the Lotus leaf that makes any surface it covers superhydrophobic.[3] It was determined that superhydrophobicity was mainly caused by the surface chemistry and the multiscale surface roughnesses.[4]

Measuring the contact angle is a common method used to characterize the wettability of a surface. The contact angle is geometrically defined as the angle formed by a liquid at the three-phase boundary where liquid, solid and gas meet (Figure 1). Surfaces are called hydrophobic when the water contact angle is higher than 90°, and hydrophilic when the water contact angle is lower than 90°.[5] There are many types of contact angle: advancing (the dynamic angle formed as the droplet advances across a dry surface), receding (the dynamic angle formed as a liquid recedes across a previously wetted surface), and the as-placed (the static angle formed after a droplet placed on the surface reaches equilibrium).[6]

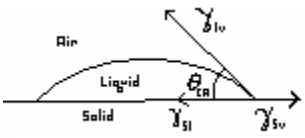

Figure 1. The contact angle and surface tensions.

Background Information

The drop size effect on the contact angle has been a matter of controversy for 40 years. Opposite trends (increasing and decreasing contact angle with increasing drop size) have been observed in various gas/liquid/solid systems.[7-15] It was found through experiments in near free-fall conditions that there was a difference of about 5° between the contact angle found on the ground and the contact angle found in free-fall conditions.[16] The contact angle is affected by surface roughness, microscopic heterogeneity of the surface, drop size effect, molecular reorientation and formation at the surface, and the size of the liquid molecules[6].

For the larger droplets, the size dependence was attributed to gravity[17]. Another model, based on the modified Young's equation, introduced the effect of line tension[11]:

$$\gamma_{lv}\cos\theta = \gamma_{sv} - \gamma_{sl} - \frac{\sigma}{R}, \text{ where } \gamma_{lv}, \ \gamma_{sv}, \ \gamma_{sl},$$

σ, θ and R are the interface tensions (the excess free energy per unit area due to the formation of an interface) of the liquid/vapor, solid/vapor and solid/liquid interfaces (Figure 1), the line tension, the contact angle and the radius of the droplet, respectively. Line tension can be defined as the excess free energy per unit length due to the presence of the three-phase contact. It was also defined as the force operating in the three phase contact line to minimize its length (or three-phase interface area).[13] Previous attempts to determine the line tension yielded values spread over several orders of magnitude and even opposite signs. The scattered data was mostly explained by the fact that the line tension was derived from models that did not take into account the effect of surface roughness and heterogeneity.[7-10] Indeed, experiments done on different surfaces have produced opposite contact angle trends.[18] Its physical meaning is still debated and is related to the molecular interactions between the three phases near the contact line that affect the interface tensions[13]. Also, line tension is not only affected by the surface chemistry, but also by the liquid and vapor chemistry[9].

Recent experiments have been conducted in order to determine what effect the presence of salts or nanoparticles in the liquid have on the contact angle. It was observed that the addition of sodium chloride increased the contact angle.[5] It was also found that the contact angle was affected by the nanoparticle concentration and size.[19]

Therefore, to study the effect of liquid chemistry on the drop size dependence, the as-placed and receding contact angles of water are compared to the as-placed and receding contact angles of a sodium chloride solution and hydrochloric acid on surfaces with various wettabilities.

Methods

The as-placed and receding contact angles were measured for water, saturated sodium chloride (brine), and hydrochloric acid (pH 2) liquids. Droplets were deposited on two hydrophilic surfaces (glass and aluminum), and a hydrophobic surface (wax), with contact angle values ranging from 30-110°. All measurements and pictures were collected using the SEO Pheonix 150 and the Image XP software. The as-placed contact angle was measured by forming a pendant droplet and raising the stage up to the droplet, gently pulling

the droplet onto the surface, waiting 15 or 30 seconds, depending on whether or not the surface was hydrophobic or hydrophilic, respectively, and taking a picture. The droplet range covered 0.5 - 10 mm radius. The receding contact angle was measured by letting an as-placed droplet of 3µL evaporate over time, with pictures taken every 15 seconds. The contact angle and radius were analyzed by using the SPIP (Scanning Probe Image Processor) software and the contact angle recorded was the average between the contact angles on either side of the droplet. All measurements were conducted in air at room temperature.

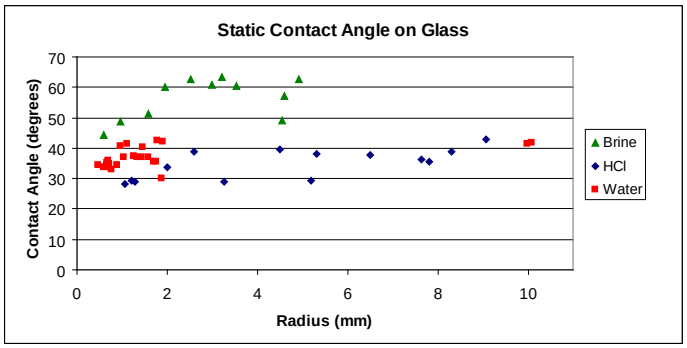

Figure 2. Static contact angle as a function of droplet base radius on glass using saturated NaCl, ~0.1 molar HCl, and DI water.

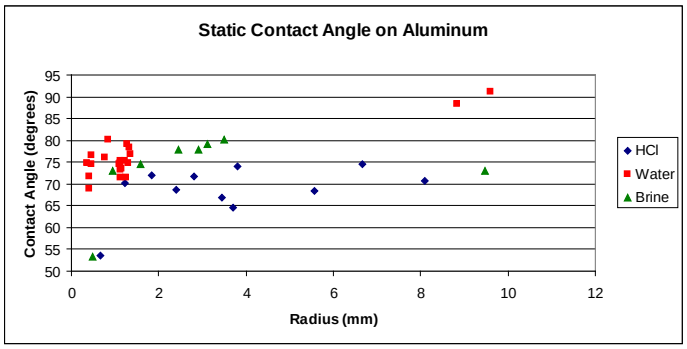

Figure 3. Static contact angle as a function of droplet base radius on aluminum using saturated NaCl, ~0.1 molar HCl, and DI water.

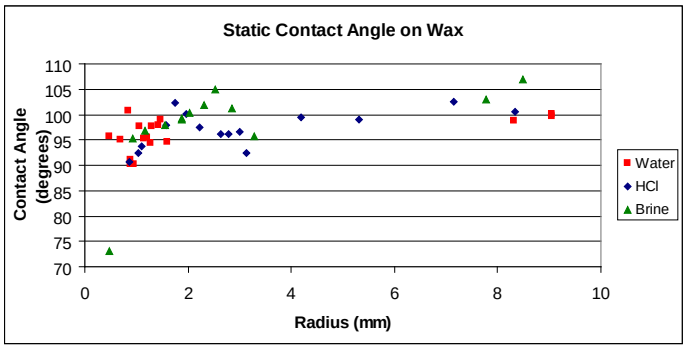

Figure 4. Static contact angle as a function of droplet base radius on wax using saturated NaCl, ~0.1 molar HCl, and DI water.

There was no significant drop size dependence observed over the radius range 0.5 mm to 10 mm (Figures 2-4). The presence of the saturated salt solution resulted in an increase of about 10° to 20° above the water and hydrochloric acid contact angles on glass, the most hydrophilic surface (Figure 2). The sodium chloride solution had no significant effect on aluminum or wax (Figs. 3-4). This was expected as it had been previously shown that on hydrophobic surfaces, the salt concentration did not significantly change the contact angle, while on hydrophilic surfaces, the contact angle significantly increases as the salt concentration increases, from 40° to 75°.[5] The data spread is attributed to the varying surface heterogeneity. It has been shown that experiments done on rough, heterogeneous surfaces result in trends showing the contact angle increasing with increasing radius while experiments done on smooth, homogeneous surfaces result in the opposite trend[18].

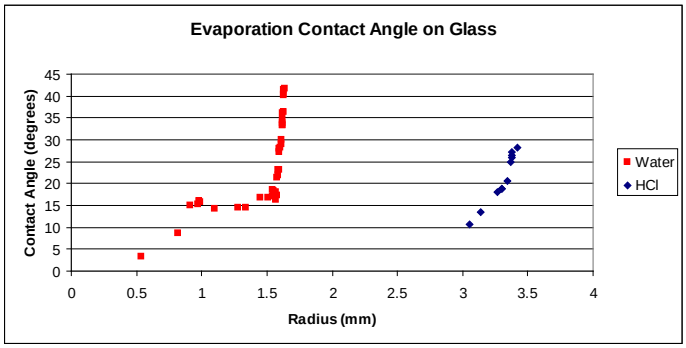

Figure 5. Contact angle as a function of droplet base radius during the evaporation of ~0.1 molar HCl and DI water on glass.

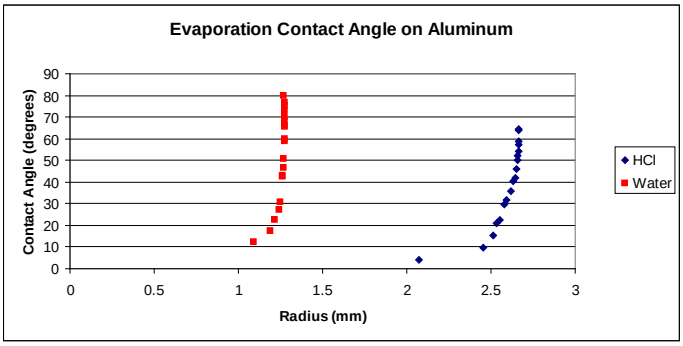

Figure 6. Contact angle as a function of droplet base radius during the evaporation of ~0.1 molar HCl and DI water on aluminum.

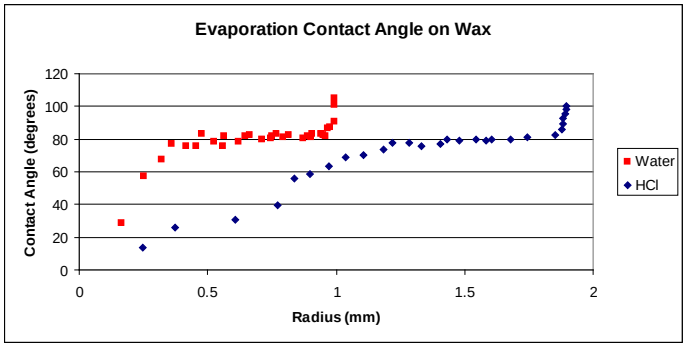

Figure 7. Contact angle as a function of droplet base radius during the evaporation of ~0.1 molar HCl and DI water on wax.

The evaporation method avoids the disadvantage of large variations in surface heterogeneity and provides a way to measure the receding CA as a function of drop size and time (Figures 5-7). The receding contact angle was not measured for the brine solution, since the droplet was deformed by the salt recrystallization. The data between the two methods are not directly comparable by base radius measurements, due to the different surface wettabilities, but if the droplet volumes are analyzed, the water and hydrochloric acid results from the two methods would be comparable. Droplet volume analysis remains a technical challenge, since it requires elaborate video analysis software and the assumption must be made that the droplet is axisymmetrical.[20] As the hydrochloric acid droplets evaporate the concentration of the HCl increases as the volume decreases, so the receding contact angle is not only a function of size, but also of HCl concentration. Since the receding contact angle value can be influenced by the volume decrease rate,[6] the initial volume of the as-placed droplet was kept at 3μL, in order to have comparable evaporation rates for all droplets.

Discussion

For both the wax and the glass surfaces, there were two distinct evaporation phases (Figures 5-6): first, the contact angle decreases sharply while the droplet base radius remains constant. Once the contact angle reaches a critical value, the radius also decreases with the contact angle until the droplet is completely evaporated. The contact angle is then comparable to the receding contact angle measured using the inclined plane method[6]. As for the hydrophobic surface, the contact angle initially drops with only a small radius variation and then remains constant, while the radius decreases continuously down to a critical value where the contact value also decreases with the radius (Figure 7). These two different behaviors are consistent with previous studies of volatile liquid drops on low-surface-tension solids: for initial contact angles lower than 90°, the evaporation follows the constant contact-area mode; and for initial contact angles higher than 90°, the evaporation follows the constant contact-angle mode.[21]

For an ideally flat solid surface, the three-phase contact line should recede continuously.[6] The droplet pinning on hydrophilic surfaces is characteristic of a strong adhesion of the water droplet. This pinning can be accentuated by the surface roughness and chemical heterogeneity. After the initial contact angle drop, the radius starts to decrease only when the excess free energy generated by the three interfaces exceeds the potential barriers set by the surface roughness and chemical heterogeneity. For the hydrophilic surfaces, it is noted that the critical contact angle at which the droplet radius also starts to decrease is increased for the HCl solution. This means that the introduction of acids has significantly affected the surface tensions of the liquid-solid and liquid-vapor interfaces.

Conclusion

In conclusion, no drop size dependence was observed from 0.5 mm to 10 mm base radius. The data spread is mostly due to the changes in surface heterogeneity. The evaporation method provides a way to measure the receding contact angle as a function of size without the surface heterogeneity being a variable. And analyzing the volume as well as the base radius would allow for a direct comparison between the two methods. Future work should focus on extending the droplet size range to smaller volumes. Using thermochemical nanolithography, hydrophilic and hydrophobic patterns of several tens of nm can be designed on a surface,[22] allowing for the formation and analysis of much smaller droplets.[23] Also, studying a smaller area of the sample will reduce variations in surface topography and chemical heterogeneity.

Acknowledgements

I would like to thank Georgia Tech University, CMDITR, NSF, my mentor, and my fellow REU participants. The funding was provided by the Center on Materials and Devices for Information Technology Research (CMDITR), an NSF Science and Technology Center No. DMR 0120967.

References

1. Furstner, R. ; et al. Langmuir 2005, 21, 956-961.
2. Autumn, K.; et al. PNAS 2002, 99, 12252-12256.
3. Xiu, Y.; et al. Contact 2007 120, 140.
4. Cheng, Y.; et al. Nanotechnology 2006, 17, 1359-1362.
5. Sghaier, N.; Prat, M.; Nasrallah, S. Chem. Eng. J. 2006, 122, 47-53.
6. Erbil, H.; et al. Langmuir 1999, 15, 7378-7385.
7. Good, J.; Koo, M. J. Colloid Interface Sci. 1979, 71, 283-292.
8. Gaydos, J.; Neumann, A. J. Colloid Interface Sci. 1987, 120, 76-86.
9. Yekta-Fard, M.; Ponter, A. J. Colloid Interface Sci. 1988, 126, 134-140.
10. Drelich, J.; Miller, J.; Hupka, J. J. Colloid Interface Sci. 1993, 155, 379-385.
11. Li, D.; Neumann, A. Colloids Surfaces 1990, 43, 195-206.
12. Amirfazli, A.; Chatain, D.; Neumann, A. Colloids Surfaces 1998, 142, 183-188.
13. Amirfazli, A.; et al. J. Colloid Interface Sci. 1998, 205, 1-11.
14. Amirfazli, A.; et al. Langmuir 2000, 16, 2024-2031.
15. Gu, Y. Colloids Surfaces 2001, 181, 215-224.
16. Ababneh, A.; Amirfazli, A.; Elliott, J. Canad. J. Chem. Eng. 2006, 84, 39-43.
17. Tadmor, R.; Yadav, P. J. Colloid Interface Sci. 2008, 317, 241-246.
18. Li, D. Colloids Surfaces A, 1996, 116, 1-23.
19. Vafaei, S.; et al. Nanotechnology 2006, 17, 2523-2527.
20. Ryley, D.; Khoshaim, B. J. Colloid Interface Sci. 1977, 59, 243-251.
21. Zhang, X.; et al. ChemPhysChem 2006, 7, 2067-2070.
22. Wang, D.; et al. App. Phys. Lett. 2007, 91, 243104.
23. Checco, A.; Gang, O.; Ocko, B. Phys. Rev. Lett. 2006, 96, 056104.

KIM REISHUS is a sophomore chemistry major at Taylor University in Upland, Indiana. She enjoys reading and playing volleyball, and doing as much undergraduate research as possible to prepare for graduate school.

Single Molecule Spectroscopy: Intermittent Luminescence Studies

COLLEEN ROSS, University of Washington
Phil Reid, Department of Chemistry, University of Washington

Introduction

Single molecule spectroscopy (SMS) provides greater insight into guest-host interactions of dye-doped polymer substrates than traditional bulk studies. SMS eliminates ensemble averaging, exposing molecular behavior that is otherwise lost in bulk studies. Our project aims to use single molecule probes to investigate the distribution of dielectric environments in polymer hosts that are relevant to opto-electronic applications. We are particularly interested in amorphous polycarbonate (APC) because of its common use in opto-electronic devices. The dielectric probe molecule is violamine R (VR), a common laser dye.

The goal for this summer was to define a protocol for the fabrication of thin films of suitable quality for SMS using an APC/VR composite. To accomplish this, several areas had to be addressed:

- Appropriate solvent for polymer/dye composite
- Aggregation of dye molecules
- Fluorescent contamination

Blinking in dye molecules

Previous studies have shown that some fluorescent molecules exhibit intermittent luminescence, switching between "on" and "off" states. This phenomenon is commonly known as blinking. A simple model for the blinking mechanism is shown in Figure 1.

Molecules are capable of demonstrating a variety of blinking behaviors. Some of these behaviors are shown in Figure 2.

These blinking behaviors depend on the dielectric environment of the system. Previous research in the Reid lab suggests that VR molecules in KAP crystals experience a variety of dielectric environments.[3] Figure 3 shows the distributions of energy shifts from the ensemble-averaged emission energy. The broad distribution of emission energies implies a variety of dielectric environments within a single crystal.

Wustholz, et al. hypothesize that this distribution stems from spectral diffusion, or shifts in the excited state of the molecules[3]. Because crystals are relatively ordered environments, this distribution was surprising. Researchers have been approximating the dielectric environments of polymer substrates as constant.[4,5] In light of Wustholz, et al.'s research, this approximation is probably invalid, and now the expectation is that this distribution will be even wider in disordered polymer matrices. Understanding the patterns of these distributions, and why they occur, will allow for improvement of current models. These improvements will further the understanding of the guest-host systems in EO materials, and can be used to investigate how to improve EO devices.

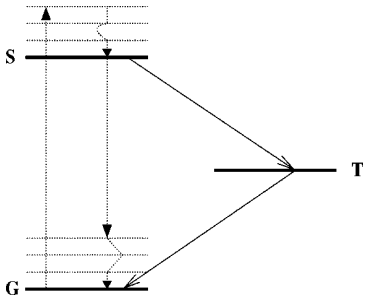

Figure 1. An electron is photo-excited from the ground state (G) to the excited singlet state (S). Then, it either goes to a "dark," triplet state (T), or back to the ground state, releasing energy on the way through fluorescence.[1]

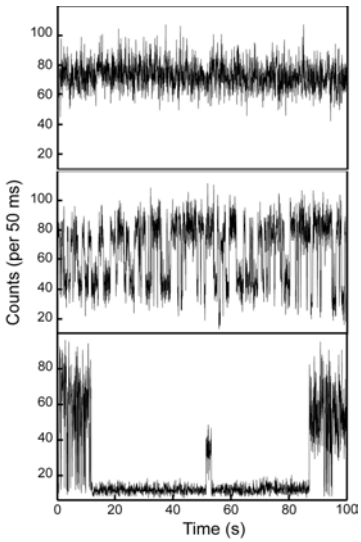

Figure 2. Time traces of VR molecule fluorescence in potassium acid phthalate (KAP) crystals, showing (a) constant emission, (b) fast blinking, and (c) both fast and slow blinking, with two "off" periods lasting over 30 seconds each.[2]

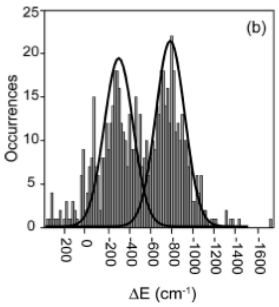

Figure 3. Energy shifts (ΔE) from the emission maximum of the ensemble-averaged spectrum demonstrates two distinct red-shifted populations with Gaussian distributions.

Experimental

The Scope

Our samples were examined with an inverted scanning fluorescence confocal microscope (Nikon T2000U).[6] A diagram is provided in Figure 4. The samples are excited with 532 nm wavelength light from a Nd:VO_4 laser (Spectra-Physics Millennia). The laser light is circularly polarized in order to excite as many molecules as possible. The laser light is reflected by a dichroic mirror into the objective and onto the raster scan stage. The light emitted by the sample passes back through the objective (Nikon, 100x, 1.3 NA), through an emission filter to filter out any laser light, and through a 75 µm pinhole, which increases the resolution. The emission passes through a beam splitter cube and is sent to the avalanche photo diode (APD) detectors (PerkinElmer, SPCM-AQR-16), which are sensitive enough to detect single photons.

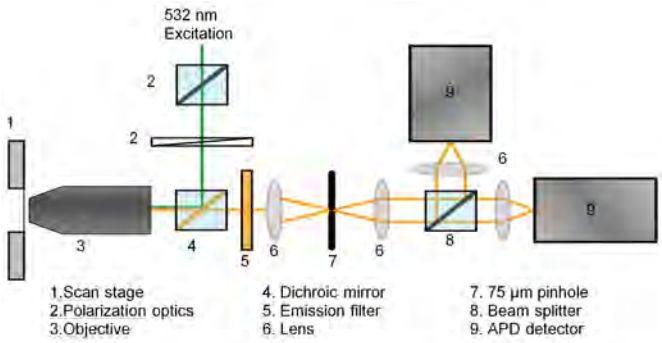

Figure 4. Schematic of the confocal microscope.[7]

Solubility

The first step in our studies was to find an appropriate solvent that would dissolve both the dye and the polymer, and would make high quality thin films when spin coated. None of the solvents tested dissolved both the dye and the polymer completely. A combination of dimethyl sulfoxide (DMSO) and cyclopentanone (CPN) was then tried but they did not spin coat well. Furthermore, the polymer as purchased did not dissolve well. Fractionating the polymer with dichloromethane and hexanes allowed it to dissolve fully. Cyclopentanone was determined to be the most suitable solvent because it dissolved fractionated APC well, and made films of excellent quality. Because VR is not fully soluble in CPN, dilute supernatant had to be used for sample preparation. As a result, the concentration of dye was unknown. The molar absorptivity of VR in CPN was so low that the extinction coefficient could not be determined spectroscopically and Beer's law tests could not be run in CPN. VR was dissolved in a variety of solvents to find an extinction coefficient that could be used to determine concentration. The extinction coefficient of VR in DMSO was used, because, of the solvents tested, DMSO's structure is most similar to that of CPN.

Aggregation

Experimental conditions that prevent aggregation of the dye molecules were determined. Aggregation can occur at high concentrations or when the dye molecules are not evenly dispersed, which can occur in poorly mixed multisolvent solutions. To ensure detection of single molecules, nanomolar concentrations were used and samples were probed with the microscope. Figure 5 shows an early sample scan, which did contain aggregated molecules. The aggregation was likely a result of improper mixing of the DMSO and CPN in the sample. After switching to a single solvent, no more aggregation was detected.

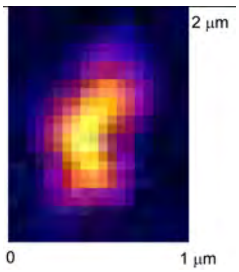

Figure 5. Fluorescence scan of 10-9 M VR/10 wt% APC in DMSO/CPN. The shape of the spot and the unusually high counts (~12,000/10ms bin) suggest this fluorescence is from an aggregate.

Contamination

The biggest obstacle was contamination, which was addressed in the glass substrate, the solvent, and the polymer. Glass coverslips were boiled in a solution of 3 parts deionized water, 2 parts ammonium hydroxide, and 1 part hydrogen peroxide. They were stored in glass Petri dishes after it was discovered that the previous storage method (on a Kimwipe in a plastic Petri dish) caused contamination. Prior to spincoating, slides were rinsed by spincoating with acetone and then isopropanol. All glassware was left in a base bath (~1M KOH) overnight and then rinsed with DI water and acetone prior to use. The CPN was distilled. APC was fractionated by dissolution in dichloromethane (DCMe), filtration through a frit funnel with filtering agent Celite 545, then precipitation in hexanes. Remaining fluorescent contamination in APC/CPN solutions was photobleached by 2 hours of UV radiation (320–450nm).

Results and Discussion

Photon counts were measured in 100 ms time bins. Scans revealed photon counts of 200-400 for individual VR molecules, with a mean maximum count around 250. From this information, the threshold for our studies was set around 200 or 300 photons per 100 ms bin, meaning that any spots that registered under this threshold would be labeled as background noise. After distillation, average max photon counts for CPN were about 125. After distillation and radiation with a UV lamp, average max photon counts for CPN were reduced to about 50. Immediately after cleaning, average max photon counts for the glass substrates were about 15, however, after prolonged exposure to air or contact with Kimwipes, the max counts went up to around 300. Prior to this experiment, standard storage procedure for cleaned glass slides had been to place them in plastic Petri dishes lined with Kimwipes. Cleaned slides will now be stored in cleaned glass Petri dishes, which should assist in further reduction of contamination. After fractionation and UV irradiation for 15 minutes, average max counts for 10 wt% APC were about 375. After one hour of irradiation, the counts dropped to about 125.

Conclusion

The goal for this summer was to produce thin films of APC and VR of suitable quality for SMS studies. To do this, the issues of solubility, aggregation, and contamination had to be addressed. The biggest breakthrough was the use of UV irradiation to photobleach any fluorescent contamination. We now have consistently low photon counts in our polymer substrates, indicating that the blinking behavior that has been detected is from the dye molecules. In the future, the Reid lab will investigate the effects that local dielectric environments have on the polymer/dye system.

Acknowledgements

Mimosa Burr

Philip Reid

The Reid Group

Ben Olbricht

Phil Sullivan

Marya Dominik

Dreyfus Undergraduate Scholarship

The Hooked on Photonics REU program

References

1. Barkai E., Jung Y., Silbey R. Annu. Rev. Phys. Chem. 2004 55, 457-507.
2. Wustholz K.L., Bott E.D., Isborn C.M., Li X., Kahr B., Reid P.J. J Phys. Chem, C 2007 111, 9146-9156.
3. Wustholz K.L., Bott E. D., Kahr B., Reid P.J. J Phys. Chem., C 2008, 112, 7877-7885.
4. Issac A., Von Borczyskowski C., Cichos F. Phys. Rev. B 2005, 71, 161302.
5. Rommel H.L, Robinson B.H. J. Phys. Chem. C 2007, 111, 18765-18777.
6. Wallace P.M., Sluss D.R.B, Dalton L.R., Robinson B.H., Reid P.J. J. Phys Chem. B 2006, 110, 75-82.
7. Figure provided by Daniel Sluss.

COLLEEN ROSS

Novel Host Materials for Highly Efficient Blue Emitting OLEDs

RICHARD SCHAUGAARD, Edmonds Community College
Michelle Liu, Department of Materials Science and Engineering, University of Washington

Introduction

Of all the organic semiconducting materials, organic light emitting diodes (OLEDs) are perhaps the most well known to the general public as they are just now appearing in the marketplace. These displays are based on thin layers of organic materials that allow for directly emitting pixels, and these materials have numerous advantages over liquid-crystal and plasma-based technologies. Compared to competing technologies OLEDs are thinner, lighter and more power efficient since they do not need be backlit or produce plasma. The picture emitted is also non-directional with high contrast ratio; giving OLED displays some of the features of CRT based displays on a screen about than 3mm thick[1]. Surprisingly, this technology is also far from being perfected.

While serviceable in specialized devices such as picture displays, OLEDs are still too inefficient to be seriously considered for use in general lighting applications. The single greatest challenge in this regard comes from the physics involved in the operation of the device. Holes and electrons are generated by the current running through the device, and transported into an emissive layer where they combine to form a molecular excited state that can relax by emitting a photon. However, the chaotic nature of this recombination yields three non-emissive triplet excited states for every emissive singlet state (Figure 1). This can be partially remedied by creating an emissive layer structure that consists of an organic host which donates triplet and singlet excitons to a phosphorescent heavy metal complex. This potentially allows the efficiency of the emissive layer to increase dramatically[2].

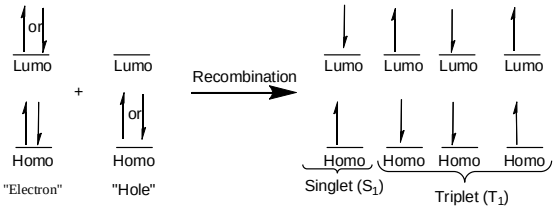

Figure 1. Spin multiplicity in excited states

The complication of using phosphors is the possibility of phosphorescent quenching, which occurs when the heavy metal complex dopant transfers an exciton back to the host; reducing the efficiency of the host/guest system. This occurs most dramatically when the host has a triplet energy less than that of the host. When using high triplet energy dopants, such as blue emitting complexes, this becomes a particularly difficult problem (Figure 2). High triplet energy hosts have high band gaps which limits their ability to transport electrons, which in turn creates a charge imbalance in the emissive layer and reduces efficiency. Additionally, guest-guest quenching can also occur if the dopant is used in excessive concentrations. Star-shaped host molecules have been found to alleviate both of these problems[3,4]. By adding electron transporting moieties onto these molecules, charge distribution in the emissive layer can be improved[3]. Additionally, the steric bulk of these molecules allow more guest molecules to be doped into the emissive layer[4]. For these reasons the focus of the research described in this paper was the synthesis and characterization of novel star-shaped large band gap small molecule host materials with electron transporting moieties. Triazine based molecules were developed to have electron transporting moieties, while analogous triphenyl amine based molecules with the same side groups were used to determine the effects of the triazine groups.

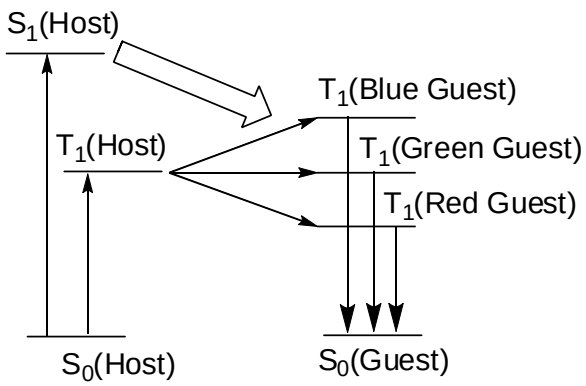

Figure 2. Schematic of energy transfer between modern hosts and primary color emitting guests

Results and discussion

Synthesis of TPA-DPAF2 was accomplished through a Friedel-Crafts reaction between diphenylamine and an available fluorene compound (Scheme 1). This was followed by a modified Ullman reaction between tris(4-iodophenyl)amine and the previously synthesized compound. All other compounds had been synthesized prior to this. The elucidation of HOMO and LUMO levels of the host materials was accomplished via a combination of UV-vis spectroscopy and cyclic voltammetry (Figure 3). Oxidation of the host enabled the determination of the HOMO level. Reduction of the hosts was attempted but was unsuccessful in the range of 0 to -2400 mV for all the species tested. This is especially curious since the triazine based hosts were designed to have electron transport capabilities and therefore should oxidize within that range. TAZ-CzF2 did not give any interpretable CV data despite multiple

attempts. The LUMO levels were extrapolated by first determining the band gap from UV-vis data and then adding this number to the HOMO level. Since TAZ-CzF2 was never successfully analyzed using CV the HOMO and LUMO levels of this compound remain unknown, though the band gap is. Though all of the compounds we were able to analyze showed a reversible oxidation reaction on CV, in practice all the substrates but those containing TPA-DPAF2 were consumed after the first oxidation. While not definitive, this seems to indicate that these compounds may not be as electrochemically stable as would be desired for this type of material.

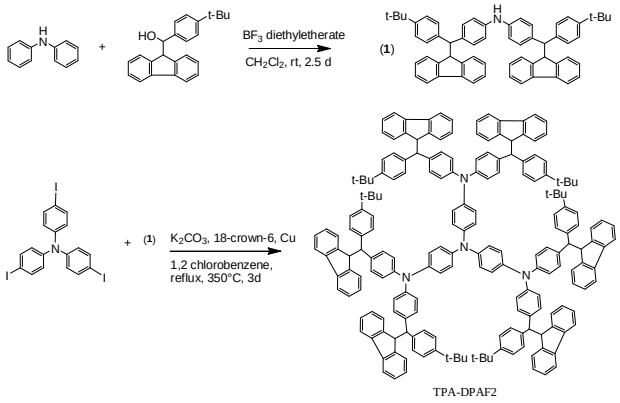

Scheme 1. Synthesis of TPA-DPAF2

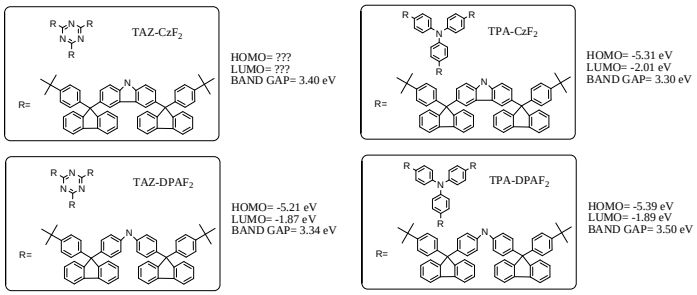

Figure 3. Structures and characteristics of hosts studied.

Photoluminescence spectroscopy revealed similarities between the spectral shapes of the triazine based hosts and their triphenyl amine based analogs (Figure 4). The most significant difference is a "red shift" that occurred in the triazine based compounds. This may indicate an intramolecular energy exchange reaction between the relatively easily oxidized "arms" and the relatively easily reduced "body". If this is in fact occurring it would have the effect of lowering the triplet energy of the triazine based hosts and thus reduce their effectiveness.

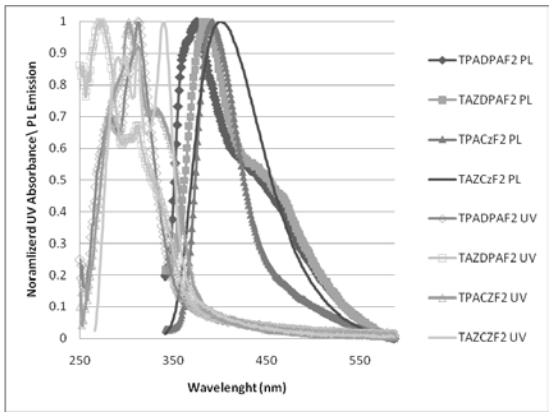

Figure 4. Combined PL and UV spectrums of the hosts studied

Devices were also created using TPA-CzF2 and TAZ-CzF2 in order to test the properties of those hosts (Table 1). When doped with the electron transport material OXD-7 TPA-CzF2 shows performance comparable to PVK, whereas TAZ-CzF2 shows dramatically less performance. This may be due to the possible triplet energy lowering intramolecular energy exchange detected in the PL spectrum. However, the efficiency of TAZ-CzF2 was virtually unchanged in devices with and without OXD-7. This indicates that electrons are being transported by this host. Both TPA-CzF2 and TAZ-CzF2 showed that they were able accept up to 21% FIrpic without quenching, indicating that the shape of these molecules allows for better segregation of guest materials and therefore reduces guest-guest quenching.

Al (100 nm) / CsF (1 nm) / TPBI (25 nm) / EML (50 nm) / VB-TCTA (20 nm) / PEDOT (30 nm) / ITO / Glass	OXD-7[a]	Host	Guest	% EQE[b]	lm W^{-1}
		TAZ-CzF2	7% FIrpic	5.6	6.7
			14% FIrpic	7.8	8.6
			21% FIrpic	8.2	8.5
		TPA-CzF2	7% FIrpic	2.5	2.3
			14% FIrpic	5.2	7.3
			21% FIrpic	8.3	10.5

Al (100 nm) / CsF (1 nm) / TPBI (25 nm) / EML (50 nm) / PEDOT (30 nm) / ITO / Glass	OXD-7[a]	Host	Guest	% EQE[b]	lm W^{-1}
		PVK	14% FIrpic	6.0	6.7
		TAZ-CzF2	14% FIrpic	2.0	1.4

		Host	Guest	% EQE[b]	lm W^{-1}
		PVK	14% FIrpic	1.2	0.9
		TAZ-CzF2	14% FIrpic	1.8	1.4

Table 1. Structure and performance of devices; a) OXD-7 is an electron transporting material and b) EQE is external quantum efficiency.

Conclusion

The compounds investigated here were shown to exhibit favorable qualities for use in OLEDs. Similar hosts that exhibit electron transporting qualities and increased guest tolerance, but with more favorable triplet energies are likely. Therefore, the design strategies employed in this project should continue to be used to develop host materials that are readily synthesized and easily processed from solution.

Experimental

Syntheses

All reactions were quenched with H_2O and extracted from CH_2Cl_2 / water. Solvent was removed by mild heating under reduced pressure and the compound of interest eluted from a silica gel packed column using a CH_2Cl_2/hexane solution of a ratio determined by analyzing a TLC of the mixture. Structure of compounds was divined from NMR spectroscopy.

Substrate cleaning procedure

All substrates were wiped with a cotton swab and detergent before being pulsed in an H2O/detergent mixture in an ultrasonic cleaner and rinsed with DI water. Substrates were then pulsed in acetone then isopropanol.

CV

Substrates were cleaned using substrate cleaning procedure on 1inch/.5 inch ITO coated substrates. 1% mass solution of host material in chlorobenzene was coated on ITO side of substrate and spin coated at 1.2 krpm for 30 sec. CV conducted using Ag/Ag+ reference electrode in .1M tetra-n-butylammonium fluoride in acteonitrile. Oxidation standard was ferrocene. By comparing the potential of the first incident curve against the observed position of ferrocene and extrapolating from the known work function of that species.

PL / UV-vis

Substrates were cleaned using substrate cleaning procedure 1inch/1inch microscope slides. 1% mass solution of host material in chlorobenzene was coated on substrate and spin coated at 1.5 krpm for 30 sec. PL and UV-vis spectrums of identical compounds taken using the same substrates. PL spectrums were taken using an excitation wavelength of 303 nm. UV was used to determine the band gap by converting the wavelength of the first incident curve into eV.

Acknowledgements

This work was made possible by the NSF sponsored Science and Technology Center on Materials and Devices for Information Technology Research. Thanks are extended to: Prof. Jenekhe, the Jenekhe research group, Prof. Reid, Marya Dominik, Miranda Robertson, Sara Selfe, Mary Whitfield, Neil Tucker, Orb Acton, Fei Huang, and Steven Hau.

References

1. Reviews.Cnet.Com. http://reviews.cnet.com/oled/sony-xel-1-oled/4505-13948_7-32815284.html?tag=prod.txt.1 (accessed 8-16-08). Review of Sony XEL-1 OLED TV
2. Zhang, Y., et al. Highly efficient White Polymer Light-Emitting Diodes Based on Nanometer-Scale Control of the Electron Injection Layer Morphology through Solvent Processing. Adv. Mater. 2008, 20, pp 1-6
3. Ge, Z., et al. Solution-Processible Bipolar Triphenylamine-Benzimidazole Derivatives for Highly Efficient Single-Layer Organic Light-Emitting Diodes. Chem. Mater. 2008, 20, 2532-2537.
4. Shih, P.-I, et al. Novel Carbazole/Fluorene Hybrids: Host Materials for Blue Phosphorescent OLEDs. Org. Lett., 2006, 8, 13, 2799-2802

RICHARD SCHAUGAARD

Control Systems and Laser Beam Stabilization

KRYSTAL R. STEVENSON, Norfolk State University
Tom Milster, University of Arizona

Introduction

The growing cost of lithography masks is increasing concerns for future technology generations. As a solution, maskless lithography is being developed. This new system eliminates the need for any lithographic masks. It also reduces time and cost for prototyping. There are many variations of maskless lithography- Electron Beam Direct Write, Charged Particle Maskless Lithography, and Optical (or Photonic) Maskless Lithography.

At the University of Arizona, researchers specifically use the optical approach. The Maskless Lithography Tool (MLT) at University of Arizona was designed as a research prototype to image binary and gray-scale high density patterns onto UV sensitive materials. Some of these UV materials are photoresists and sol-gels. The MLT is based on conventional optical lithography scanner architectures, except that the photo mask is replaced with an array of light modulating elements that are used to generate the mask pattern in real time. The wanted outcome is to write the patterns directly into the photoresist layer using a laser beam. While completing tasks of the MLT, University of Arizona stumbled upon some concerns of their own.

Pointing stability of the laser is the major concern. The laser internal thermal effects and the adjustable optics mounts can cause pattern problems, such as instability of the lateral or angular beam position. A closed loop laser stabilization servo system is applied to the MLT to correct the drift of the laser beam.

Optical beam servo systems have wide applications for many applications that require laser beam pointing. Beam stabilization servo systems correct laser misalignment. At the start of this project, this servo system was not optimized.

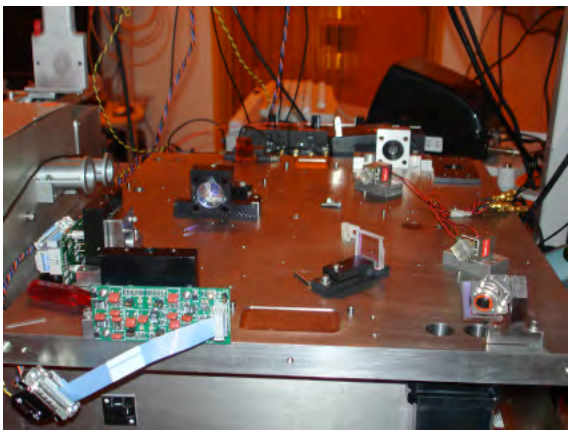

Figure 1: Servo System (taken from Yuming Shen "Engineering Principles of the UA Maskless Lithography Tool")

Theory

A control system is an interconnection of components making a configuration that provides a desired system response. The analysis of this system is based on linear system theory. There are two different approaches to control systems, which are called open loop and closed loop systems.

The difference between a closed loop and open loop system is that closed loop control systems use an additional measure *H(s)C(s)* of the output in order to compare the actual output with the desired output response. The closed loop system includes generation and utilization of the error signal. When operating correctly, it operates so that the error is reduced to a minimum value.

"A closed loop feedback system is a control system that tends to maintain a prescribed relationship of one system variable to another by comparing functions of these variables and using the difference as a means of control" (Dorf)[2]. The feedback system has been the main foundation for control system analysis and design. There are many methods of examining analysis and design of such systems. At the University of Arizona, beam stabilization for the Maskless Lithography Tool (MLT) is accomplished with closed loop feedback servos.

The closed loop transfer function has many advantages over an open loop transfer function. A process will sometimes change due to age and environment, which will eventually display an error. An open loop system will ignore the change and produce these errors and inaccurate outputs. A closed loop system will sense these errors and try to correct the output. A big advantage of a closed loop system is that it has the ability to reduce the system's sensitivity to disturbances.

Closed loop transfer functions assure that a system performs within the control limits. The system's output feeds back directly to change the system's input. Closed loops utilize the error signal and cause error signal reduction to a minimum value.

Open Loop Transfer Function

$$C(s) = G(s)R(s)$$

Closed- Loop Transfer Function

$$C(s) = G(s)E_a(s)$$

$$C(s) = G(s)[R(s) - H(s)C(s)]$$

$$C(s) = \frac{G(s)}{1 + G(s)H(s)}R(s)$$

(C(s) = output, R(s) = input, G(s) = actual signal/transfer function, E_a = error signal)

Enhanced control is all possible for closed loop systems because when $GH(s) >> 1$, then $$C(s) \cong \frac{1}{H(s)} R(s)$$

If $H(s) \approx 1$, the output will equal to the input regardless of the value of $G(s)$. As the magnitude of the loop transfer function $GH(s)$ is increased, the effect on $G(s)$ is reduced.

Relative stability for the frequency response method is defined in terms of the 0 db, 180˚ point on the Bode diagram However, there is a limit to the system stability. There are two distinct ways of measuring relative stability. phase margin and gain margin. The phase margin is equallent to the total phase lag allowed before the system becomes unstable. On the Bode diagram, the phase margin is measured at the point where the logarithmic magnitude is 0 db.

A simple way to visualize unstable operation is to substitue $G(s)H(s) = -1$ into the denominator of the closed loop transfer function. In this case, the output $C(s)$ is always infinity, which is an unstable condition. The gain margin is equallant to the total gain availble for where phase is -180˚.

Research Method

In order to began considering fixing a stability problem, the background of the subject must be read. It is also possible to be familiar with operating the laser, and understanding how to operate, run, and analyze a digital oscilloscope. An oscilloscope measures the voltage and time or frequency.

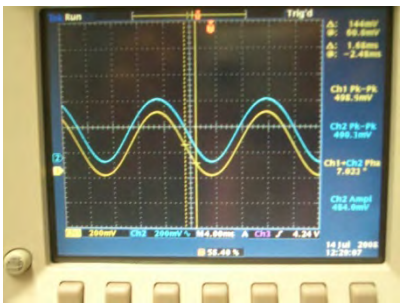

Figure 2: Digital Oscilloscope

Before the servo was added to the MLT, there was about 100mV of error caused by beam movement. However, after designing and adding a servo to the system, the error went down to about 20mV. Although an error of 20mV would be acceptable for writing bigger patterns, smaller patterns need to achieve an error less 1mV. While using a digital oscilloscope, the frequencies, input and output peak to peak, phase shift, the input and output amplitude was recorded. This test was first applied to the of the circuit card inside of the MLT. Data was collected at the input test point and the lead lag test point. After changing the amplitude of the lead lag test point from one volt to .250V and at .5V, the experiment seemed to be on track. Therefore, at the lead lag test point another test was applied varying capacitor values- no capacitor, 10nf, 47nf, 4.7nf, 1nf, and 470pf capacitor. After plotting and reviewing the results, it was necessary to run a test varying the same capacitor values, but also adding resistor values- 5k, 10k, and 20k.

Figure 3: Circuit Card

After running the test with the circuit card, tests were run on the actual servo system. With amplitude of .5V, the test frequencies ranged from 10 Hz to 1.5 kHz. This test was applied without any added capacitors and then with a .01 capacitor. Once this process was complete, I collaborated with an electronic engineer to re-measure the frequency responses. All of the data was then plotted in a Bode diagram using a Mat Lab program.

Results

The servo circuit board's Bode plots were obtained for several RC values of the lead lag circuit. The slopes of the plots were examined and compared to see how values change the system. This information will be used in subsequent optimization. The MLT open loop servo data indicated that the capacitor did not change the circuit.

MLT Servo without Capacitor

Frequency (Hz)	Input Pk-Pk (mV)	Output Pk-Pk (mV)	Phase Shift (degrees)	Input Amplitude (mV)	Output Amplitude (mV)	Output/Input Amplitude
10	1000	308	178.6	988.0	300.0	-10.352
50	997.5	298	-174.4	989.8	297.0	-10.455
100	995.1	291	-165.3	988.6	285.8	-10.779
200	995.3	277	-149.7	988.0	272.7	-11.181
400	996.2	224	-106.3	992.4	218.5	-13.144
600	997.0	142	-60.1	992.0	140.0	-17.007
800	1016	97.6	-25.8	1008.0	96.0	-20.423
1000	1021	65.6	-4.8	1017.0	65.6	-23.808
1200	1025	51.0	16.8	1016.0	48.9	-26.351
1500	1035	37.3	45.2	1030.0	35.2	-29.325

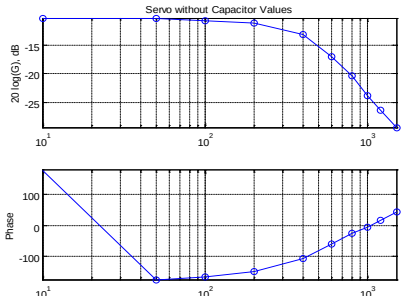

Figure 4: Data and Bode Diagram for MLT Without Capacitor

MLT Servo with .01 Capacitor

Frequency (Hz)	Input Pk-Pk (mV)	Output Pk-Pk (mV)	Phase Shift (degrees)	Input Amplitude (mV)	Output Amplitude (mV)	Output/Input Amplitude
10	1001	536	179.1	984.0	552.0	-5.021
50	995.3	519	-177.3	984.0	510.0	-5.708
100	993.0	508	-172.3	984.0	504.0	-5.8113
200	992.7	505	-162.9	988.0	502.0	-5.8811
400	994.2	468	-137.0	988.0	502.0	-5.8811
600	996.3	349	-105.2	992.2	468.0	-6.5271
800	1003	268	-76.9	997.8	344.9	-9.2270
1000	1009	199	-53.5	1002.0	267.0	-11.4871
1200	1021	174	-32.7	1016.0	195.0	-14.3372
1500	1031	147	-7.9	1028.0	143.0	-17.1331

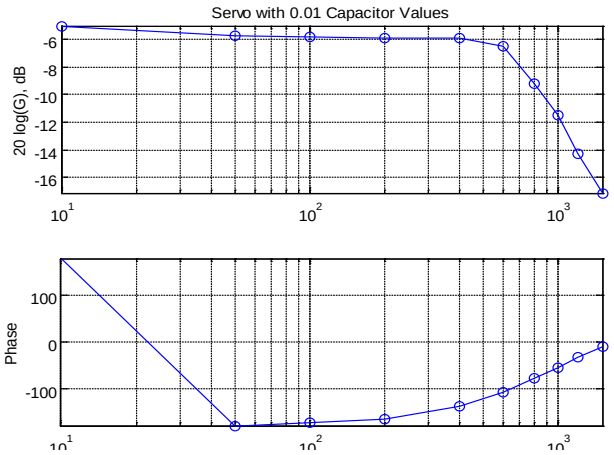

Figure 5: Data and Bode Diagram for MLT.01 Capacitor

Conclusion

After carefully analyzing the data, the results indicated no change in performance. The low frequency gain and the phase margins suggest that further optimization is necessary in the servo circuits. Also, the low DC gain indicates that the feedback loop is not implemented properly. Although the desired performance of 10mV of error maximum was not achieved, a path was shown for further analysis and optimization. It is likely that the desired performance of 10mV maximum error can be achieved. performance of 10mV of error maximum was not achieved, a path was shown for further analysis and optimization. It is likely that the desired performance of 10mV maximum error can be achieved.

Acknowledgments

Funds for this research were provided by the Center on Materials and Devices for Information Technology Research (CMDITR), and the NSF Science and Technology Center No. DMR 0120967, University of Arizona, Tom Milster, Hooked on Photonics, Norfolk State University and Dr. Arlene Maclin.

References

1. Dorf, Richard C. Modern Control Systems. New York: Addison-Wesley Longman, Incorporated, 1986.
2. Yuming Shen, “Engineering Principle of the UA Maskless Lithography Tool (MLT)”, A Master’s Report, University of Arizona, May 2008

KRYSTAL STEVENSON is a student at Norfolk State University. She is earning a degree in Electronic Engineering.

The Effects of Binding Ligands on Nickel Catalysts in the Polymerization of Poly(3-Hexylthiophene)

MICHELINA STODDARD, Seattle Central Community College
Natasha Doubina, Christine Luscombe, University of Washington

Abstract

Organic semi-conducting polymers (OSPs) demonstrate promise in the use of photovoltaic devices; however, they are difficult to polymerize in a reproducible and controlled manner due to the step-growth nature of polymerization that results in random coupling of polymer, oligomer and monomer units. In order to fully utilize the attractive qualities of π-conjugated organic polymers for the improvement of organic electronic devices, polymerization methods must be developed that allow for greater control over the properties of synthesized polymers. An investigation of the special type of chain growth polymerization, catalyst-transfer polymerization, for the synthesis of poly (3-hexylthiophene) is described. P3HT polymerization from external initiators such as chlorobenzene, ortho-chlorotoluene and para-chlorotoluene was attempted utilizing nickel catalyst with various binding ligands such as dppp, dppe, dppf and PPh_3.

Background and Introduction

OSPs have presented challenges and promise to scientists since their discovery roughly 30 years ago. The OSPs flexibility could offer many uses, from more efficient electronics to organic solar cells. These potential uses have motivated extensive research on their chemical and physical properties. Control of the chain-growth mechanism presents a perplexing challenge in the applications of OSPs. Literature and previous work by the Luscombe group has suggested that the catalyst used in the reaction has a significant effect on the outcome of the polymerization.[1,2]

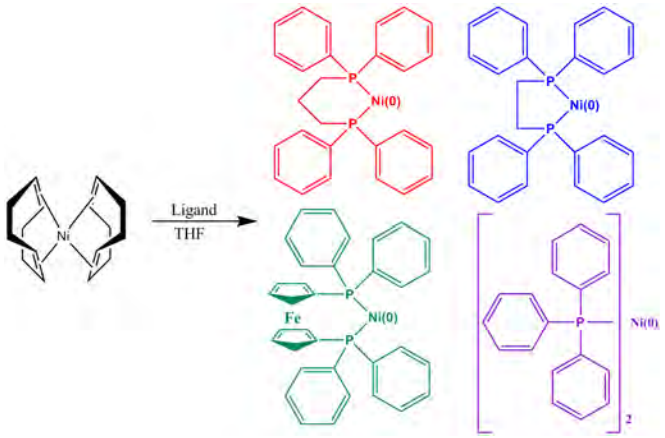

Figure 1: $Ni(COD)_2$ combines with one of the four ligands to create one of the nickel catalysts used in the polymerizations of poly(3-hexylthiophene).

Most research on nickel catalysts has been done with uninitiated polymer variations. This study presents interesting implications because our reaction begins with creating a complex with the nickel catalyst and the initiating molecule. The effectiveness of the catalyst depends greatly on the type of ligand used (due to stability, bite angle, and other factors).[3,4,5,6,7] Four common ligands will be examined in this study for their general effectiveness in the polymerization of P3HT: di(phenylphosphino)propane (dppp), di(phenylphosphino)ethane (dppe), di(phenylphosphino)ferrocene (dppf), and tri(phenyl)phosphine (PPh_3). Analytical methods such as MALDI-TOF , ^1H NMR and GPC will be used to characterize P3HT polymerizations from nickel catalysts with various binding ligands by studying polymer end-groups, molecular weight and polydispersity index.

Procedures

Ni(0) was bound to the ligand by adding $Ni(COD)_2$ to one molar equivalent of the ligand, with the exception of PPh_3, of which we added two molar equivalents (see Table 1 for exact amounts added).

Table 1: Exact amounts of catalyst, ligand, and initiator used in our polymerizations of P3HT

Ligand	Ligand (mg)	$Ni(COD)_2$ (mg)	Chlorobenzene (mg)	o-Chlorotoluene and p-Chlorotoluene (mg)
Dppp	11.1	7.4	45.4	52.1
Dppe	10.7	7.4	45.4	52.1
Dppf	14.9	7.4	45.4	52.1
PPh_3	14.1	7.4	45.4	52.1

Ligands were placed into three-neck round-bottomed flasks. Inside a glove box enough $Ni(COD)_2$ for all reactions was measured into a round-bottomed flask with a magnetic stir bar. We added 5 mL of dry tetrahydrofuran (THF) per reaction to the $Ni(COD)_2$ and allowed the $Ni(COD)_2$ to dissolve. 5 mL of the Ni solution was added to each of the three-neck round-bottomed flasks and allowed to stir for twenty minutes. After twenty minutes fifteen molar equivalents of chlorobenzene (PhCl) were added and stirred for 2-4 hours to allow the catalyst-initiator complex to form. Several experiments were also performed using o-chlorotoluene and p-chlorotoluene as external initiators employing similar experimental procedures. 1.2 g of 2-bromo-3-hexyl-5-iodothiophene were placed in the flask and the atmosphere was replaced with nitrogen. 20 mL dry THF was added into the flask and the mixture was stirred at 0 °C. Isopropyl magnesium chloride (*i*-PrMgCl: 1.5 mL of 2 M solution) was added and the mixture stirred for 1 hour at 0 °C. After 1 hour, the *i*-PrMgCl-functionalized thiophene monomer solution was equally distributed

between the four flasks containing the catalyst-initiator complexes and allowed to polymerize overnight.

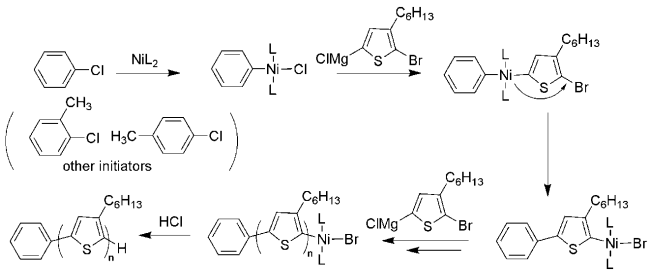

Figure 2: Proposed reaction mechanism for the polymerization of P3HT using our synthesized catalysts and external initiators. Three external initiators were experimented with: chlorobenzene, o-chlorotoluene, and p-chlorotoluene.

To make sure our initiator attached to the polymer, as opposed to normal H-Br end groups, we used MALDI-TOF spectrometry. Gel Permeation Chromatography (GPC) was used to determine the molecular mass of the polymers and their degree of polydispersity (PDI). ^{1}H Nuclear Magnetic Resonance (^{1}H NMR) allowed us to analyze the groups present on the carbon chain of the polymer to determine whether head-to-tail cross-coupling had occurred and to ensure that the proper end groups were present.

Results

Table 2: Summary of the characterization of polymers synthesized with various ligands and initiators

Ligand – Time of Catalyst-Initiator Reaction	Initiator	Percent Yield	End Groups
PPh_3 – 2hr	Chlorobenzene	62%	Phenyl-H and Br-Br
3-hr	*o*-chlorotoluene	88%	Toluene-H, Toluene-Br, and H-Br
3-hr	*p*-chlorotoluene	0%	H-Br and Br-Br
Dppp – 2hr	Chlorobenzene	No Polymer	No Polymer
3hr	*o*-chlorotoluene	No Polymer	No Polymer
3-hr	*p*-chlorotoluene	No Polymer	No Polymer
Dppe – 2hr	Chlorobenzene	0%	H-Br and Br-Br
3hr	*o*-chlorotoluene	0%	HBr and Br-Br
3hr	*p*-chlorotoluene	No Polymer	No Polymer
Dppf – 2hr	Chlorobenzene	36%	Phenyl-H, others unidentifiable
3hr	*o*-chlorotoluene	0%	Br-Br and H-Br
3hr	*p*-chlorotoluene	0%	H-Br and Br-Br

In the first set of experiments, in which PhCl was the initiator, PPh_3 and dppf catalysts produced promising polymers. The polymer catalyzed with dppf produced intiator peaks in both the MALDI-TOF and H NMR spectra, but there are also a number of unknown peaks in both spectra. In addition to higher initiation per reaction, polymer produced with PPh_3 has lower PDI and higher M_n. Dppe Fproduced polymer, but it was uninitiated and not useful for our purposes. Dppp produced no polymer.

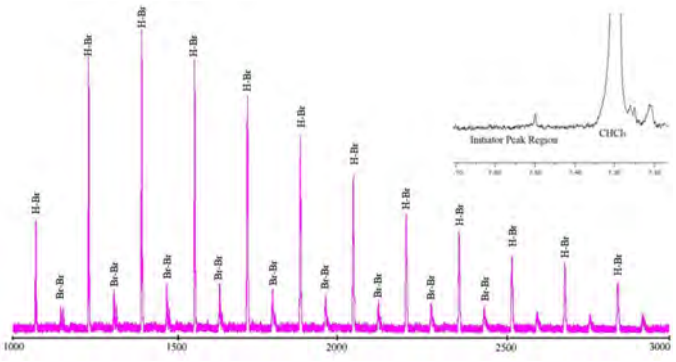

Figure 3: MALDI-TOF (bottom) and H NMR (upper right) spectra of P3HT synthesized with the dppe ligand and initiated with chlorobenzene. No initiator groups are present.

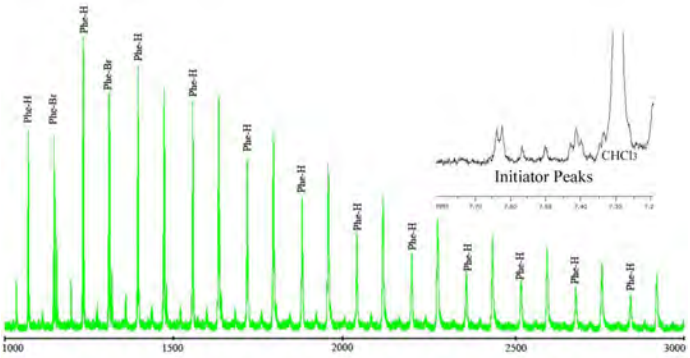

Figure 4: MALDI-TOF (bottom) and H NMR (upper right) spectra for P3HT synthesized with the dppf ligand and initiated with chlorobenzene. Some initiator groups are present, but many peaks are unknown.

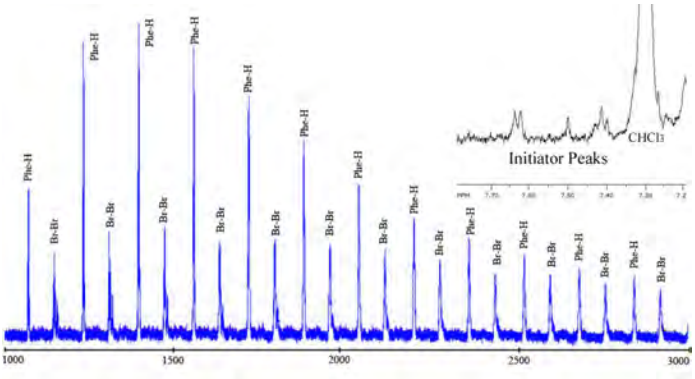

Figure 5: MALDI-TOF (bottom) and H NMR (upper right) spectra of P3HT synthesized with the PPh3 ligand and initiated with chlorobenzene. Initiator groups are present in 62% of the peaks.

The second set of experiments was performed with an *ortho*-chlorotoluene (*o*-ClTol) initiator. PPh3 produced the highest initiated yield once again. Dppf and dppe produced uninitiated polymer, and dppp did not create polymer.

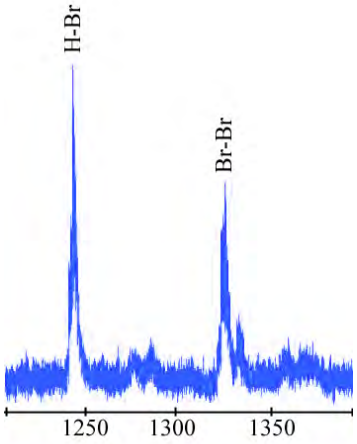

Figure 6: Close-up MALDI-TOF spectrum of P3HT synthesized with the dppe ligand and initiated with o-chlorotoluene. No initiator peaks are present.

Figure 7: Close-up of peaks in the MALDI-TOF spectrum of P3HT synthesized with the PPh3 ligand and initiated with o-chlorotoluene. 88% of the polymer has been initiated.

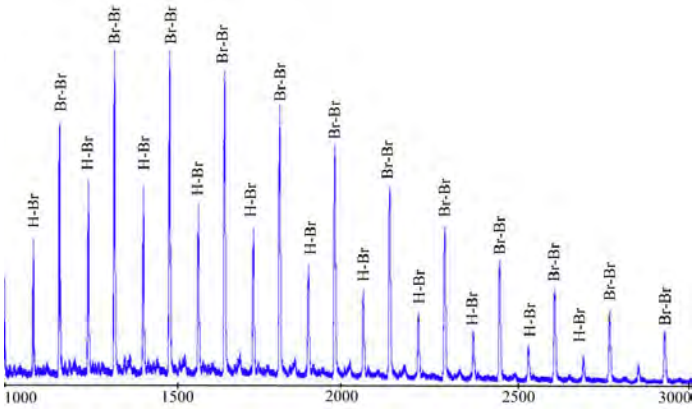

Figure 8: MALDI-TOF spectrum of P3HT synthesized with the dppf ligand and initiated with o-chlorotoluene. No initiator peaks are present.

Discussion

Table 3: Summary of ligands and the effects they had on the percent of initiated polymer.

Ligand	Initiator	Bite Angle (Bn)/Cone Angle (Cn)	Percent Initiated
Dppp	Chlorobenzene	Bn=91°	No Polymer
	o-chlorotoluene	Bn=91°	No Polymer
	p-chlorotoluene	Bn=91°	No Polymer
Dppe	Chlorobenzene	Bn=85°	0%
	o-chlorotoluene	Bn=85°	0%
	p-chlorotoluene	Bn=85°	0%
Dppf	Chlorobenzene	Bn=96°	36%
	o-chlorotoluene	Bn=96°	0%
	p-chlorotoluene	Bn=96°	0%
PPh_3	Chlorobenzene	Cn=145°	62%
	o-chlorotoluene	Cn=145°	88%
	p-chlorotoluene	Cn=145°	0%

As seen in Figures 6-8, two ligands catalyze reactions with reasonable initiation. Some literature suggests that the bidentate ligand with the bite angle closest to 100° operates with optimal activity and selectivity.[4] In that case, dppf should have been the optimal bidentate ligand for the polymerization because it has a bite angle of 96°. Indeed, dppf was the only bidentate ligand to produce initiated polymer. PPh_3, a monodentate ligand, seemed to provide the cleanest, best-initiated polymer. All of the experimental data suggests that PPh3 produces desirable polymer efficiently.

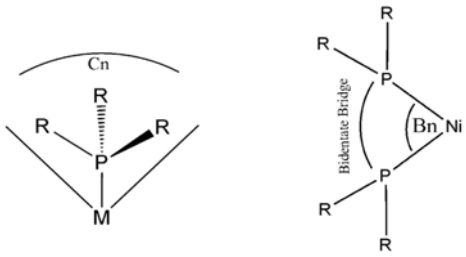

Figure 9: Diagram illustrating a cone angle (Cn) and a bite angle (Bn). Cone angles refer to monodentate ligands (such as PPh_3) and bite angles refer to bidentate ligands (such as dppp).

Each of the ligands contains a combination of one to two phenylphosphine groups with a connecting point, or bridge. PPh_3 makes an excellent ligand because it has no bite angle restrictions and has a wide cone angle (see figure 9). Although previous work indicates that $Ni(PPh_3)_4$ catalysts are very active with poor selectivity,[6] the $Ni(PPh_3)_2$ catalyst used in our studies seems to operate more selectively in the external initiator polymerizations. Since we were unable to obtain polymer with the dppp ligand it may be possible that dppp simply won't react with the initiator or monomer. The uninitiated polymer obtained with the dppe ligand-catalyst suggests that dppe will not react with an initiator after three hours, but may react with the monomer when left overnight. Future experiments will include manipulating catalyst-initiator reaction variables to try to produce initiated polymer with the dppp and dppe ligands.

References

1. Ricardo Po, Nicoletta Cardi, Roberto Santi, Anna Maria Romano, Carla Zamoni, Silvia Spera. J. Polym. Sci. A. 1998. 36:12, 2119-2126
2. Anh Ho, Natasha Doubnia, Christine Luscombe. “Controlled Polymerizations of P3HT”. Poster presentation, University of Washington. 2008.
3. Ryo Miyakoshi, Akihiro Yokoyama, Tsutomu Yokozawa. Macromol. Rapid Comm. 2004. 25:19; 1663-1666.
4. Mirko Kranenburg, Paul C. J. Kamer, Piet W. N. M. van Leewen. Eur. J. Inorg. Chem. 1998; 2; 155-157.
5. Ryo Miyakoshi, Akihiro Yokoyama, Tsutomu Yokozawa. J. Polym. Sci. 2008, 46, 753-765
6. Richard D. McCullough. Adv. Mater., 1998, 10, 93.
7. Piet W. N. M. van Leeuwen, Paul C. J. Kamer, Joost N. H. Reek, Peter Dierkes. Chem. Rev. 2000, 100, 2741-2769.
8. Ryo Miyakoshi, Akihiro Yokoyama, Tsutomu Yokozawa. J. Am. Chem. Soc. 2005, 127, 17542-17547
9. Satoru Amou, Osamu Hava, Kaori Shirato, Teruaki Hayakawa, Mitsuru Veda, Kazuhiko Takeuchi, Michihiko Asa. J. Polym. Sci. A. 1999. 37:13, 1943-1948.
10. Sloan, M. F.; Matlack, A. S.; Breslow, D. S. J. Am. Chem. Soc. 1963. 85. 4015.

MICHELINA STODDARD

Easily-Processed Metal Oxide Thin Films for Use as Interlayers and Encapsulants in Organic Solar Cells

DELVIN TADYTIN, University of Arizona
Diogenes Placencia, Neal R. Armstrong, University of Arizona

Introduction

Titanium dioxide (TiO_2) is a natural occurring oxide of titanium. It has a wide range of applications including sunscreen and paint. TiO_2 is used as a white pigment in outside painting and attractive because of its chemical inertness. When deposited as a thin film TiO_2 is known for its high refractive index and transparency.

The properties of TiO_2 make it attractive for applications as a component of organic photovoltaic cells (OPV's), where it can be used a thin interlayer between adjacent OPV's or as an encapsulation layer over the top of such cells. Because of the complex production and high cost of silicon based photovoltaic solar cells, organic photovoltaics are being researched extensively. The power conversion efficiency of OPV's is very small (~3-5 % efficiency). A key parameter for OPV's is power output per unit area (Watts/cm^2). By building a tandem OPV, where two organic solar cells are stacked on top of each other and connected in series, voltage and power output per unit area can be increased. In studies performed by Heeger and coworkers, a tandem OPV was constructed where they used TiOx as charge recombination layer.[1] The TiOx was applied by spin coating a soluble titanium isopropoxide precursor, using conventional sol gel techniques to form the thin film oxide. This poses a significant problem because very thin layers of TiOx need to be applied. Controlling the thickness of the TiOx layer is difficult through spin coating. In addition, it would be ideal to deposit TiOx in the absence of air and at low temperatures.

Another attractive feature of TiO_2 with respect to OPV's is for the TiO_2 to serve as an encapsulation layer. OPV's are very sensitive to air, especially oxygen and water. By simply exposing OPV's to air, their performance capabilities are dramatically reduced. Depositing TiO_2 onto surfaces at temperatures which will not decompose the sensitive organic dyes in OPV's would be ideal. By encapsulating the OPV's, they can be exposed to air without sacrificing their performance capabilities.

TiO_2 can be deposited through different methods e.g., sol-gel techniques where a metal alkoxide is used as precursor to produce an integrated network (gel). The solution can be deposited onto a substrate through dip-coating or spin-coating. There is a drying process which serves to remove the liquid phase. A thermal treatment may also be performed. As mentioned previously this step can damage organic dyes in OPV's.

An unpublished result by Paul Lee and Neal R. Armstrong suggests metal oxide precursors can decompose to TiO_2 at low temperatures with the assistance of ultraviolet light (Figure 1).

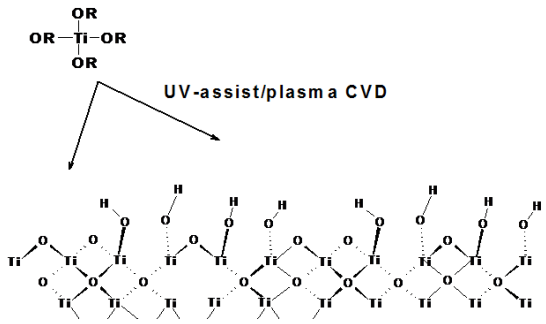

Figure 1. Chemical Vapor Deposition. P. Lee, N. R. Armstrong, unpublished results.

Based off the previous studies by Paul Lee and Neal R. Armstrong, a chemical vapor deposition chamber for depositing TiO_2 was proposed. The chamber required fabrication of glass tubing as shown in Figure 2. Nitrogen gas was bubbled into a solution of titanium isoproxide, and promoted from the liquid phase to the gas phase. Nitrogen gas served as a carrier gas and titanium isopropoxide was heated slightly with a temperature controlled heating source and then bombarded with a 254 nm mercury vapor ultra violet light source. The entire process occured under vacuum at a pressure of ~400 mtorr.

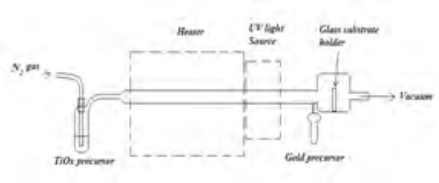

Figure 2. Chemical Vapor Deposition Chamber.

The development of this new CVD chamber required that several variables be identified and controlled: temperature, carrier gas flow rate, time of deposition, and distance from the substrate to the UV light source. To optimize TiO_2 film deposition, one variable was changed at a time until optimal parameters were established. Optimal parameters consider for TiO_2 thin films were: a) the roughness of the deposited surface and b) establishing that in fact TiO_2, or some other sub-stoichiometric oxide was made.

The TiO_2 thin films where characterized with X-ray photoelectron spectroscopy and atomic force microscope (AFM), to verify surface roughness.

Results and Discussion

The chemical vapor deposition chamber was constructed as proposed. The first variable changed was the temperature. The deposition was performed on glass substrates. The results of the deposition can be seen in Table 1. The temperature was changed while the other variables were kept constant. The temperature was varied from 121 °C to 398 °C. The films were analyzed by inspection and by AFM. The films at lower temperatures resulted in smoother TiOx films. The TiOx films at higher temperatures (samples 3-5) were found to deposit very cloudy samples. The sample at 398 °C had very small crystal growth, which was seen by moving the sample from side to side where the reflections of light by individual particles on the surface of the substrate were noticed.

Sample	Carrier gas flow rate: (cc/min)	Time (hr)	Temperature (°C)	Distance (inches)	Film
1	115	1	121	4.25	slightly rough
2	115	1	176	4.25	smooth
3	115	1	232	4.25	rough
4	115	1	287	4.25	rough
5	115	1	398	4.25	very rough

Table 1. Temperature variation. Table of variables. Temperature was varied from 121 °C to 398 °C. Films were analyzed via AFM and determined the roughness.

The optimal temperature was determined to be at 176 °C. From this point the next variable changed was the carrier gas flow rate. The flow rate meter used was very basic; it had a valve with an upper ball and lower ball. The flow meter was calibrated by flowing N_2 gas through the meter and into a graduated cylinder turned upside down. N_2 gas was pumped into the cylinder and timed to a specific volume of water displaced. With a calibrated flow meter deposition of TiOx was performed from 15 cc/min - 100 cc/min.

The time in this particular experiment had changed from 1 hour to 30 minutes. The time change was done for convenience purposes. The time change should not have affected the outcome of the results because it was held constant throughout this particular experiment. By analyzing AFM images of the surface, the flow rate at 68 cc/min resulted in the smoothest films (Table 2). The films at the lower flow rate of 15 and 27 cc/min were, by inspection, very cloudy films. The 15 cc/min flow rate showed crystal growth on surface of the substrate. This was determined by reflection of light by individual particles on the surface of the substrate.

Sample	Carrier gas flow rate: (cc/min)	Time (hr)	Temperature (°C)	Distance (inches)	Film
1	15	0.5	176	4.25	Very rough
2	27	0.5	176	4.25	Rough
3	46	0.5	176	4.25	Rough
4	68	0.5	176	4.25	Smooth
5	100	0.5	176	4.25	Slightly rough

Table 2. Carrier gas flow rate variation. Table of variables. Flow rate was varied from 15 cc/min - 100 cc/min. Films were analyzed via AFM and determined the roughness.

The optimal carrier gas flow rate was determined to be at 68 cc/min. Up to this point, optimum parameter have been established for temperature and carrier gas flow rate. The next variable to be optimized is the distance from glass substrate to the UV light source housing. The heater and UV housing were constructed collectively so the distance from the glass substrate to the UV housing could be varied. The distance ranged from 4.25 inches to 7.25 inches. The distance variable indicated smooth films can also be accomplished by the distance from the UV light housing to the glass substrate. The distance of 6.25 inches proved to be the optimal position of creating smooth films. The position at 4.25 inches showed extreme differences, by clouding up and forming crystals on the surface. The distances of 4.25 and 5.25 inches were found to produce rough surfaces.

Sample	Carrier gas flow rate: (cc/min)	Time (hr)	Temperature (°C)	Distance (inches)	Film
1	68	0.5	176	4.25	Rough
2	68	0.5	176	5.25	Rough
3	68	0.5	176	6.25	Smooth
4	68	0.5	176	7.25	Slightly Rough

Table 3. Distance variation. Table of variables. Distance was varied from 4.25 in. to 7.25 in. Films were analyzed via AFM and determined the roughness.

The optimal conditions have been investigated for three conditions: the temperature, carrier gas flow rate, and distance from UV light source to glass substrate. The optimal parameters were found at a deposition temperature of 176 °C, carrier gas flow rate of 68 cc/min, and distance from UV light source to substrate of 6.24 inches. Time was originally going to be analyzed as a variable for optimal smoothness of TiO_2 deposition; however, it was hypothesized that the thickness of the film would be a function of time.

AFM images of the optimal condition can be seen in Figure 3. The average rms is 0.340 nm. An AFM image of the control, which is glass, can be seen in Figure 4. The average rms of glasss is 0.286 nm. The average was taken by dividing the 5 μm^2 image into 2.5 x 5 µm square and taking the roughness analysis of the image. The images were taken at two different locations on the glass substrate. A total of four samples were taken to achieve an average.

The optimal condition produced very smooth films which are comparable to glass. X-ray photoelectron spectrometer was used to analyze surface for TiO^2. The results of the XPS can be seen in Figures 5 and 6.

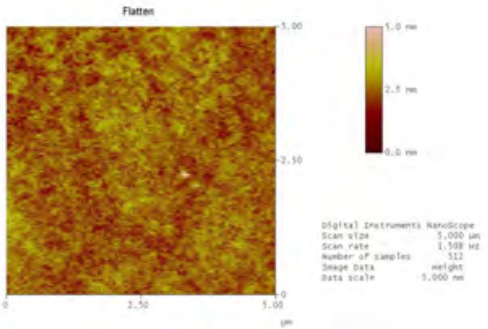

Figure 3. AFM image of optimal parameters at 30 minute deposition. Image is 5 μm^2. Average rms is 0.340 nm, n = 4.

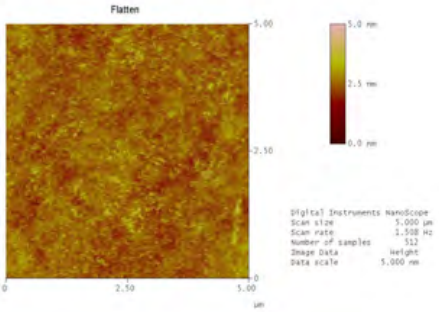

Figure 4. AFM image of the control which was glass. Image is 5 μm^2. Average rms is 0.286 nm, n = 4.

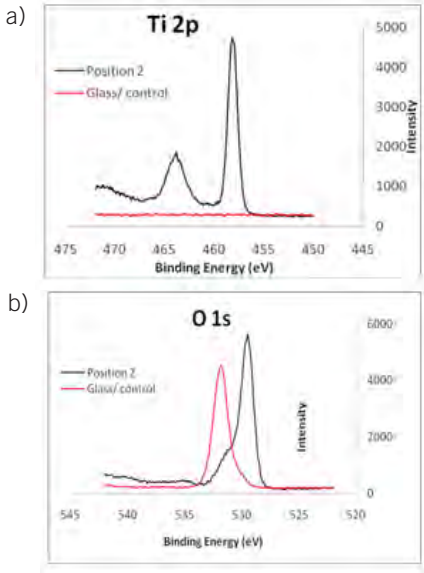

Figure 5. XPS results of the optimal deposition parameters and the control/ glass. a) Ti 2p peak. b) O 1s peak.

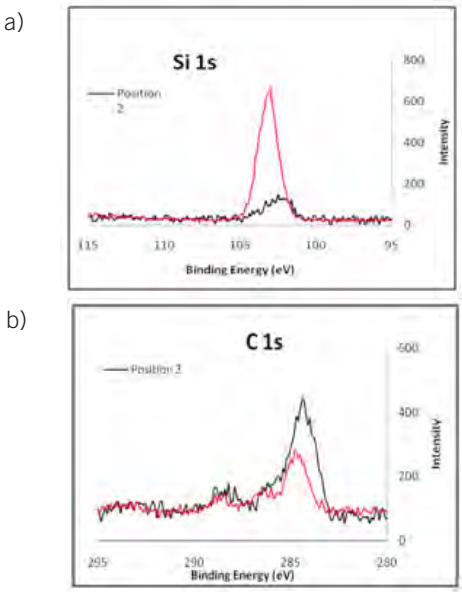

Figure 6. XPS results of optimal deposition parameters and control/glass. a) Si 1s peak. b) C 1s peak.

In Figure 5a. the peaks at 458 eV and 464 eV indicate titanium was deposited on the surface of the substrate. In Figure 5b. the optimal deposition peak shifted to lower binding energy compared to glass. The peak of O 1s of the deposition also shows a shoulder, which may come from a different valence of titanium or perhaps from an additive effect from the SiO_2, nonetheless, TiOx was deposited.

In Figure 6a. the optimal deposition parameters showed silicon electrons were being ejected by XPS. The penetration depth of XPS is typically 1.5 to 5 nm. The peak of the optimal deposition parameters also appears to be shifted slightly to lower binding energy. The peak in Figure 6a. may indicate several things: there may be pin-holes in the TiOx thin film, or the film is very thin (5 nm or less), or the titanium isopropoxide may be interacting with surface of the glass, and shifting the valence state of the silicon.

In Figure 6b. the optimal deposition parameter and the control indicate carbon being the surface in either case. The carbon peak for the optimal deposition parameter is a slightly larger peak, which suggests impurities of titanium isopropoxide by-products may be trapped in the film and/or on the surface of the the film.

Conclusion

A new technique using a chemical vapor deposition chamber was used to create thin layers of TiOx under mild processing conditions. The parameters of the CVD chamber were explored where the optimized parameters for TiOx thin films were identified: deposition temperature at 176°C, carrier gas flow rate at 68 cc/min, and distance from substrate to UV light housing at 6.25 inches.

Future work will include using this technique to apply thin layers of TiOx as an interlayer for charge recombination in tandem OPV's, encapsulating OPV's, and waveguide applications. This technique appears to be promising because of the low temperature deposition and deposition capabilities in vacuum.

Acknowledgments

Funds for this research were provided by the Center on Materials and Devices for Information Technology Research (CMDITR), and the NSF Science and Technology Center No. DMR 0120967.

References

1. Kim, Jin Y., Heeger, Alan J; Science 2007 317. a

DELVIN TADYTIN is a student at the University of Arizona. He is earning his degree in Chemistry and applying to graduate school in fall 2008.

The Synthesis of Organic Dyes as Charge Carriers for Organic Field Effect Transistor (OFET) and Organic Photovoltaic (OPV) Devices

DONOVAN THOMPSON, Georgia Southern University
Jon Matichak, Seth Marder, Georgia Institute of Technology

Abstract

The synthesis and the characterization of organic squaryilium and croconium dyes are described. These organic dyes are expected to have semi-conducting properties that will enable them to be used as a charge transport layer in Organic Field Effect Transistors (OFET) or Organic Photovoltaic (OPV) devices. Several expected useful properties may include: flexible-film-forming properties, low cost, and their near IR absorption in the electromagnetic spectrum for sensitization.

Introduction

Electronic and optoelectronic devices, such as OFET or OPV devices, using organic material as active elements are receiving a great deal of attention.[1] These devices are using these organic materials because they have many advantages such as their flexibility, low cost, and light weight.[1] Organic materials that are used in these devices are known as "organic semiconductors." This class of materials is known by that name because they are in between conductors and insulators and are used as charge carriers.[1]

Background

When a photon gets absorbed by a chromophore acting as a semiconductor, it excites an electron to move from the HOMO (Highest Occupied Molecular Orbital) to the LUMO (Lowest Unoccupied Molecular Orbital). The excited molecule now has an electron in the conduction band and a gap, or "hole" in the valence band. The electron in the conduction band will hop to the adjacent molecule towards the anode because it consists of a charge. The hole in the valence band will continue to move in the direction of the cathode. This process is collectively known as the "hopping" process (Figure 1). Dissociation of the electron-hole pair and transport into the electrode will cause a current; which is electricity.[2] In a similar sense, OFETs (Figure 2) function on the theory that organic semiconductor conductivity can be increased or decreased by the occurrence of an electric field. The amount of free electrons and holes in an organic semiconductor will increase by the presence of an electric field, thereby changing its conductivity.[3] OFETs are used to switch electric signals and use a semiconductor in its active channel. A frequent characteristic of OFETs are the inclusion of a conjugated π-electron system (Figure 3).

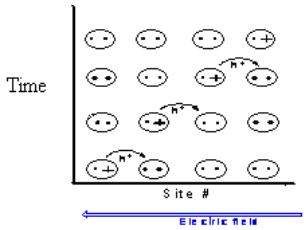

Figure 1: An example of hole transport.

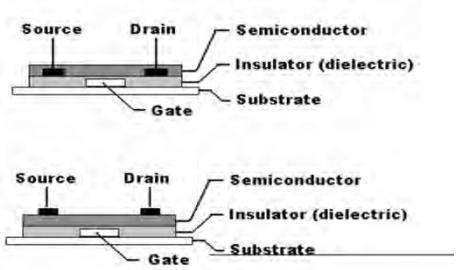

Figure 2: An illustration of an Organic Field Effect Transistor.

Figure 3: An example of two resonance forms of a transport material, oxidized trithiophene.[1]

The objective of this research is to create organic dyes, such as squaryilium or croconiums, which can be used as organic semiconductors or charge carriers for OFET or OPV devices. Possible advantages of the target dyes are they absorb in regions of the spectrum that are not commonly accessed, which distinguishes them from other organic materials. squaryilium and Croconiums were chosen because they can be oxidized, reduced, and they have been used for the semi-conducting layer for OFETs.[4]

The synthesis of squaryilium dyes and croconium dyes has been reported.[5] The squaryilium dyes have a planar structure throughout the π-conjugated system. These dyes absorb in the visible and near IR wavelengths of the electromagnetic spectrum. The croconium dyes have an additional carbonyl group relative to squaryilium that shifts their absorption range to longer wavelengths.[5]

Method

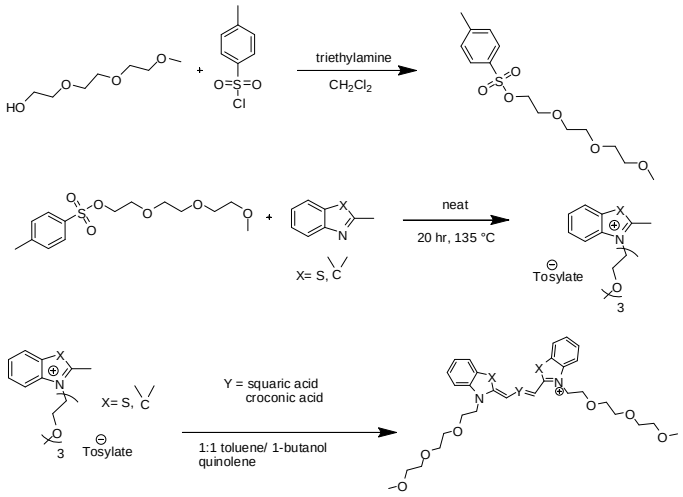

Figure 4: Basic reaction scheme.

The compound 1-bromo-2-(2-(2-methoxy ethoxy) ethoxy) ethane was first used as the starting product from the reaction described in Figure 5.

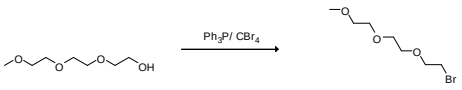

Figure 5.

However, the product with bromide as the leaving group was not as easy to synthesize as the 4-Toluolsulfonyl chloride (Ts-Cl). The Ts-Cl compound contains a stable leaving group and it is easier to purify because it can be seen by UV/Vis on a TLC plate. Using Bromide, there was not a clear separation on TLC plate because the UV/Vis did not identify any double bonds in that compound. The purpose of the PEG chain is to promote aggregation. After the formation of the PEG chain, it will react with an acceptor such as the Benzothiozole compound or the indole compound to form an ammonium salt. These heterocyclic salts are building blocks to form the target dyes.[6] Next, each ammonium acceptor reacted with the squaric and croconic acid to form the symmetric squaryilium and croconium dye.

Experimental

2-(2-(2-methoxyethoxy)ethoxy)ethyl 4-methylbenzenesulfonate

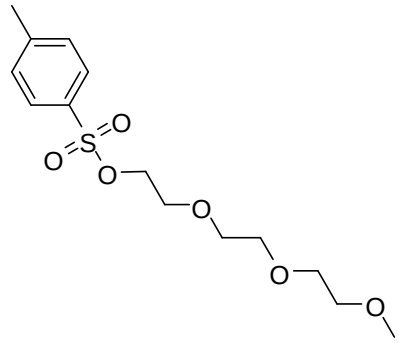

A solution of diethylene glycol monomethylether (98.05 mmol 16.1 g) and triethylamine (147.075 mmol 14.88 g) in dry CH_2Cl_2 (120 ml), 4-toluenesulfonyl chloride (117.66 mmol 22.94 g) in dry CH_2Cl_2 (40 ml) was added. The reaction stirred for 20 hours at room temperature. Saturated $NaHCO_3$ aqueous solution was used to wash the reaction mixture. The anhydrous $MgSO_4$ dried the extract and eliminated any water traces, filtrated, and evaporation of the filtrate. The sample was purified by column chromatography on silica gel using the eluent (4:1) Ethyl Acetate and dichloromethane to attain a light yellow oily liquid substance.[7] The yield was 37% and it was characterized by 1H NMR ($CDCl_3$) similar to the research literature.[7]

Quaternary Ammonium Salt

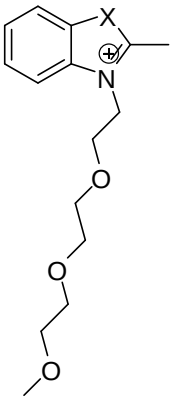

A) X = S Benzothiazole compound

B) X = $C(CH_3)_2$ Indole compound

The reaction was placed under nitrogen atmosphere and carried out with solvent-free conditions. A sample of 2-methylbenzo (d) thiazole (20 mmol, 2.9842 g.) or 2, 3, 3-trimethly-3H-indole (20 mmol, 3.1846 g.) and the alkylating agent (20 mmol, 6.3678 g.) were heated at 135 Celsius (the reaction turns a dark red). After 20 hours of mixing, the reaction mixture was diluted with 30 ml of CH_2Cl_2 and extracted with 40 ml of distilled water. The aqueous phase was washed with 60 ml of CH_2Cl_2 and the water evaporated under reduced pressure conditions to give the desired product which was a slight yellow oily substance. These heterocyclic salts, bearing an activated methyl group in the 2-position in relation to the

nitrogen atom, are precursors for dyes.[6]

2-methylbenzo (d) thiazole: Yield 45%. ^{1}H NMR (400 MH_3, $CDCl_3$). 8.45 (d, 1H), 8.34 (D, 1H), 7.75-7.95 (m, 2H), 7.5 (d, 2H), 7.04 (d, 2H), 4.99 (t, 2H), 3.9 (t, 2H), 3.47-3.42 (m, 4H), 3.37- 3.30 (m, 4H), 3.27 (s, 3H), 3.18 (s, 3H), 2.25 (s,3H)

2, 3, 3-trimethly-3H-indole: Yield 28%. ^{1}H NMR (400 MH_3, $CDCl_3$) 7.94 (m, 1H), 7.84 (m, 1H), 7.45 (d, 2H), 7.1 (d, 2H), 4.7 (t, 2H), 3.9 (t, 8H), 3.4 (m, 4H), 3.2-3.3 (m, 4H), 3.15 (s, 3H), 2.8 (s, 3H), 1.5 (s, 6H)

Squaryilium Dye

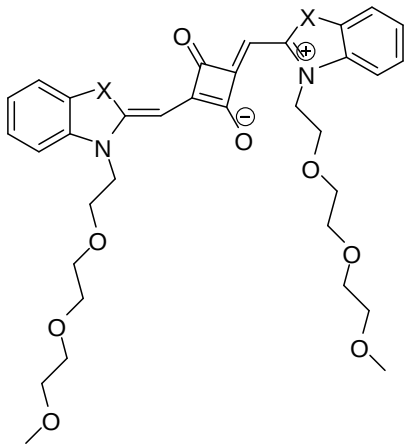

The unknown ammonium salt with benzothiazole compound (1 mmol .477 g) or the ammonium salt with Indole compound (1 mmol .474 g) and squaric acid (.5 mmol .057 g) was kept under the reflux for 3 to 5 hours in (10 ml of each) toluene/ 1-butanol (1:1) in the presence of Quinoline (1 mmol .129 g), using a Dean-Stark trap. The reaction was closely monitored by the characterization of UV/Vis spectra. The appearance of the reaction mixture continuously changed colors. (It changed colors from a dark red to a dark shiny green.) Reaction mixture was purified by column Chromatography in basic alumina with the eluent Ethyl Acetate and then the solvent system was changed to 10% Methanol and Ethyl Acetate for a pure product. Every collection from the column was characterized by UV/Vis. The fractions that displayed peaks in the region expected of a squaryilium were combined and evaporated. There was the presence of a shiny-crystal green solid substance and HNMR detected desired product.

2-methylbenzo (d) thiazole squaryilium: Yield 10%. ^{1}H NMR Mercury 300 ($CDCl_3$). MS (m/z) = 669.2 g/mol

2, 3, 3-trimethly-3H-indole squaryilium: Yield 30%. ^{1}H NMR Mercury 300 ($CDCl_3$). MS (m/z) = 689.3 g/mol

Croconium Dye

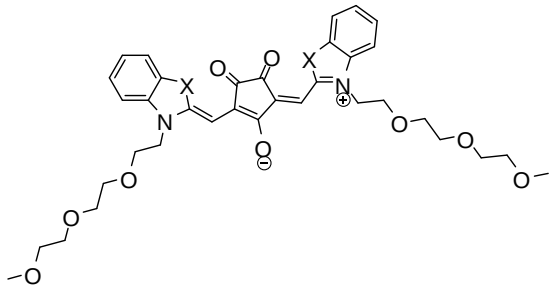

Similar synthesis to the squaryilium dye synthetic procedure was used for the synthesis of the croconium dye. The unknown ammonium salt with benzothiazole compound (1 mmol .477 g) or with the indole compound (1 mmol .474 g) and croconic acid (.5 mmol .067 g) was kept under the reflux for an hour in (7 ml of each) toluene/ 1-butanol (1:1) in the presence of Quinoline (1 mmol. 129 g), using a Dean-Stark trap. The reaction was closely monitored by the characterization of UV/Vis. Reaction mixture was characterized twice in that hour (at the half hour and at the hour). It changed several colors like brown, red, green and a brownish yellow. The reaction was purified by Column Chromatography using the eluent Ethyl Acetate and then the eluent was changed to 20% Ethanol and Ethyl Acetate for better separation. Every collection that displayed an expected croconium peak was collected and combined for evaporation. The presence of a dark brownish substance was obtained. HNMR was used to detect desired product and it was present.

2, 3, 3-trimethly-3H-indole croconium: Yield 9.5%. ^{1}H NMR Mercury 300 ($CDCl_3$). 7.4 (t, 5H), 7.2 (t, 5H), 6.2 (s, 2H), 4.15 (m, 4H), 3.8 (t, 4H), 3.4-3.6 (m, 12H), 3.2-3.4 (s, 6H), 1.6 (s, 33H), 1.2 (s, 9H)

Results/Discussion

The squariliums and croconiums were characterized by MS, ^{1}H NMR, and UV/Vis. The purification of these dyes has been very difficult. The ^{1}H NMR of these dyes seems very pure and clean, but elemental analysis showed that these dyes are impure. The recrystallization method may be a possible way to purify these organic dyes. The squarilium dyes absorb in the visible region of the spectrum; around the 700 nm region. They absorb the red light so their color was a blue/ greenish color. The croconiums absorb at longer wavelengths than the squarilium dyes; near the 800 nm region. Their color was a dark brownish color. Figures 6 and 7 show the UV/Vis spectra of these dyes.

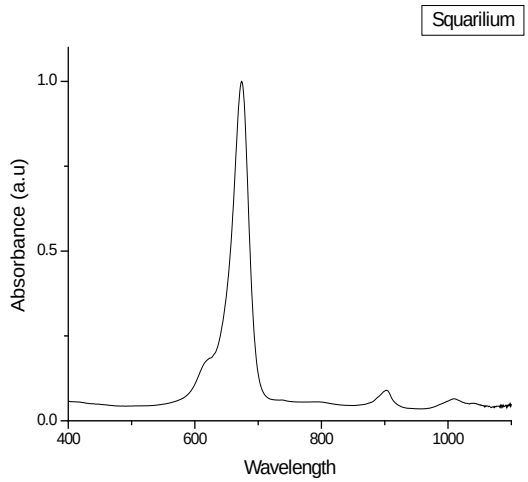

Figure 6: Absorption spectra of squarilium dye with Benzothiazole compound in methanol solution.

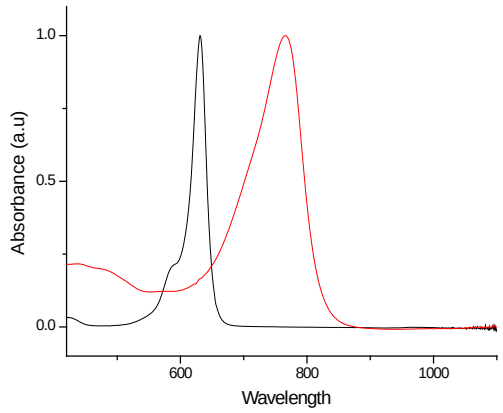

Figure 7: UV/Vis comparison of Croconium dye with Indole compound (red line) and squaryilium dye with Indole compound (black line) in methanol solution.

Potential future work will focus on purification and subsequent device fabrication, so information on charge transport properties can be obtained.

Acknowledgements

This work was supported by the National Science Foundation, Georgia Institute of Technology REU summer program, Materials and Devices for Information Technology Research Center (MDITR), and Center of Organic Photonics and Electronics (COPE).

References

1. Yasuhiko, S.; Hiroshi, K. Chem. Rev. 2007, 107, 953-1010.
2. http://en.wikipedia.org/wiki/SolarCells July 1, 2008.
3. http://en.wikipedia.org/wiki/OFET June 25, 2008.
4. Yum, J.-H.; Walter, P.; Huber, S.; Rentsch, D.; Geiger, T.; Nuesch, F.; Filippo; Angelis, D.; Gratzel, M.; Nazeeruddin, M. K. J. AM. Chem. SOC. 2007, 129, 10320-10321.
5. Matsuoka, M. Infrared Absorbing Dyes; Plenum Press: New York, 1990.
6. Pardel, C.; Ramos, S. S.; Santos, P. F.; Reis, L. V.; Almeida, P. Molecules 2002, 7, 320-330.
7. Edouard, O.; Mathilde, B.; Laurent, B.; Florence, A.; Catherine, L.; Francois, B. J. AM. Chem. SOC. 2007, 15601- 15605.

DONOVAN THOMPSON is a rising senior who attends Georgia Southern University studying Chemistry. In the future, he plans to enroll in a PhD. Chemistry program with emphasis in Organic Chemistry to become a chemist who will attempt to shape the academia avenue of science.

Electro-Optic Coefficient Measurement Using Mach-Zehnder Interferometry

RIKA M. YATCHAK, University of California, San Diego
Charles Greenlee, Mahmoud Fallahi, University of Arizona

Introduction

The electro-optic effect measures the change in the refractive index *n* of a material as a voltage is applied.[1] The electro-optic (EO) effect may have a linear dependence on field (Pockels effect) or a quadratic dependence (Kerr effect). In this abstract, we will be concerned with the Pockels effect.

The EO properties of a material can be useful in applications that require "tuning" of the index of refraction. For example, a Fabry-Pérot etalon (Fig. 1) with an electro-optic material could be used as a tunable filter or switch. Varying the index of refraction of the material in the Fabry-Pérot cavity will affect how much of the incident light will be transmitted.

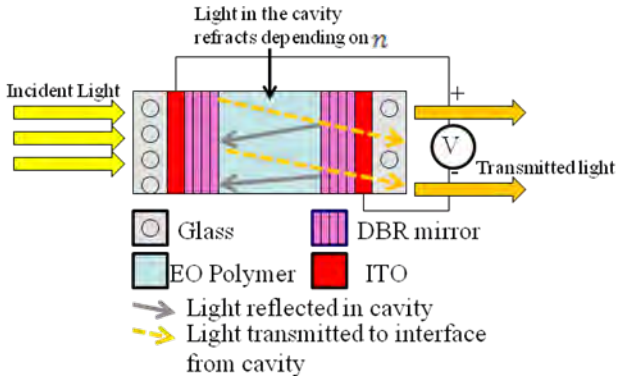

Figure 1: One application in which the electro-optic effect could be useful is the Fabry-Pérot etalon.

The magnitude of the electro-optic effect is described by a quantity called the electro-optic coefficient, or Pockels coefficient. The units of the electro-optic coefficient are meters per volt, usually presented as pm/V.

The electro-optic effect is observed in materials that lack symmetry. Although some commonly used semiconductor crystals such as GaAs exhibit the EO effect, the observed change in *n* is small[1]. It is therefore preferable to use polymer materials containing various concentrations of electro-optic chromophores. After these polymer materials are poled, they display a measurable EO effect based on concentration of chromophore, poling voltage, and fabrication method. Since their characteristics can vary so drastically from sample to sample, these electro-optic polymers must be individually characterized by their EO coefficient.

There are several methods for measuring the electro-optic coefficient. The most popular method is the reflection method described by Teng and Man[2]. The reflection method is a very simple experiment, requiring few instruments and little set-up time (Figure 2). However, it is not without problems. Unfortunately, only one of the Pockels coefficients (r_{33}) can be experimentally obtained using reflection. For their purposes, Teng and Man assumed that $r_{33}/r_{13}=3$. It was thought that r_{13} could be reasonably predicted from this ratio.

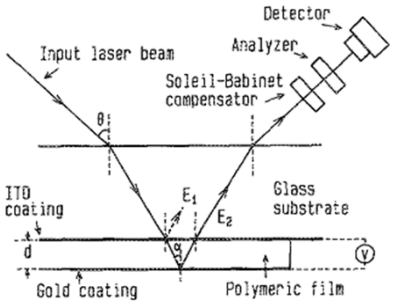

Figure 2: The reflection method for finding the electro-optic coefficient as described by Teng and Man.[2]

This assumption was later proven false by Norwood, Kuzyk, and Keosian[3]. In their work using Mach-Zehnder interferometry to measure the electro-optic coefficient, it was found that the ratio r_{33}/r_{13} varies depending on the material. Thus, it would be advantageous to use this newer, more accurate method to find the electro-optic coefficient.

We implemented the Mach-Zehnder interferometry system in order to measure the EO coefficient of our polymer samples. Samples would be tested immediately after poling and then at controlled times thereafter, to observe the EO coefficient and to determine how it changes over time. Some change in the EO coefficient was expected due to "relaxing" in the polymer, a phenomenon whereby the aligned dipoles from poling will tend to drift back to a charge-neutral configuration.

Experimental Setup

The modified Mach-Zehnder reflection scheme described by Norwood, Kuzyk, and Keosian involves the construction and use of a complicated optical system (Figure 3). A laser light source is incident to the Mach-Zehnder system, which contains the electro-optic polymer sample. The sample is driven by a modulating voltage, while a glass plate is rotated in one arm to create a controllable phase shift due to change in path length. As the plate rotates, the light fringes will modulate (Figure 4). The parameters of interest are

the fringe amplitudes, rms voltage, polarization, and the primary refractive indices of the sample. These values will be used to calculate r_{33} and r_{13} , which will fully characterize the EO coefficients of the sample.

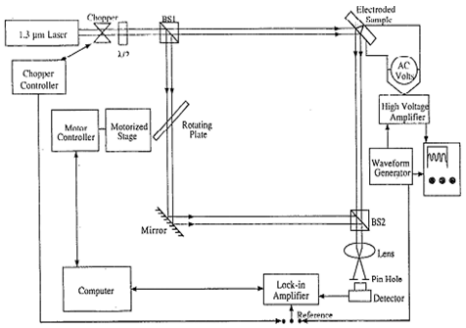

Figure 3: The Mach-Zehnder interferometry set up to measure the electro-optic coefficient.[3]

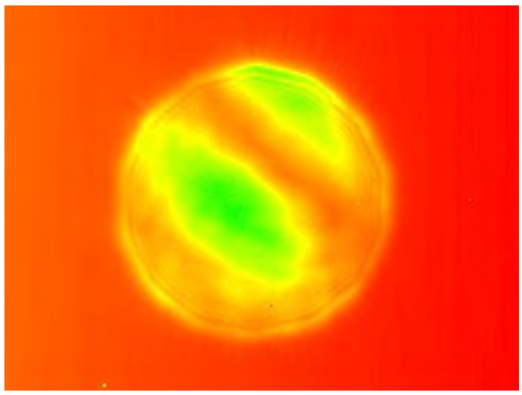

Figure 4: Rotating the glass plate in the Mach-Zehnder interferometer causes the fringe pattern to modulate.

The original intention of the experiment was to use a 1310-nm laser, but it was later decided that the system would be tested using a 1550-nm laser. No other changes were made to the experimental setup. A few laboratory instruments were needed in addition to the actual Mach-Zehnder interferometer. These instruments included a voltage meter, an AC voltage source, a high voltage amplifier, an optical chopper, and a lock-in amplifier.

Finally, electro-optic polymer samples were fabricated for testing. Electro-optic polymers with various concentrations of EO chromophores were placed on a glass and ITO (indium tin oxide) substrate, and then covered with gold, which functioned as the electrode (Figure 5).

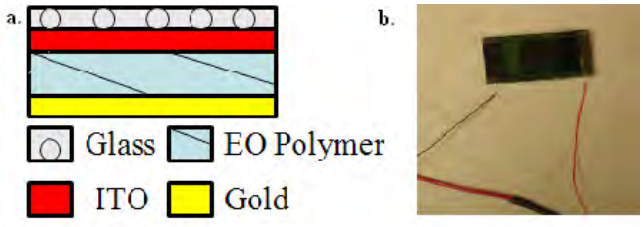

Figure 5: a. Cross-sectional view of a sample, showing layers b. An actual sample ready for testing.

Results and Discussion

According to Norwood, Kuzyk, and Keosian, the calculations for r_{13} and r_{33}/r_{13} are very straightforward. Through some math, it is found that:

$$r_{13} = \frac{\lambda|I_1 + I_2|}{2\sqrt{2}V_{rms}I_r n_1^3}\frac{\cos\theta}{2} \qquad (1)^3$$

and:

$$\frac{r_{33}}{r_{13}} = \left[\left(\frac{n_1}{n_3}\right)^4\left(\frac{n^3(n^3)^3 r_{33}}{n^1(n^1)^3 r_{13}}\right) - \cos^2(\theta)\right]/(\sin^2(\theta) \qquad (2)^3$$

where $I_1 + I_2$ is the sum of the intensity of the large and small peak from the signal sample data, I_r is the intensity of the reference data, V_{rms} is the amplitude of the modulating voltage applied to the sample, θ is the internal angle of the light in the sample, and n_1 and n_3 are the indices of refraction for s and p polarizations respectively.

A simple MATLAB program was written to automate these calculations using experimentally obtained values. Because all readings were preliminary, reasonable values for I_{sig} and $I_1 + I_2$ were found by taking an average of the peaks visible in the experimentally obtained data. No error calculations were made.

Figure 5 shows the MATLAB plot made of the baseline and signal measurements for s polarization for an APC (amorphous polycarbonate) polymer sample with a 20% concentration of the electro-optic chromophore SWOHF3ME. The sample was contact poled at 25 *V/μm*. After aligning the optical system, the fringe contrast was found to be .9677. Calculations yielded a measured r_{13} of about 13.32 *pm/V*. The expected r_{13} was less than 8 *pm/V*, as the poling voltage and chromophore concentration were low.

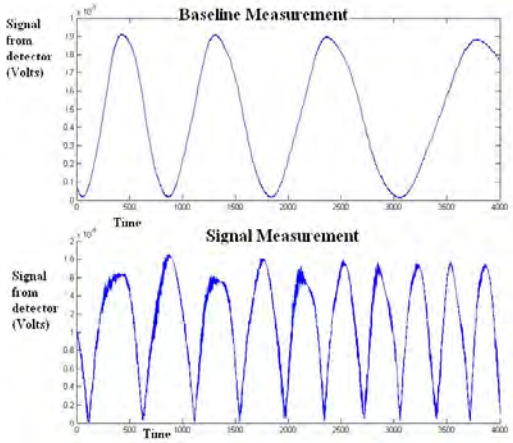

Figure 6: The measured results showed gave an experimental r_{13} of about 13.32 *pm/V*. This was higher than expected.

All experimental runs exhibited a similar deviation from the expected result, with all measured r_{13} values being incorrect by one to two orders of magnitude. From the data (Figure 6), it appears that the measured signal from the detector is higher than anticipated. From Equation 1, it follows that it would be preferable for the $I_1 + I_2$ quantity to be less than I_{sig} by several orders of magnitude. However, the measured signal did not give this anticipated result. Detector malfunction was later excluded as an error factor.

The most likely reason for this observed error stems from the

piezoelectric effect. The piezoelectric effect causes contraction or expansion of the poled film due to applied voltage.[2] According to Norwood, Kuzyk, and Keosian, the piezoelectric effect is not an issue in the reflection method because of cancellation of first-order effects, but it may be an issue that would cause the measured r_{33}/r_{13} result to be greater than expected in the Mach-Zehnder interferometry method. More data is needed to conclusively show that the piezoelectric effect is the culprit for this large measurement error.

Because of the large measurement error, we were unable to conclusively test the change in EO coefficient over time in our polymer samples.

Conclusion

The Mach-Zehnder interferometry method of measuring the electro-optic coefficient is a promising way to obtain accurate results. Once the system is properly calibrated, it is possible to obtain r_{13} and r_{33} independently, without using any approximations. The advantages of this method are many, but increased accuracy does not come without a price. The experimental setup is far more involved, and data acquisition can be complicated.

Future directions to be taken with this method include refinement of the data acquisition technique, and determining a minimum fringe contrast required for reasonable accuracy of measurement. A vital extension of this research would be to determine an explicit way to quantify the piezoelectric effect in the sample. This would be a useful known quantity on its own, but is also essential to the electro-optic measurement as it could inflate the r_{33}/r_{13} ratio.

Acknowledgments

Funds for this research were provided by the Center on Materials and Devices for Information Technology Research (CMDITR), and the NSF Science and Technology Center No. DMR 0120967. Special thanks to Dr. Robert Norwood- without his previous work and good advice, this project would not have been possible. Additional thanks are owed to my mentors Charles Greenlee, and Dr. Mahmoud Fallahi, for an excellent summer research experience.

References

1. B. E. A. Saleh and M. C. Teich. Fundamentals of Photonics. 1991
2. C. C. Teng and H. T. Man, Applied Physics Letters 1990, 56, 1734-1736.
3. R. A. Norwood, M. G. Kuzyk, and R. A. Keosian, Journal of Applied Physics 1994, 75, 1869-1874

RIKA YATCHAK is earning an undergraduate degree in electrical engineering with a concentration in photonics, and a second degree in mathematics. Upon completion, she plans to pursue a Ph.D.